Effect of Submerged Arc Welding Parameters on the Microstructure of SA516 and A709 Steel Welds

A Thesis Submitted to the College of

Graduate Studies and Research

In Partial Fulfillment of the Requirements

For the Degree of Doctor of Philosophy

In the Department of Mechanical Engineering

University of Saskatchewan

Saskatoon

By

James Amanie

© Copyright James Amanie, August 2011. All rights reserved.

PERMISSION TO USE

In presenting this thesis in partial fulfilment of the requirements for a Postgraduate degree from the University of Saskatchewan, I agree that the Libraries of this University may make it freely available for inspection. I further agree that permission for copying of this thesis in any manner, in whole or in part, for scholarly purposes may be granted by the professors who supervised my thesis work, Prof. S. Yanacopoulos and Prof. I. N. A. Oguocha or, in their absence, by the Head of the Department of Mechanical Engineering or the Dean of the College of Engineering. It is understood that any copying or publication or use of this thesis or parts thereof for financial gain shall not be allowed without my written permission. It is also understood that due recognition shall be given to me and to the University of Saskatchewan in any scholarly use which may be made of any material in my thesis.

Requests for permission to copy or to make other use of material in this thesis in whole or part should be addressed to:

Head of the Department of Mechanical Engineering

57 Campus Drive

University of Saskatchewan

Saskatoon, Saskatchewan, Canada S7N 5A9

ABSTRACT

The effects of submerged arc welding (SAW) current and speed on the microstructures of SA516 grade 70 and A709 grade 50 steel welds were studied in this research. Steel plates 17 mm-thick were submerged arc welded using different welding currents (from 700 to 850 A) and welding speeds (from 5.3 to 15.3 mm/s). The effect of heat input on the weld metal chemistry, morphologies and chemistry of inclusions and nucleation of acicular ferrite (AF), grain boundary ferrite (GBF) and Widmanstatten ferrite (WF) were evaluated. Optical microscopy (OM), scanning electron microscopy (SEM), energy dispersive X-ray spectroscopy (EDS) microanalysis and transmission electron microscopy (TEM) were used to examine the microstructures of the developed weld joints. PAX-it image analysis software program was utilized for quantitative analysis of the microstructures.

The results showed that it is difficult to ascribe changes in the microstructure that occurred in the heat affected zone (HAZ) and the weld metal regions to a single welding process parameter. Inclusion analysis revealed two types of inclusions formed in the weld metals for both steels. They are spherical and faceted inclusions. It was also observed that acicular ferrite nucleated only on the spherical inclusions. EDS analysis showed that the two inclusions have different chemical compositions.

The results further showed that the total oxygen content of the weld metals of both steels generally increased with welding current, but decreased with increasing welding speed.

The prior austenite grain width decreased with increasing welding speed, but increased with increasing welding current (increased heat input). For both SA516 and A709 steel welds, the proportion of acicular ferrite (AF) in the weld metals increased initially, while those of grain boundary ferrite (GBF) and Widmanstatten ferrite (WF) decreased with increasing welding current when welding current was increased from 700 A to 800 A. With further increase in the welding current above 800 A, less acicular ferrite was produced as both GBF and WF proportions increased. However, welding speed did not affect appreciably the amounts of ferrite products in the weld metals.

Non-linear regression models were developed using welding current and welding speed to predict the ferrites (AF, GBF, WF) that formed in the weld metals of the two steels. The adequacy of the models was checked by using the F-statistics.

ACKNOWLEDGMENTS

I would like to thank my supervisors, Profs. S. Yannacopoulos and I. N. A. Oguocha, for their guidance and support during the course of this project. I would like to thank members of my academic advisory committee, Profs. D. Sumner, D. Torvi, A. Odeshi, M. Boulfiza and P. B. Hertz for their faithful criticisms, enlightening corrections and suggestions.

I would like to thank Hitachi Canadian Industries (HCI) Ltd., Saskatoon, and the Natural Science and Engineering Research Council (NSERC) for providing the test materials and financial support. My thanks go to Mr. R. McEachern, Dr. H. Guo and Mr. G. Marisca for their personal interest and advice. My thanks go to the Universities of Manitoba and British Columbia for the use of SEM and TEM. I am grateful for the help received from Dr. R. Sidhu, Prof. L. Ojo and Mrs. M. Fletcher. I extend my thanks to Mr. F. Hamad, Evraz Regina Steel, Regina for their assistance in elemental composition analysis. My gratitude goes to Mr. T. Bonli, Mr. R. Peace and Mrs. N. Kelley for their invaluable assistance.

Thanks to Dr. E. Arinze (deceased), Rev. M. Arinze and Dr. S. Attah-Poku for their encouragement. Finally, my family deserves mention for their unfailing support and tolerance. Imagine your first day in Heaven. Trust in the Lord with all your heart and completely lean on Him.

Dedicated to my family; Theresa, John, Victor, Emmanuel and Michael.

TABLE OF CONTENTS

LIST OF TABLES

LIST OF FIGURES

NOMENCLATURE

Abbreviations

A	Austenite; Welding current
AF	Acicular ferrite
ANOVA	Analysis of variance
ASME	American Society of Mechanical Engineers
ASTM	American Society for Testing Materials
AWS	American Welding Society
B	Bainite
BM	Base metal
BI	Basicity index
b	Weld nugget width
C	Carbide
CCT	Continuous cooling transformation
CGHAZ	Coarse grain heat affected zone
CI	Cooling rate interface
CR	Cooling rate
EDS	Energy dispersive X-ray spectroscopy
ESAB	Elektrika Svetsnings Aktiebolaget (Swedish Arc Welding Company)
FGHAZ	Fine grain heat affected zone
FZ	Fusion zone
GBF	Grain boundary ferrite
GMAW	Gas metal arc welding

GTAW	Gas tungsten arc welding
HAZ	Heat affected zone
H	Welding heat input
HSLA	High-strength low alloy
h	Weld reinforcement
I	Current
M	Martensite
NA	Nugget area
OM	Optical microscope
PWHT	Post weld heat treatment
PV	Pressure vessel
S	Travel speed
SAW	Submerged arc welding
SEM	Scanning electron microscope
TEM	Transmission electron microscope
TS	Tensile strength
V	Arc voltage
VHN	Vickers hardness number
WF	Widmanstatten ferrite
WM	Weld metal
WT	Wind tower
w	Heat affected zone size

Greek Symbols

α	Thermal diffusivity
α-Fe	Ferrite
δ-Fe	Delta ferrite
γ-Fe	Austenite
β	Regression coefficient
λ	Thermal conductivity

CHAPTER 1 INTRODUCTION

1.1 Overview

Steels are the most important structural materials for construction because of their high strength and toughness and relatively low cost. The properties of steels can be optimized by altering their chemical composition and through heat treatment. Among structural steels, high-strength low-alloy (HSLA) steels have emerged as the preferred material choice in the fabrication industry. HSLA steels mainly contain low carbon (0.05 to ~ 0.25 wt.% C), manganese (0.9 to 1.8 wt.% Mn), and small additions of alloying elements at concentrations less than 0.1 wt.% such as Cr, Mo, Si, Cu, V, Nb, Ti, Al and B. These steels have yield strength greater than 800 MPa and possess good toughness at low temperatures compared to conventional carbon-manganese steels due to their fine grained microstructure and evenly distributed precipitates which offer precipitation strengthening [1]. HSLA steels are increasingly employed in several applications such as boilers and pressure vessels, boats, bridges, wind turbine towers, oil and gas pipelines. In these applications it is essential to form strong joints and welding is generally the preferred joining method. Welding provides continuous strong joints and avoids crevice corrosion problems often associated with fasteners and rivets and also offers greater bonding and less stress concentration at the point of attachment.

There are several welding methods in use in the industry. They include submerged arc welding (SAW), shielded metal arc welding (SMAW), gas tungsten arc welding (GTAW) and flux cored arc welding (FCAW) [2]. Among the several arc welding methods, the submerged arc welding is the preferred method for welding thick sections in the industry because of its several advantages which include high production rates, good weld quality, ease of automation and minimum operator skill requirement. Despite their numerous advantages, welded joints can often act as sources of weakness leading to catastrophic structural failures such as boiler explosion or bridge collapse. The goal during welding is to obtain the best possible combination of strength and toughness for the welded joint. Strength and toughness are both strongly influenced by the microstructure [2-4]. However, with optimal selection of welding current and speed, it is possible to obtain a weld metal microstructure that provides strength comparable to the base steel.

As strength increases, it becomes difficult to maintain the toughness requirement irrespective of the selected welding method. This is because the microstructure of the as-deposited weld metal has complex dependence on several variables including the base metal chemistry, the filler metal and the flux as well as the actual cooling rate of the weld metal as it cools to room temperature. The high heat input employed during welding is associated with high temperatures which create the molten weld pool. It can also induce high temperature chemical reactions between the flux and the molten metals. These reactions and subsequent thermal cycles can cause unwanted phase transformations and compositional changes which alter the final microstructure and properties of the welded joints. Upon cooling and solidification the welded joint evolves

from its original base metal structure into additional distinct structural regions namely, the weld metal (WM) and heat affected zone (HAZ) with microstructures and properties different from those of the base metal. The extent of change depends on the maximum temperature experienced by the joint, the length of time that the high temperature lasted and the cooling rate after the welding process [5-7].

During cooling of carbon-manganese steel welds from the molten state, austenite that forms at elevated temperatures transforms into various ferrite morphologies on cooling. The microstructural constituents observed using optical microscopy and the sequence of their formation, according to Abson and Pargeter [8], are as follow: (i) grain boundary-nucleated primary ferrite (GBF) forms at the prior austenite grain boundaries between 1000 and 750°C, (ii) ferrite side plates, which nucleate at the ferrite-austenite boundaries and grow in the form of thin plates into the austenite, also known as Widmanstatten ferrite (WF), forms between 750 and 650°C, and (iii) fine-grained intergranularly-nucleated acicular ferrite (AF), which nucleates at some inclusions forms at approximately 650°C. Small quantities of other microconstituents consisting of mixtures of martensite and retained austenite, which is the residual, untransformed austenite remaining after GBF, WF, and AF have formed, may be observed, especially at high cooling rates. It is generally accepted that the optimal strength and toughness of the welded joint is obtained by maximizing the AF content of the weld metal, whereas the formation of GBF and WF is detrimental to the toughness of the weld metal because they offer less resistance to crack propagation [9-13]. The relationship between welding process parameters and the microstructures formed in a weldment has been the subject of many investigations [6-14]. The findings from these investigations are diverse and

often conflicting because the effects of the individual welding parameters and the mechanism involved is not clearly understood.

1.2 Challenges

Increasing welding process productivity can be achieved by increasing the deposition rate. This can be achieved by either increasing heat input in single wire welding or using multiple wires at the same heat input. Multiple wire welding will need extra capital and operator training. Heat input can be increased by either increasing welding current or reducing welding speed. However, increasing heat input adversely affects the microstructure and properties of the weld joint.

Notwithstanding the low carbon equivalent values and good weldability of HSLA steels, there are problems that need to be addressed when welding in order not to degrade the original mechanical properties of the base metal. To produce good quality welds, it is essential to understand the changes that occur in the microstructure of the weldment. Although acicular ferrite has been identified as the microstructural constituent that controls the strength and toughness in steel weld metals, and that increasing its amount provides both increased toughness and improved strength, it is not entirely clear the type of inclusions that nucleate acicular ferrite and how acicular ferrite nucleation is affected by the process parameters of current and speed [8, 15-20].

1.3 Scope

This work focused mainly on the broad area of evaluating the changes in microstructure that occurred in the weld metals of SA516 grade 70 and ASTM A709 grade 50 steels as a result of varying welding current and speed. It also focused on finding the correlation between the submerged arc welding parameters and the microstructures of the welded joints. In the course of this work, the factors that control the formation of acicular ferrite, grain boundary ferrite and Widmanstatten ferrite, i.e., austenite grain size, inclusions morphology, weld metal chemistry, weld nugget size and cooling conditions were examined. The type of inclusions that support acicular ferrite nucleation and formation of other ferrites were investigated. SA516 grade 70 and A709 grade 50 steel plates submerged arc welded using welding currents from 700 to 850 A, welding speeds from 5.3 to 15.3 mm/s and a fixed voltage of 35 V were examined.

1.4 Objectives

The main objectives of this study were:

1. To determine the effects of welding current and welding speed on the microstructures of steel weld metals and heat affected zones of SA516 grade 70 and ASTM A709 steel welds.
2. To establish the relationship between the microstructure of the weld metals and the SAW welding parameters (welding current and welding speed).

1.5 Thesis Outline

The thesis is divided into five chapters. Chapter 1 presents an introduction to the study, the challenges and main objectives. A comprehensive literature review of previous research pertinent to this study is presented in Chapter 2. In Chapter 3, the materials and experimental methods used in the study are presented. Chapter 4 presents and discusses the experimental results. A summary of the conclusions and suggestions for future work are given in Chapter 5.

CHAPTER 2 LITERATURE REVIEW

This chapter reviews the available literature relevant to this study. The focus is on the development of microstructures in the heat affected zones and weld metals of carbon and low alloy steels with respect to changing welding process parameters.

2.1 High Strength Low alloy (HSLA) Steels

HSLA steels, also termed microalloyed steels, are low-carbon steels typically containing 0.05 to 0.25 wt.% carbon (C) and 1.3 to 2.0 wt.% manganese (Mn). Small additions ($\leq$ 0.1 wt.%) of other alloying elements such as niobium (Nb), vanadium (V), aluminum (Al), titanium (Ti), copper (Cu), silicon (Si), Zirconium (Zr), chromium (Cr), molybdenum (Mo) and calcium (Ca) are added in various combinations to meet the desired mechanical properties. Some of the alloying elements combine with carbon to form carbides (e.g., chromium carbide ($Cr_{23}C_6$), niobium carbide (NbC) and vanadium carbide (V_4C_6)) or with nitrogen to form nitrides (e.g., titanium nitride (TiN), niobium nitride (NbN) and chromium nitride (CrN)) to provide grain refining, precipitation strengthening and improved formability. Cu is added to increase the corrosion resistance of these steels by forming a protective oxide film [15, 16]. Typically, HSLA steels have microstructures consisting mainly of ferrite and pearlite and small amounts of carbides carbonitrides and nitrides depending on the heat treatment and processing received during production [17, 18].

The yield and tensile strengths of HSLA steels range from 275 to 550 MPa and 380 to 620 MPa, respectively [15, 17, 19].

2.2 Submerged Arc Welding (SAW)

Welding is a technique for joining metals. A small amount of molten steel is deposited within the gap between the components to be joined and fuses them together upon solidification. The heat sources used for the welding process include electric arc, laser, electron beam and friction. The submerged arc welding (SAW) technique, which was used in this study, is a fusion welding process in which the molten steel is produced by an electric arc submerged under a granular flux bed. The flux is fed by gravity from a hopper above, in the path of the moving electrode. Figure 2.1 is a schematic illustration of a typical set-up for a single wire SAW process. The major components of the system are the regulated welding current which provides the heat to fuse the filler electrode, granular flux and the base metal which is the workpiece. The flux fuses during welding and forms a slag that floats on the surface of the weld and protects the steel against oxidation from the environment. The SAW process uses high welding currents (300 A to 1600 A) and high travel speeds which result in increased heat input and deposition rate [20]. The technique is therefore good for welding thick materials provided suitable joint design and welding procedures are used. Depending on the thickness of the plate to be welded, either single-pass or multiple-pass electrodes can be used to increase the deposition rate and reduce welding cost.

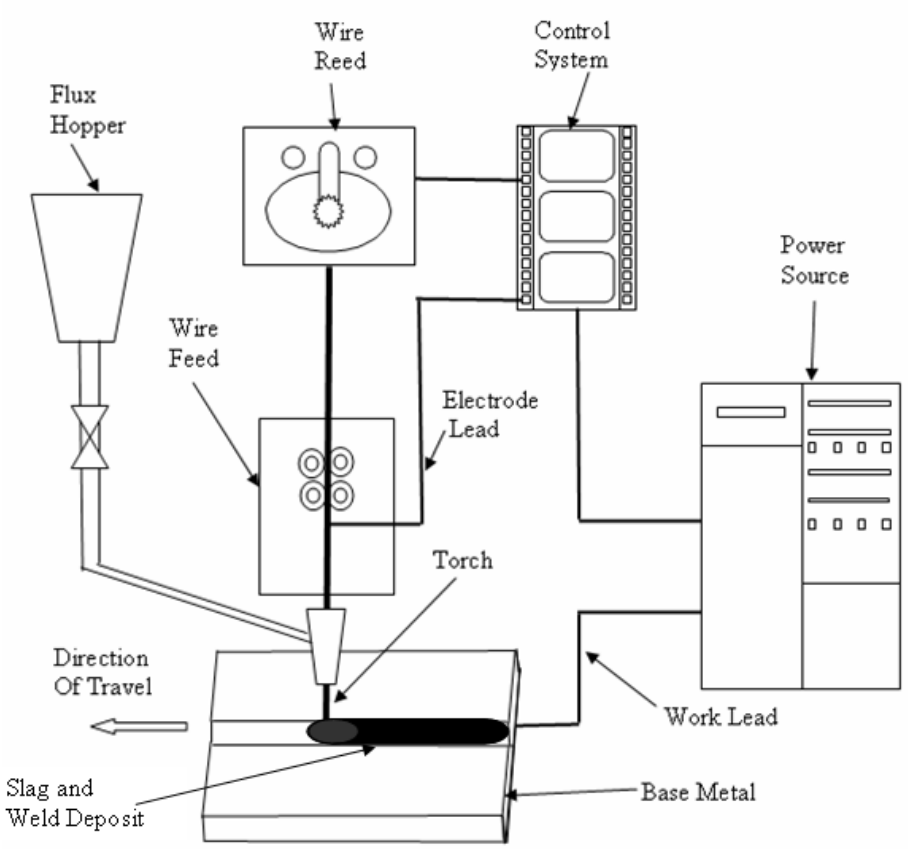

Figure 2.1. Equipment setup for single wire submerged arc welding process (adapted from [21]).

Due to the slag and flux cover over the weld, heat loss to the environment is small and as a result, the thermal efficiency (ratio of energy output to the energy input) of the SAW process is as high as 95% [21]. The efficiencies for other welding processes are comparatively lower. For plasma arc welding (PAW), it is 47%; for gas tungsten arc welding (GTAW), it is 67%; and for gas metal arc welding (GMAW) it is 85% [21]. SAW is used for longitudinal and circumferential butt and fillet welds in the flat position to prevent the molten metals and flux flowing out of the weld joint. After welding, the weld is left to cool in air with the slag on top of the weldment. After cooling, the molten flux solidifies and the slag is removed from the weldment by slight chipping.

The fluxes typically used in the SAW process contain silica, alumina, manganese oxide which form aluminum, silicon and manganese oxides and oxygen in the slag and the molten metal during the welding process [5, 21, 22]. As the metal cools, some of these deoxidation products will become trapped in the solidifying metal as inclusions which have a substantial effect on the subsequent development of the weld microstructure. The composition of the weld metal is determined mainly by the chemistry of the welding electrode which completely melts and mixes with only a small portion of the base metal which actually melts to form the weld pool. In the SAW process, as is in all fusion welding, the filler electrode and the base metal have different chemistries. The weld metal consequently assumes a composition lying somewhere between that of the filler metal and that of the base metal [21, 23]. This effect is called dilution and it comes about because the filler metal penetrates and melts into the base metal.

Nitrogen enters the weld pool from the air. When the nitrogen amount in the weld is large, precipitation of nitrides can occur on cooling due to the different solubilities of nitrogen in δ-iron and in austenite (γ) [24]. Hydrogen can also enter the weld pool through the moisture in the flux but, because hydrogen has high diffusivity in iron, a lot of it escapes from the weld surface. However, small quantities of hydrogen which remain in the weld metal diffuse into the base metal and causes embrittlement and heat affected zone (HAZ) cracking [24]. For thick plates, hydrogen causes more problems because it has a longer distance to travel through to the surface and because it is unable reach the surface much of it is entrapped. Due to this damaging effect of hydrogen on weld metals, it is necessary to eliminate it as much as possible. For this reason, the flux is dried to remove any moisture accumulated during storage before it is used.

2.3 Factors Affecting the Characteristics of SAW Welds

The main variables that determine the characteristics of welds include: (1) welding current, (2) welding voltage, (3) welding speed, (4) flux type, (5) electrode size, (6) electrode extension (or stick-out), (7) angle of electrode and (8) electrode chemistry. The flux type, electrode chemistry, size, angle and stick-out were all pre-selected and remained the same for all the welded joints investigated in this study. The parameters varied were the welding current and welding speed, while the welding voltage was fixed. Effects of these variables on the SAW process and weld quality are briefly explained below [1, 2, 21].

2.3.1 Heat Input

The heat input during welding is controlled by the welding current, voltage and speed. The heat input per unit length (H) is calculated according to the following equation [25].

$$H = \eta \frac{EI}{1000S} \tag{2.1}$$

where H = heat input (kJ/mm), E = arc voltage (V), I = welding current (A), S = arc speed (mm/s) and η = arc efficiency. In submerged arc welding, (η = 0.90-0.99) [1]. The arc efficiency is a quantitative measure of the fraction of total energy delivered to the work piece. The *1000* in the denominator is due to unit conversion.

Increasing heat input increases the cross-sectional area of the weld bead. Depending on the joint geometry, at higher heat input fewer runs per layer are needed because of the

increased filler material. With increasing heat input, the average hardness and strength of the weld decreases [24]. From a practical production perspective, it has been common practice to correlate the weld metal properties with the heat input determined using equation (2.1). Although this approach seems very practical, it does not properly assess the effects of the individual welding parameters. This is because different combinations of welding current and speed give the same heat input, and thus may be viewed as identical heat input conditions. However, it was shown that the weld metal microstructure under identical heat input conditions can be different with different welding current and welding speed combinations [13].

2.3.2 Welding Voltage

The welding voltage governs the length of arc which, in turn, controls the width of the weld metal. Keeping all other welding parameters constant, if voltage is increased, the weld bead width increases but weld penetration decreases. High voltage also increases flux consumption as a result of the wider weld bead. Dilution of the base metal is also affected by increased voltage. The arc voltage is therefore a key parameter in controlling the chemical composition of the weld metal [26].

2.3.3 Welding Current

According to equation (2.1), welding current and heat input are directly related; increasing welding current increases heat input. It determines the rate at which the welding electrode is melted, the amount of base metal melted, dilution, and the weld geometry. Increasing welding current increases the amount of filler material and flux

use, penetration and weld reinforcement [25-29]. For smaller diameter electrodes, higher current density is achieved, for the same amount of current thereby increased penetration and narrower weld beads will be produced. Increasing the electrode size will reduce penetration and broaden the weld bead due to reduced current density. When all other welding parameters remain constant, high current will lead to an increased reinforcement with a narrow bead and excessive penetration that may result in melt 'run-out' [30]. The melt run-out is the molten metal and slag which being very fluid tends to run out of the joint. Using very high current consumes additional filler material, which leads to high reinforcement that will be machined out eventually at an additional cost. Increased reinforcement also increases the weld shrinkage and can cause distortion in the weld. On the contrary, very low current will result in unstable arc and cause incomplete fusion or inadequate penetration [15, 26, 28].

2.3.4 Welding Speed

The travel speed of the arc has major effects on the quality and properties of the final weld. As shown in equation (2.1), welding speed is inversely proportional to heat input. It is usually used to control bead width and penetration [15, 26, 28]. Keeping all the other parameters constant, increasing welding speed produces narrower weld beads and increased cooling rates which may form martensite. The amount of porosity in the weld is also directly related to the welding speed. Very low welding speed results in a large molten pool and spreading weld bead and causes solidification cracking and increased flux consumption. Due to the large amount of melt in the pool, some will flow around the arc and result in spatter and slag inclusion. Very slow speed also results in increased

arc exposure because of the high flux consumption and high heat input. This in turn produces large size HAZ and increased grain coarsening [15, 27-30]. Kanjilal *et al*. [31] in their study using acidic fluxes in shielded metal arc welding noted that for a given electrode, flux and base metal, weld travel speed had by far a larger effect on manganese recovery from the slag-metal reaction than current. On the contrary, North [32], who used submerged arc welding, found that there was no effect of travel speed on manganese recovery. The two observations on the effect of travel speed on manganese recovery are conflicting probably because of the different welding processes used in the two studies.

2.4 SAW Consumables

Apart from the base metals, the consumables used in SAW are the welding electrode and flux. Different flux-electrode combinations will result in different weld metal properties, so selection of welding consumable is of primary importance in the weld process specification.

2.4 1 SAW Electrodes

The electrode conducts electrical current and supplies the filler materials required to fill the gap between the workpiece to fuse the weld joint. SAW electrodes are bare metals with thin copper coatings to improve their electrical conductivity and corrosion resistance (shelf life) [2]. The chemical compositions of welding wires are chosen according to the service application but they always have low (~ 0.10 wt.%) carbon content and low levels of residual and impurity elements, especially nitrogen, sulphur

and phosphorus. They come in sizes ranging from 1.6 mm in diameter for the current range of 150 to 400 A to 6.4 mm in diameter for the current range of 700 to 1600 A [33].

2.4.2 The Flux

The flux protects the molten weld and the arc from environmental contamination and also provides additional filler material for the weld joint. In SAW, a layer of flux completely covers the molten metal and prevents weld spatter and electric sparks. The flux also keeps the fumes and gases generated during welding from escaping into the surroundings. In the molten state the flux in addition, conducts current from the electrode to the work piece [33]. The flux is a very important component for achieving good quality welds. The composition of the flux includes oxides of Mn, Si, Ti, Al, Ca, Zr, Mg and other compounds [34]. The flux is characterized by the basicity index (*BI*), which is a measure of oxygen transfer ability to the weld metal during the welding process [34]. Tuliani, *et al.* [35] defined *BI* as:

$$BI = \frac{\%CaO + \%CaF + \%MgO + \%K_2O + \%Na_2O + 0.5(\%MnO + FeO)}{\%SiO_2 + 0.5(\%Al_2O_2 + \%TiO_2 + ZrO_2)} \qquad (2.2)$$

where, *BI* is basicity index and % refers to elemental composition in wt.%. Basicity index ranges are classified as follows: acid, < 1; neutral, 1-1.5; semi-basic, 1.5-2.5; and basic, > 2.5 [35].

It was reported that the weld metal oxygen content, which is of fundamental importance to the nucleation of acicular ferrite because of the inclusions they form, decreased with increasing flux basicity index [36]. It was shown that the weld metal oxygen content decreased as the flux basicity increased up to 1.25 and remained constant at approximately 250 ppm oxygen (O) thereafter [36]. High *BI*, in addition to reducing the weld metal oxygen level, produces clean weld metals with regard to oxide inclusions and consequently improves strength and toughness of the weldment [37, 38].

High temperature reactions that occur during the SAW process between the slag and molten metal determine the amount and type of inclusions that form in weld metal depending on the flux composition [39]. Manganese, calcium, silicon and titanium oxides have been observed to have both beneficial and detrimental effects on the mechanical properties of welds [16, 40]. Titanium oxide promotes the formation of AF and suppresses weld cracking [41, 42]. The Mn and Si contents in fluxes are strictly controlled because during solidification, these elements segregate and create variations in hardness and uneven microstructural distribution of the weld metal [42]. Butler and Jackson [43] reported that a reduction of weld metal oxygen content was obtained as the percentage of $MnO + SiO_2 + TiO_2$ in the flux used for the SAW process was reduced. Devillers *et al*. [44] similarly observed that lowering the flux $MnO + SiO_2$ content reduced the weld metal oxygen content.

2.5 Weldability of Steels

Weldability is the ability to weld a material. The base metal near the fusion line during welding heats up above the A_3 temperature and austenite forms. As the weld cools, the

austenite in this zone transforms into new structures which are dependent on the cooling rate and the continuous cooling transformation diagram of the BM. If martensite is the product of the austenite transformation, the weld becomes very brittle and susceptible to failure due to cracking. Most metals can be welded with varying degrees of difficulty to produce weld joints with good mechanical properties for the intended application. Weldability of a material is a measure of its resistance to cracking during and after welding and in service performance, i.e., adequate strength and resistance against brittle and ductile fracture propagation. If it is easy to avoid cracking, the material is deemed weldable [33]. In welding, the carbon equivalent carbon (CE) value is used to determine how different alloying elements affect the hardenability of the steel being welded. The CE value is directly related to hydrogen-induced cold cracking, which is a common weld defect. High concentrations of carbon and other alloying elements such as Mn, Si and Ni tend to increase hardenability and decrease weldability [45]. Since HSLA steels have low carbon contents and only small alloy additions, they generally have good weldability. There are a number of different equations in use to calculate *CE*. The most appropriate value depends on the type of steel being considered. For low alloy C-Mn steels with a ferrite-pearlite structure, the most widely used equation is the International Institute of Welding (IIW) formula, which is good for steels with more than 0.18 wt.% C [45, 46]:

$$CE = C + \frac{Mn + Si}{6} + \frac{Ni + Cu}{15} + \frac{Cr + Mo + V}{5} \tag{2.3}$$

The Ito-Besseyo [45, 46] equation is used for low carbon steels with less than 0.18 wt.% C):

$$CE = C + \frac{Mn + Cr + Cu}{20} + \frac{Si}{30} + \frac{V}{10} + \frac{Mo}{15} + \frac{Ni}{60} + 5B \quad (2.4)$$

where the alloying elements in the two equations are expressed in wt.%.

Low *CE* values in the base metal prevent martensite from forming as the weldment cools to room temperature. Martensite is not desirable in the weld metal because of its high hardness which makes the weldment susceptible to high residual stress and easy cracking. For a steel to be easily weldable, it is recommended that the *CE* should be less than 0.41 when using equation (2.3) and less than 0.25 when using equation (2.4) [45]. Steels with *CE* values in excess of 0.41 wt.% are not easily welded because of their increased tendency to form martensite upon cooling. For such steels, preheating prior to welding is required. Both weldability and toughness are achieved with low carbon content and low *CE* values. The loss of strengthening effect due to the reduced carbon content in HSLA steels is compensated for by the addition of small quantities of other alloying elements such as niobium and vanadium. There is a linear relationship between the amount of weld metal ferrite constituents and *CE*. Fleck *et al.* reported an increase of acicular ferrite content from 26 to 85% as the weld metal carbon equivalent was increased form 0.18 to 0.21 [47].

2.6 Structure of Steel Weld Metals

The microstructure that develops in the weld joint is influenced by the chemical composition of the base metal, the filler wire, the flux and the actual cooling rate experienced by the weldment during transformation of austenite to ferrite. Upon

examination after polishing and etching of a completed welded joint, the three distinct metallurgical zones that can be observed are shown in Figure 2.2, namely, the unaffected base metal (BM), the heat affected zone (HAZ) and the fusion zone or weld metal zone (WM).

2.6.1 Heat Affected Zone (HAZ)

The heat affected zone (HAZ) is the area between the weld metal and the base metal. It is the portion of the base metal that experienced temperatures below the melting point, but is heated to temperatures high enough to change its microstructure and alter its properties due to the welding process [2]. The microstructure of the HAZ depends on the peak temperature attained and the length of time spent in the temperature range 800 to 500ºC. The HAZ microstructure may range from thin regions of martensite to coarse pearlite zones. Figure 2.3 is a schematic illustration of the iron-iron carbide phase diagram and the heat affected zone of a welded low carbon steel. The line connecting points A and B show the peak temperatures attained in the HAZ, moving away from the fusion line. The iron-iron carbide phase diagram show how these temperatures relate to the different HAZ microstructures. As shown in the figure, the HAZ consists of four different microstructural zones for plain carbon steel, namely, (i) grain growth zone 1450 to 1100ºC, (ii) recrystallized zone 1100ºC to A_3, (iii) partially transformed zone A_3 to A_1 and (iv) tempered zone below A_1 [1]. The peak temperature attained decreases with increasing distance away from the fusion zone and so also is the grain growth which decreases with increasing distance away from the fusion line. The HAZ regions are designated, respectively, as coarse grained (CGHAZ), fine grained (FGHAZ),

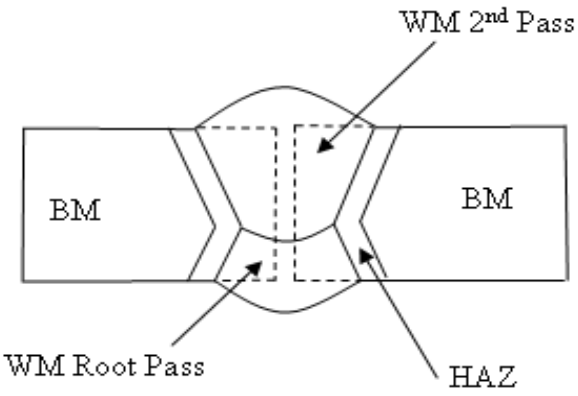

Figure 2.2. A sketch showing the basic regions of a welded joint. (BM = base metal, WM = weld metal and HAZ = heat affected zone).

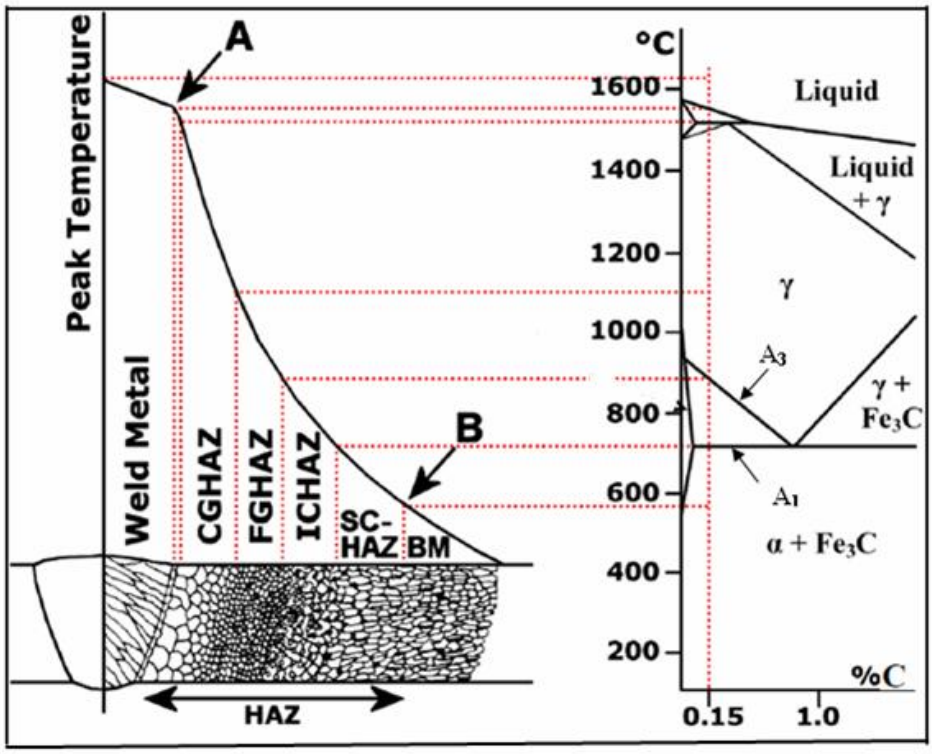

Figure 2.3. Schematic diagram of the heat-affected zone of a 0.15 wt.% C steel indicated on the Fe-Fe_3C phase diagram [adapted from [1]].

inter-critical (ICHAZ) and sub-critical (SCHAZ) zones [24]. Zone 1, coarse grained HAZ (CGHAZ), is the region next to the fusion line. In this zone high temperatures

above the upper critical (A_3) are attained and therefore austenite grain growth occurs. The austenite grain size and the width of the CGHAZ zone increase with increasing heat input and low cooling rate [24, 48].

As high heat input produce low cooling rate, it means that coarser grains will be formed because of the increased length of time spent above the A_3 temperature. Zone 2, fine grained heat affected HAZ (FGHAZ), or recrystallized zone consists of fine ferrite grains. The material in the FGHAZ zone is heated to high temperatures enough to form austenite during the welding process. The peak temperature attained is however not high enough to completely dissolve the precipitates (carbides and nitrides) in this zone as in zone 1. As a result, fine ferrite grains are formed and austenite grain growth is also suppressed. Zone 3, the inter-critical HAZ (ICHAZ), is the partially-austenize region. Ferrite in this region does not completely transform to austenite on heating. Upon cooling, the transformed grains are refined whereas the austenite may transform to pearlite, martensite or be retained as martensite-austenite (M-A) microconstituent. In zone 4, sub-critical HAZ (SCHAZ), as the peak temperature is below A_1, the grain size is not affected because no transformation of austenite occurs. Thus, the austenite grain size within the HAZ is regulated by the upper critical temperature (A_3) of the steel and the weld thermal cycles that were encountered [24, 49].

The mechanical properties of each HAZ zone are different because of the difference in grain size in the zones. In low carbon and low alloyed steels, attention is given more to the CGHAZ because it attains very high temperatures and large austenite grains are produced which result in high strength but low toughness in the weld joint.

The hardness of the different HAZ regions varies gradually, declining from the weld interface to the fine-grained zone. In general, when moving across the HAZ, from the base metal toward the fusion line, the peak temperature experienced increases and so, likewise, the austenite grain size and hardenability increase. High hardness values usually correlate with increased brittleness and reduced ductility.

2.6.2 The Weld Metal (WM)

The weld metal is the fusion zone which on cooling fills the gap between the base plates, and bonds them. It is a mixture of the filler wire, flux and base metal that has melted during the welding process. It consists of a columnar solidification microstructure similar to ‘as cast’ structures [50]. Easterling [1] described the evolution of this columnar microstructure as epitaxial growth because the solidifying grain is a continuation of the base metal grain at the fusion boundary. The reviews by Abson and Pargeter [8] and Grong and Matlock [23] discussed the effect of welding process on the weld metal solidification structure. The columnar grain size and shape can be changed by altering the weld pool shape. The inoculation of the weld pool by inclusions, oscillation of the welding arc, welding current, welding speed and welding voltage all influence the solidification microstructure [51].

2.7 Microstructural Products in a Weld Joint

Austenite (γ-Fe) is stable at temperatures between 1350°C and 910°C for low carbon steels and is the primary microstructure which is maintained during cooling within the temperature range.

On cooling, as mentioned earlier, the microstructural constituents observed using optical microscopy are grain boundary ferrite (GBF), Widmanstatten ferrite (WF) and fine-grained intergranularly-nucleated acicular ferrite (AF) [8]. Small quantities of other microconstituents consisting of mixtures of carbides, sulfides, martensite (M) and retained austenite (RA), which result from untransformed austenite after GBF, WF, and AF have formed, may be observed especially at high cooling rates [26, 47]. It is generally agreed that for low-carbon, low-alloy steel weldment, microstructures which consist primarily of acicular ferrite provide optimum weld joint mechanical properties both for strength and toughness and that the toughness of the weld metals is proportional to the amount of AF [4, 7, 8]. This is because of a basket-weave-type morphology, 1-3 μm in size, which makes acicular ferrite resistant to crack propagation [8]. The formation of other structures, such as GBF and WF, decrease the weld toughness because they provide preferential paths for crack propagation [27, 52].

2.7.1 Allotriomorphic or Grain Boundary Ferrite (GBF)

Allotriomorphic ferrite is the first phase to form on cooling austenite below the A_3 temperature [2]. It nucleates heterogeneously at the austenite grain boundaries and grows with time rapidly covering the boundaries. Increasing the hardenability of the weld metal by addition of alloying elements such as Mn, Cr, Ni, or Mo decreases the amount of allotriomorphic ferrite [28]. Grain boundary ferrite is detrimental to toughness, as it offers little resistance to crack propagation and hence should be kept low in the weld metal.

2.7.2 Widmanstatten Ferrite (WF)

Upon further cooling of a typical weld deposit, after the formation of the initial grain boundary ferrite, two kinds of Widmanstatten ferrite are usually observed [8, 28]. Secondary Widmanstatten ferrite nucleates at the allotriomorphic ferrite and austenite grain boundaries and grows as sets of parallel plates separated by thin regions of austenite into the untransformed austenite. Depending on the rate of cooling, the austenite between the WF plates may be retained to ambient temperature or partially transformed into small quantities of martensite [52]. These small quantities of retained austenite, martensite, carbide and nitride mixtures are called microphases.

The International Institute of Welding (IIW) refers to this Widmanstatten ferrite and its associated microphases as ferrite with aligned martensite-austenite-carbide (MAC) [53]. Primary Widmanstatten ferrite nucleates directly from the austenite grain boundaries which are not covered by allotriomorphic ferrite. Fast cooling, high alloy content have been reported to promote the formation of Widmanstatten ferrite. The growth mechanisms of the two are identical. The WF transformation temperature is just below that of GBF and assumed to begin when the growth of the latter ceases [54, 55]. The formation of Widmanstatten ferrite depends on the austenite grain size and the thickness of allotriomorphic ferrite which formed earlier [24]. Widmanstatten ferrite, like the allotriomorphic ferrite, is regarded as an undesirable constituent because it leads to poor fracture toughness [26, 55].

2.7.3 Acicular Ferrite (AF)

Acicular ferrite has long been recognized to provide both increased toughness and improved strength in steel weld metals and therefore AF is the desirable microstructural constituent in the weld metal [55, 56]. The morphology of AF consists of fine elongated ferrite platelets that are arranged randomly in an interlocking pattern within the austenite grain. The non parallel, disorganized grain boundaries of acicular ferrite hinder crack propagation and impact improved toughness to the weldment [57-60]. The acicular ferrite phase forms at temperatures between 650 to 500ºC predominantly on some inclusions in the weld metals [53, 60]. Under the scanning microscope, acicular ferrite appears as laths fanning from nucleating round inclusions as shown in Figure 2.4. Research has shown that acicular ferrite requires the presence of inclusions to enable intragranular nucleation to start. In addition, it will only form when the austenite grain size is relatively large so that the events which started earlier at the austenite grain boundaries at higher temperatures (GBF and WF) do not suppress its formation within the grain [30].

Acicular ferrite was originally thought to be a form of Widmanstatten ferrite which was nucleated intragranularly [6]. The current understanding is that it is intragranularly nucleated bainite. The difference between acicular ferrite and bainite is that AF nucleates intragranularly on inclusions and its growth is limited by hard impingement with other AF plates which form within the prior austenite grain boundary [60]. On the other hand, bainite forms intragranularly but not on inclusions

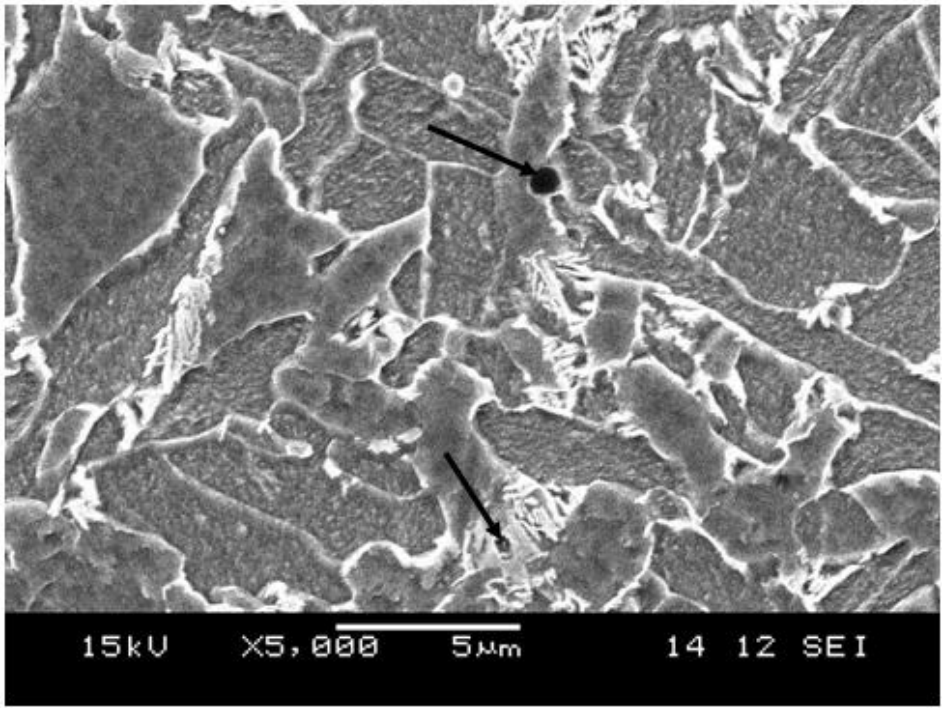

Figure 2.4. Typical SEM micrograph showing acicular ferrite plates nucleated on some inclusions in a SA516 steel weld deposit.

. The transformation of austenite upon cooling is a competitive process between the grain boundary products (GBF and WF) and intragranular ferrite (AF) [49].

2.8 Factors Affecting the Weld Metal Microstructure

The discussion from the previous sections has identified the major factors that influence the development of the microstructure of steel weld metals. They are heat input (*H*), alloy chemistry and weld pool geometry all of which affect the actual cooling rate (*CR*) experienced by the weld joint and, consequently, its microstructure and mechanical properties.

2.8.1 Role of Cooling Rate (CR)

The cooling rate (CR) after a weld pass is a primary factor that determines the structure of the weld metal and heat affected zones in a weld joint. Fast cooling rates may produce martensite whereas slow cooling rates resulting from high heat inputs reduce HAZ hardness [30]. The temperature-time relationship in the welding process consists of a rapid heating period, during which the weld metal attains peak temperatures reaching a maximum of about 1900^{o}C which melts the welding electrode, the base metal and flux materials around the arc. After welding is complete, solidification occurs and is followed immediately by cooling in air to room temperature. During this period heat is transferred by conduction from the molten metal pool to the base metal and creates the heat affected zone [58-61].

In welding of steel, the cooling time from 800 to 500°C ($\Delta t_{8/5}$) during which the austenite decomposition takes place is referred to as "the weld time constant". It is an index which is widely used to access the thermal conditions under which the austenite to ferrite transformation takes place. The weld time constant is proportional to the heat input (H). Based on the solution of the differential equation of heat transfer by Rosenthal [62] and assuming that the physical characteristics of the metal, i.e. thermal conductivity (λ), thermal diffusivity (α) and thermal capacity (c) are independent of temperature, the 'cooling time constant' ($\Delta t_{8/5}$) for thick plates can be approximated using equation (2.5), where H is the heat input in kJ/mm [23].

$$\Delta t_{8/5} \approx 5H \tag{2.5}$$

The ‘cooling time constant’ is approximately proportional to the heat input (*H*). The cooling rate (*CR*), expressed in (°C/s), can be estimated using equation (2.6) [36].

$$CR = \frac{300}{\Delta t_{8/5}} = \frac{300}{5H} \tag{2.6}$$

Figure 2.5 is a schematic diagram showing three weld cooling curves and their corresponding ‘weld thermal constant’ for different welding heat inputs. It can be seen from the figure that as the heat input increased, so also does the weld thermal constant ($\Delta t_{8/5}$) and consequently, the cooling rate decreased. Therefore, high input is associated with reduced cooling rate.

Increasing cooling rate generally will lower the austenite to ferrite transformation start temperatures [17]. When cooled at sufficiently low rate, for example, *CR* = 1ºC/s (i.e., $\Delta t_{8/5}$ = 300 s), the dominant transformation products are grain boundary ferrite and pearlite. As cooling rate increases, if inclusions are present, acicular ferrite will begin to form and eventually pearlite will be eliminated. The weld microstructure can show WF morphologies that grow out of the GBF. At intermediate cooling rate, for example, *CR* ≈ 15ºC/s (i.e., $\Delta t_{8/5}$ = 20 s), the transformation products will be mostly acicular ferrite. At very high cooling rate, for example, *CR* > 200ºC/s (i.e., $\Delta t_{8/5}$ = 1.5 s), lath structures consisting of martensite will develop [63, 64]. For SA516 steel weld, Lundin *et al.* [63] established that maximum toughness was obtained when $\Delta t_{8/5}$ was about 10 s.

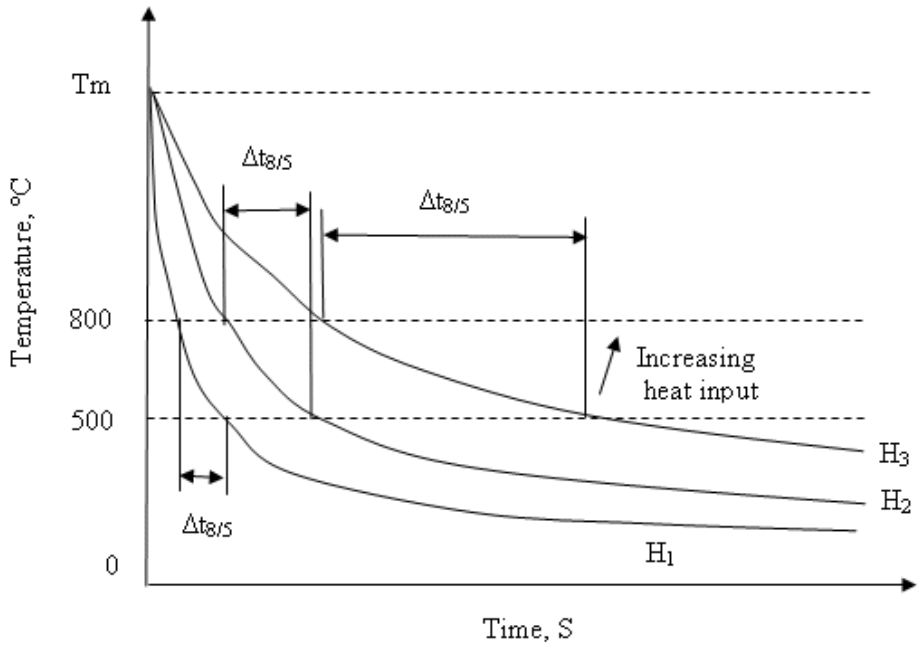

Figure 2.5. Schematic diagram showing weld cooling curves and weld thermal constants ($\Delta t_{8/5}$) for different heat inputs ($H_3 > H_2 > H_1$) [adapted from 21].

Apart from the heat input (and the peak temperature attained), plate thickness and weld joint geometry are other factors that control the cooling rate of the welded joint. The following are examples that show the extent of *CR* dependence on the weld geometry and process parameters: for a low heat input of *H* approximately 1 kJmm^{-1}, on a plate 20 mm-thick the cooling rate is *CR* ≈ 75ºC/s ($\Delta t_{8/5}$ = 4 s), whereas, for a heat input of *H* approximately 4 kJmm^{-1}, the cooling rate will be *CR* ≈ 20ºC/s ($\Delta t_{8/5}$ = 15 s). At this cooling rate, 60% of GBF and WF microconstituents would develop with only 40% transforming to AF [17]. Figure 2.6 is a schematic illustration of the cooling rates in the various HAZ regions and their corresponding hardness measurements. A low heat input is associated with a high cooling rate and the formation of hard martensite hence the weld metal is very hard and brittle.

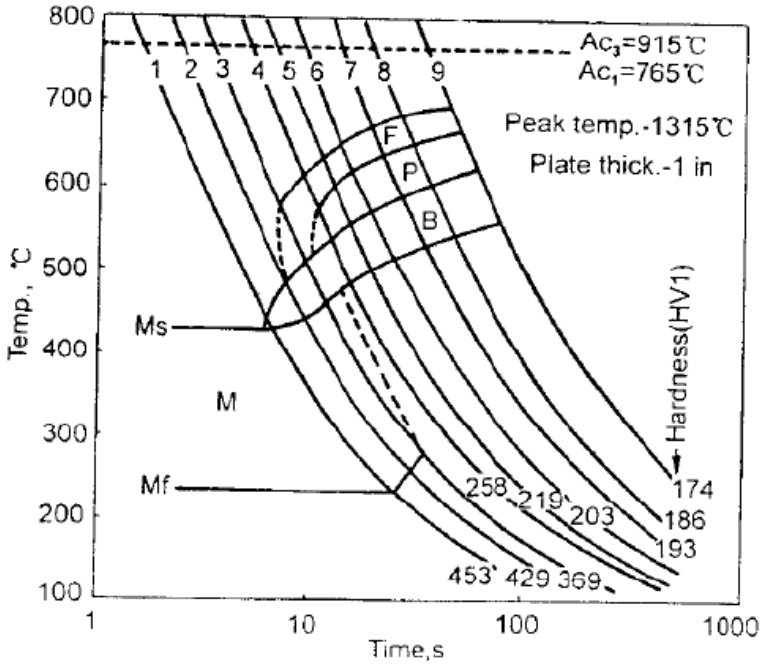

1. H=0.75 kJ/mm, $\Delta t_{8/5}$ = 3.2 s;
2. H=1.10 kJ/mm, $\Delta t_{8/5}$ = 4.8 s;
3. H=1.57 kJ/mm, $\Delta t_{8/5}$ = 6.7 s;
4. H=2.35 kJ/mm, $\Delta t_{8/5}$ = 10.1 s;
5. H=3.15 kJ/mm, $\Delta t_{8/5}$ = 13 s;
6. H=3.94 kJ/mm, $\Delta t_{8/5}$ = 18.4 s;
7. H=4.92 kJ/mm, $\Delta t_{8/5}$ = 27.8 s;
8. H=5.91 kJ/mm, $\Delta t_{8/5}$ = 40.0 s;
9. H=7.87 kJ/mm, $\Delta t_{8/5}$ = 71.1 s

Figure 2.6. A schematic diagram showing the approximate hardness of the various HAZ regions for different heat inputs and cooling rates. Reprinted from [63] with permission.

With increasing heat input, the cooling rate decreases, which allows the weld to dwell longer in the high temperature range. Coarse grains are produced leading to a reduction in hardness.

2.8.2 Cooling Rate Parameter (NA/CI)

Calculating the cooling rate using equations (2.5) and (2.6) does not include either the weld shape geometry or the plate thickness. This means that the actual cooling rate experienced by the weld may not have a linear dependence on the heat input since different weld bead geometries will yield different cooling rates. Experimentally measuring the cooling rate by inserting thermocouples in the weld path was not practicable in this work.

In considering the factors that influence the CR and hence the final microstructure, the cross-sectional shape and geometry of the molten pool produced by the heat input should be taken into account. The resulting cooling rate will depend on the amount of molten metal generated as well as the heat sink available to conduct the heat away. The nugget area (NA) shown in Figure 2.7 is associated with the amount of heat dissipated by the molten weld pool surrounded by the weld cooling interface (CI), also shown in Figure 2.7, and depends on the heat input. The cooling interface represents the area available for conducting heat away from the fusion zone. A cooling rate parameter, which is the ratio NA/CI [13], can be substituted for the actual cooling rate and used. As the value of NA/CI increases, CR decreases and vice versa.

The positive feature of using this parameter is that the weld profile resulting from any combinations of welding parameters is included, which is not possible in the conventional approach using equations (2.5) and (2.6). For example, a high cooling rate parameter (NA/CI) yields a low cooling rate. Hence, the weld will spend a long time at high temperatures. This will cause the formation of large austenite grains. Due to the increased time spent at the high temperature, there is also a great chance of oxygen being absorbed by the slag which will lead to a drop in the volume of inclusions. The decrease in inclusion amount produces large inclusions. These results are consistent with the results obtained using cooling rates that were determined experimentally by inserting thermocouples in the weld path and measuring the temperatures [62]. Thus, the cooling rate parameter gives a good representation of the actual cooling rate the weld experienced.

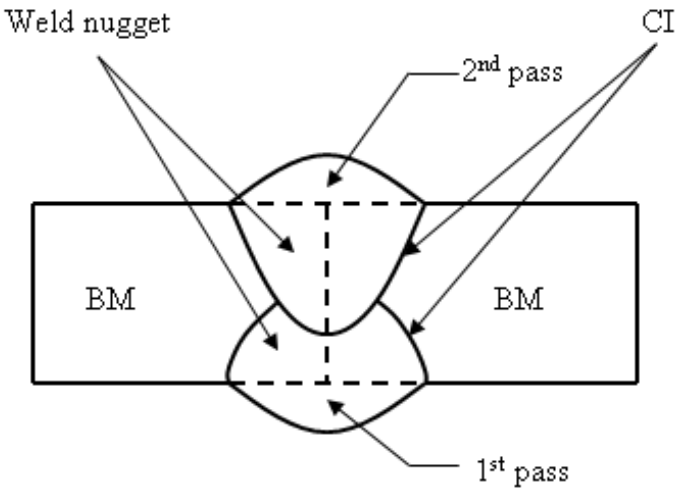

Figure 2.7. Schematic drawing showing a cross-section view of a butt weld joint geometry (BM = base metal, CI = cooling interface).

2.9 Influence of Alloying Elements on Weld Metal Microstructure and Properties

Alloying elements in the weld metals come from the filler wire, the base metal and the flux. Most alloying elements except cobalt (Co) increase hardenability because solid solutions are formed when they dissolve, either interstitially or substitutionally in the weld metals. Small atoms such as carbon and nitrogen occupy the interstitial sites while large atoms such as silicon and magnesium dissolve substitutionally. The increase in strength of ferrite iron by interstitial carbon or nitrogen is much greater than any substitutional alloying element as shown in Figure 2.8 in which the effect of alloy addition on solid solution strengthening of ferrite is illustrated. Amongst the common alloying elements used in steels, C, Ni, Co, Mn and N are austenite stabilizers while Si, W, Mo, V and Nb are ferrite stabilizers [19, 65] and used as such for the intended application.

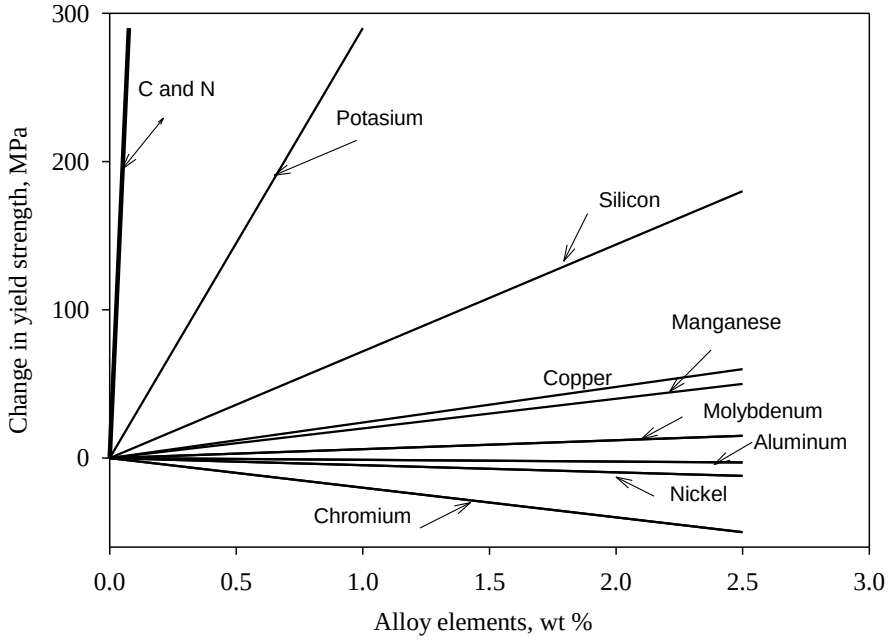

Figure 2.8. Effect of alloy addition on solid solution strengthening of ferrite [65, 66].

Alloying can also be used to refine grains in order to improve strength and toughness. The effect of these alloying elements on the development of the microstructure is reviewed in the following sections.

2.9.1 Carbon

Carbon is the most important element for controlling the microstructure of steel. It is a solid solution strengthener, carbide former, and provides grain refinement and strong hardening effect in steel. Dorshu [67] reported that the solid solution hardening effect of carbon in as-deposited weld metal was stronger than most other elements. Farrar and Harrison [17] and Askeland [68] reported an increase in the amount of carbide and a

refinement of the austenite grain size with increasing carbon content. The strengthening due to carbon is caused by the carbides. However a high level of carbides in the weld metal is detrimental to the microstructure because they can act as crack initiation sites [69].

The solubility of carbon in ferrite is about 0.01%, but this amount is exceeded in most weld metals ranging from 0.05 to 0.15% [17]. Abson and Pargeter [8] and Moll *et al.* [70] reported that increasing carbon content of the weld metal from 0.1% to 0.2% decreased the impact toughness by over 60% and recommend the carbon level in steel welds be kept below 0.1% to prevent extensive martensite formation in the weldment.

2.9.2 Manganese

Manganese is a moderate solid solution strengthener and has a slight deoxidizing effect in weld metals. Manganese, nickel and copper are austenite formers and, therefore, suppress the austenite-to-ferrite transformation temperature (A_3) and slow the rate of austenite transformation. Manganese lowers both ductility and weldability if present in high percentage in high carbon steels [71].

Manganese addition was reported to increase the acicular ferrite nucleation by retarding the growth of grain boundary ferrite. Improvement in toughness through grain refinement in the microstructure with increasing levels of manganese has also been noted [17]. It was also reported that increasing the manganese content from 0.6 to 1.8 wt.% progressively increased AF content whilst reducing GBF and WF [35].

In another study, Evans [40] reported that manganese increased the proportion of AF at the expense of GBF and decreased the austenite grain size in the as-deposited weld metal. Lord [72] observed that high levels of manganese and nickel in steel can prevent δ-ferrite formation entirely so that the weld metal solidifies directly to austenite. The Fe-Mn equilibrium phase diagram shown in Figure 2.9, confirms the observation by Lord. Addition of manganese progressively reduces δ-ferrite phase. Manganese will combine with sulphur in the weld metal to form MnS which has been shown to reduce solidification cracking [5]. Unfortunately, manganese tends to segregate in the weld metal on cooling which results in hardness and microstructural variations of the weld metal, hence its level has to be limited to prevent manganese segregation. Manganese as an inclusion former lowers the toughness of the weld metal [73].

2.9.3 Nickel

The addition of nickel in the weld metal, like manganese, improves toughness and has solid solution hardening effect on the microstructure [74]. Nickel addition lowers the austenite-to-ferrite transformation temperature and reduces the formation of GBF, which favors AF formation. Nickel can be added in large quantities (up to 3.5 wt.%) to produce a refining effect in the structure and increase AF [66]. Evans [40] reported that as the level of nickel increased, the amount of GBF decreased while that of AF increased and became more refined. At high levels above 3.5 wt.%, intergranular martensite was observed to develop between laths of AF microstructure.

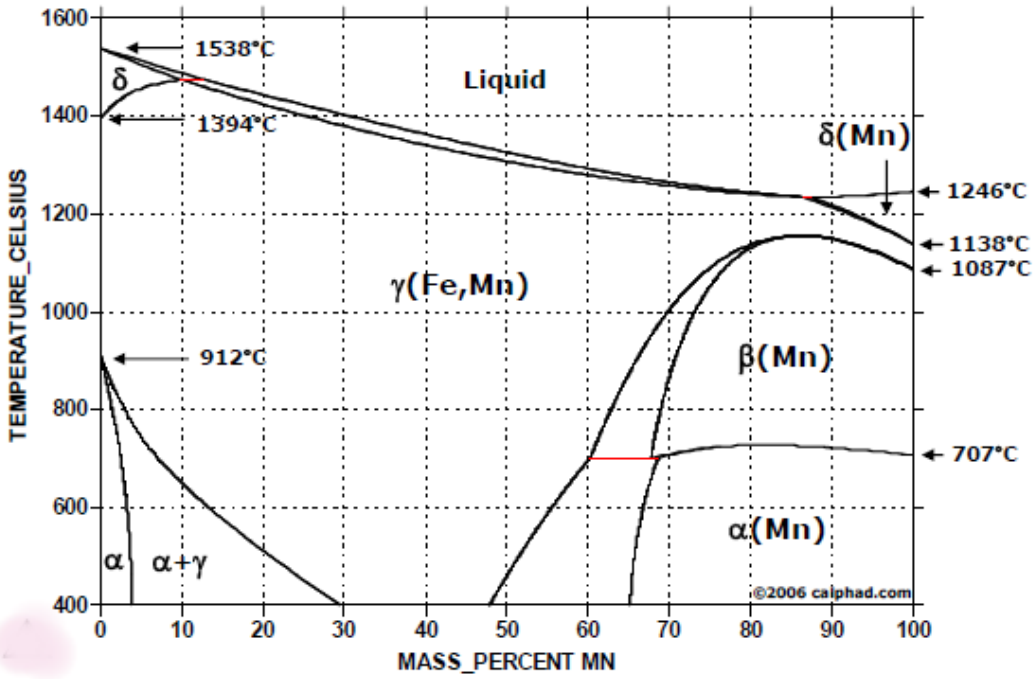

Figure 2.9. The Fe–Mn equilibrium phase diagram [66]

2.9.4 Chromium

Chromium is a ferrite stabilizer, but it slows down austenite-to-ferrite transformation rate [75]. Addition of chromium increases hardenability and strength of weld metals. However, it impairs toughness, but has been reported to promote an increase in the amount of acicular ferrite [75]. Chromium has a great influence on the weld metal microstructure when manganese is at low concentrations [75]. It has been reported in studies of mechanical properties of weld metals of HSLA steels that increasing chromium levels decreased toughness [74, 75].

2.8.5 Silicon

Figure 2.8 shows that silicon contributes greatly to ferrite solid solution strengthening. The addition of 1.5 wt.% silicon was reported to increase yield strength in carbon steels by 110 MPa [33]. The role of silicon on the weld microstructure, however, is not entirely clear. For example, it was reported that a silicon level > 0.5 wt.% is detrimental to weld metal toughness [17]. On the contrary, other researchers reported that silicon addition in the range 0.35 to 0.8 wt.% had no effect on the weld metal microstructure [69, 76]. A change from Widmanstatten to acicular ferrite structure as the silicon content increased from 0.2 to 0.4 wt.% was also reported. The role of silicon in the range 0.2 to 0.94 wt.% was reviewed in [40] and it was concluded that a high level of silicon promoted AF formation.

2.9.6 Titanium, Niobium and Boron

Titanium and niobium form carbo-nitrides which improve strength and toughness in steel weld metals through precipitation hardening [77, 78]. Titanium reacts with oxygen in the weld metal to form oxide inclusions of Ti(C, N, O), which provide nucleation sites for acicular ferrite formation. Inclusions containing Ti and Nb have been reported as good nucleating sites for AF. Nevertheless, high Nb content has been reported to reduce the AF amount in the weld metal as GBF and WF increased resulting in decreased weld metal toughness [78]. Boron enhances strength and toughness in the weld metal because it suppresses the formation of GBF [79]. Babu *et al*. [80] reported that boron levels in the range 20 to 40 ppm a large influence on the microstructure and increased hardness of weld seams. Evans [40] studied the effect of Ti and B on the

microstructure and properties of C-Mn shielded metal arc welds. He concluded that Ti enhanced the formation of AF in the weld metal. Oh *et al.* [81] concluded that Zirconium-boron additions to the weld metal of a low carbon steel provided an increase in the AF nucleation on the inclusions in the weld metal.

2.9.7 Aluminum

Aluminum is a strong oxide and nitride former in the weld metal. It was reported in [23] that the average inclusion diameter increased with weld metal aluminum content and this resulted in grain coarsening and increased inter-inclusion spacing. On the contrary, the formation of aluminum nitrides which pinned grain boundaries and suppressed austenite grain growth was also reported. A complex interaction between titanium-aluminum-oxygen was reported by Bailey [79]. It was suggested in this work that aluminum could reduce titanium content and limit the formation of titanium oxide, which is considered necessary for AF nucleation. Oldland [82] indicated that changes in the flux type would alter the effect of aluminum. He found that for a fully basic flux, increasing the aluminum content reduced the formation of AF and favoured GBF. However, in a semi-basic flux the effect was small. He concluded that since the oxygen level in the weld metal was raised through changes in the flux type, the optimum value of aluminum associated with the formation of AF was also increased. Grong and Matlock [23] suggested there is a critical oxygen/aluminum ratio for AF formation in the weld metal. They found that the lowest Charpy 35 J temperature (and hence the maximum AF content) was obtained when the ratio $(\%Al)/(\%O)^2 = 28$. Above this

level, the inclusion size increased rapidly and the number of suitable nucleation sites for AF formation was substantially reduced.

2.9.8 Oxygen

Oxygen exists in the weld in the form of finely dispersed oxygen-rich inclusions. The main sources of weld metal oxygen are: (1) decomposition of the flux constituents and (2) contamination from the atmosphere. The flux is the major source of oxygen and different fluxes produce different weld metal oxygen levels. The oxygen pick up from the atmosphere is minor and can be reasonably controlled. Chaveriat *et al*. [71] and Chai and Eager [83] reported that weld metal oxygen content was influenced by the flux used in welding. Terashima *et al.* [84] showed that oxides in steel weld metals can improve toughness. They reported that oxygen content of less than 200 ppm was insufficient to form enough potent inclusions to nucleate AF. As a result, GBF and WF were formed.

However, increasing the oxygen content above 550 ppm generated very many oxide inclusions which suppressed prior austenite grain growth by pinning the grain boundaries. As large austenite grains are necessary for the nucleation of AF, only GBF is able to form which reduces the toughness of the weld metal. For C-Mn steel welds, these authors recommended that the optimal weld metal oxygen level should be between 240 to 340 ppm. Ito *et al.* [85] reported that in Fe-Si-Mn-Ti-B steel weld metal, AF was formed at oxygen level above 270 parts per million (ppm), but GBF and WF were the predominant microstructure at oxygen levels above 440 ppm. At oxygen levels below 60 ppm, bainite was formed.

They noted also that weld metal oxygen content increased with increasing welding speed (reducing heat input), but decreased with increasing welding heat input.

2.9.9 Nitrogen

Nitrogen is not a deliberate alloying addition in steel welds. It is picked up from the interaction of the base metal, flux and the environment during welding. Its concentration is kept low as a high concentration is detrimental to toughness of the weld. Although nitrogen raises strength, it reduces the toughness of the weld and may also cause weld metal porosity [17]. With a well-designed welding procedure, the amount of nitrogen in the weld metal can be kept close to that of the parent metal. In so doing, its effect on the properties of the weldment can be minimized.

2.10 Weld Metal Inclusions

Large volume fraction of acicular ferrite is beneficial for the toughness of steel welds because the chaotic, interlocking nature of the AF microstructure impedes crack propagation. Oxide and nitride inclusions are important because AF nucleates on them [8, 14, 36, 77, 84]. If no inclusions are present, bainite rather than acicular ferrite may result. Bainite offers little resistance to crack propagation and, therefore, is detrimental to the weld metal toughness.

2.10.1 Composition of Inclusions

Inclusions in the weld metals come primarily from the reaction between dissolved Al, Ti, Si and Mn with dissolved O, S and N. Due to the high thermal cycles attained during

welding and the limited time available for growth and separation of particles, the amount of inclusions in weld metals is high. As previously mentioned, inclusions restrict the growth of the austenite grains but also provide nucleation sites for AF [8, 77]. Since the main source of oxygen in the weld metal is the flux which contains oxides such as Al_2O_3, SiO_2, MnO and TiO_2, the flux chemistry affects the chemistry and morphology of inclusions. The average inclusion size in weld deposits is 0.3-1.0 μm [85, 86]. The volume fraction of inclusions has been determined to correlate with the total oxygen content in the weld because most of the oxygen is present in the form of oxides and most of the inclusions are oxides [71].

2.11 Weld Solidification and Prior Austenite Grain size

Solidification in low alloy steel weld deposits starts with the epitaxial growth of δ-ferrite from the base plate at the fusion boundary [51]. Due to the large temperature gradient between the solid-liquid interface, solidification has a cellular shape with the major axis oriented along the direction of maximum the heat flow. On further cooling, austenite allotriomorphs nucleate at the δ grain boundaries. If the cooling rate or carbon content is high enough, then austenite will solidify directly from the melt and grow epitaxially from the fusion boundary. The austenite grain size at this stage could be very large, about 100 μm wide and 3000 μm long [12]. Several researchers have indicated that the number density of weld metal inclusions affects the size of the austenite grain size [8, 87, 88]. They concluded that increasing the inclusion number in the weld metal will lead to a decrease in the prior austenite grain size because of grain boundary pinning.

For a given thermal cycle, the prior austenite grain size increases with decreasing oxygen concentration [89]. The volume of inclusions was found to correlate with the total oxygen content of the weld metal, which was present in the oxides. For a rough estimate of the columnar prior austenite grain size, the following equation is used [39]:

$$L = 154.6 - 2228(C) - 10.56(Si) + 33.77(Mn) - 0.1133(O) + 0.5604(H) \quad (2.7)$$

where, L is the grain size measured in a direction perpendicular to the major axes of the columnar grain in μm, H is the gross heat input in kJ/mm and the chemical compositions are in wt.%.

Investigations carried out by several researchers showed that austenite grain size influences the proportions of the austenite-to-ferrite transformation products [14, 46, 87]. Prior austenite grain boundaries are the nucleation sites for high temperature ferrite products [71]. When the austenite grain size is large, the grain boundary area reduces and less high temperature grain boundary ferrite is formed. This provides conditions for lower temperature acicular ferrite to form. The austenite grain size thus affects the CCT curve. Farrar *et al*. [49] asserted that the austenite grain size influenced the transformation behaviour of the weld metal. They found that increasing the grain size depressed the start temperature of grain boundary ferrite and slightly increased the acicular ferrite start temperature. Easterling [1] also reported that the start temperature of GBF formation reduced with increasing prior austenite grains.

2.11.1 Microphases

Though acicular ferrite is the most desirable weld metal microstructure, it is not the only factor that determines high strength and toughness in steel weld metals. It was reported that microphases, which are martensite-austenite constituents, have a deleterious effect on toughness of low carbon steel weld metals [90]. The microphases in the weld metal are a mixture of small quantities of retained austenite and martensite. Microphases can be found among the plates of acicular ferrite or located between the Widmanstatten ferrite plates and appear as fine dispersion islands when viewed under the optical microscope [26].

2.11.2 Summary

This concludes the review of the literature of the major factors that affect the development of the microstructures in the weld metals and heat affected zones in plain carbon and alloy steels during the welding process. The transformation of austenite to ferrite in the weld is associated with characteristic microstructures which are dependent on welding process parameters. The experimental methods that were used in this study follow in the next chapter.

CHAPTER 3 MATERIALS AND EXPERIMENTAL PROCEDURES

3.1 Experimental Methods

Five main experimental techniques were used in this investigation. The general flow chart of the experimental procedures used is illustrated in Figure 3.1. Inductively coupled plasma optical emission spectroscopy (ICP-OES) and energy dispersive X-ray spectroscopy (EDS) techniques were used for chemical analysis of weld metals and inclusions. Characterization of the weld metal microstructure and precipitates identification were done with optical microscopy (OM), scanning electron microscopy (SEM), powder X-ray diffraction and EDS and transmission electron microscopy (TEM).

3.2 Materials

The materials used in this study were American Society of Mechanical Engineers (ASME) SA516 grade 70 and American Society for Testing and Materials (ASTM) International A709 grade 50. The SA516 steel was in the as-rolled condition while the A709 steel was in the normalized condition. The weld joints that were used for this study were provided by Hitachi Canadian Industries (HCI) Limited, Saskatoon.

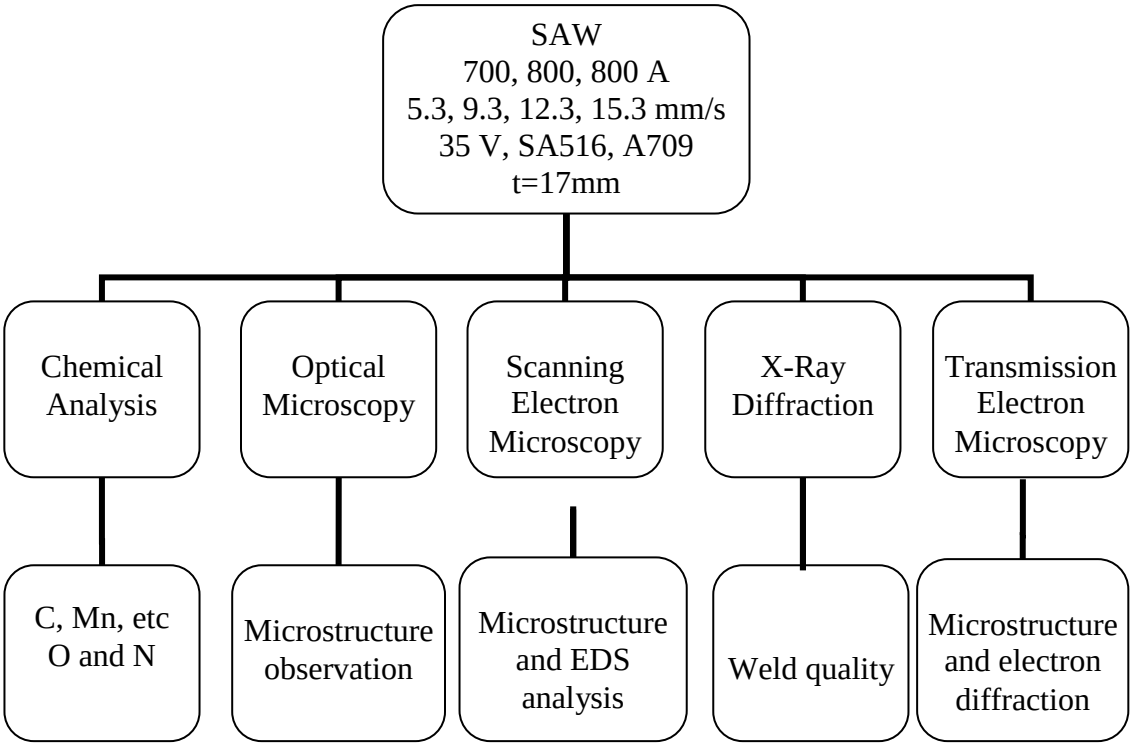

Figure 3.1. **A** flow chart illustrating the experimental procedures used in this investigation.

The welding machine used to produce the welds was a Lincoln Idealarc CD-1000 equipped with Lincoln NA-5 controller. The electrode used for welding was a 4 mm diameter copper-coated welding wire with the Elektrica Svetsnings Aktiebolaget (ESAB) Spoolarc 81 designation, which is classified by the American Welding Society (AWS) as No. EM12K. The welding electrode was a manganese-containing electrode manufactured from silicon-killed steel. The flux used was an agglomerated high impact bonded aluminate basic flux with the OK Flux 10.72 designation. This flux was designed especially for applications requiring high toughness at low temperatures down to - 50^{o}C. Its basicity index (BI) is 1.9.

3.2.2 Acceptance of Mill-Test Reports

Review and acceptance of material test reports is a mandatory requirement by the National Board Inspection Code NBIC RA-2151-I [91]. The mill test reports supplied by the manufacturer were first compared with ASTM tables for the specified steel grades and found to be within range. The chemical compositions of the as-received base plates were further verified against the mill test reports using inductively coupled plasma optical emission spectroscopy (ICP-OES), located in the Department of Geological Sciences, University of Saskatchewan. The results of the mill test report check analysis for SA516 base metal chemical compositions are shown in Table 3.1. The standard error was obtained by dividing the sample standard deviation by the square root of the number of samples. The results obtained are consistent with the composition analysis provided by suppliers. On the basis of these results, the mill-test reports as supplied were accepted and used for the investigations. Table 3.2 shows the chemical compositions of SA516 and A709 steels and the electrode. The phase compositions of the flux are shown in Table 3.3. The carbon equivalent values for the SA516 and A709 steels were calculated using equations (2.3) and (2.4) to be 0.41 and 0.14, respectively.

3.3 Experimental Weld Metals

The weld joints analyzed in this work were shop produced by the HCI personnel. The base plates were cut into approximately 915 mm x 122 mm x 17 mm strips, cleaned with a steel wire brush and compressed air before they were submerged arc welded using an ESAB Electric Welding machine and EM12K welding wire electrode and ESAB OK 10.72 flux.

Table 3.1. Comparison of measured chemical composition with supplied mill-test report for SA516 steel plate.

	Si	P	Mn	Cu	Ni	Mo	Cr
Lab	0.195	0.019	1.195	0.021	0.012	0.003	0.032
HCI	0.240	0.019	1.140	0.020	0.010	0.002	0.020
Std. Err	0.022	0.000	0.027	0.005	0.001	0.005	0.002

Lab = ICP-OES results from University of Saskatchewan, Department of Geology.
HCI = Mill test reports obtained from Hitachi Canadian Industries, the materials supplier. Std. Err = standard error

Table 3.2. Chemical compositions of ASME SA516 and ASTM A709 steels and welding electrode AWS No. EM12K as supplied.

Material	Elements (wt.%)											
	C	Mn	Si	S	P	Cu	Cr	Ni	Mo	Nb	V	Ti
SA516	0.220	1.140	0.240	0.008	0.019	0.020	0.010	0.010	0.002	0.004	--	0.004
A709	0.040	1.30	0.060	0.007	0.010	0.310	0.090	0.140	0.040	0.045	0.003	0.010
EM12K	0.010	0.990	0.240	0.010	0.006	0.130	--	--	--	--	--	--

Table 3.3. Chemical composition of ESAB OK 10.72 flux as supplied (BI = 1.9).

Material	Elements (wt.%)			
	SiO_2+TiO_2	CaO+MgO	Al_2O_3+MnO	CaF_2
ESAB OK 10.72	20	30	25	20

The strips with no edge beveling were butt-welded in the flat position with a single pass on each side. To avoid moisture contamination, the flux was dried in an oven at 350 °C for 2 hours before use. Since the calculated carbon equivalent values for the base metals were 0.41 (SA516) and 0.14 (A709), it was pre-determined that no additional preheat or

post-weld heat treatment was required. The SAW was performed using direct current, electrode positive with an initial electrode extension of 22 mm.

The welding voltage was kept constant at 35 V for all the welds. To obtain sufficiently wide range of weld heat input, three welding currents (700, 800 and 850 A) and four arc travel speeds (5.3, 9.3, 12.3 and 15.3 mm/s) combinations were used to fabricate twelve samples each for SA516 (PV) and A709 (WT).

For each welded joint, one side was initially welded at room temperature, air cooled in the shop with the slag on and then flipped over to weld the other side. On account of this technique the interpass temperature between the two weld passes ranged between 80 and 100°C, thus giving the second side a small preheat. After welding, the welded joints were allowed to cool in air with the unfused slag until the temperature dropped below 100 ºC. The slag was finally removed by slight tapping with a chipping hammer. The weld joints were brush cleaned thoroughly and visually and ultrasonically inspected for weld defects like undercuts, excess reinforcement, weld bead shape and weld metal burn-through. The test specimens were prepared from the sections of the welds without defects. The test specimens with their corresponding SAW process parameters used are shown in Table 3.4. A schematic of the joint geometry used for the test welds is shown in in Figure 3.2.

Table 3.4. SAW parameters used for welding test samples.

SA516	A709	Voltage(V)	Current (A)	Speed (mm/s)
PV0*	WT0*			
PV1	WT1	35	700	5.9
PV2	WT2	35	700	9.3
PV3	WT3	35	700	12.3
PV4	WT4	35	700	15.3
PV5	WT5	35	800	5.9
PV6	WT6	35	800	9.2
PV7	WT7	35	800	12.3
PV8	WT8	35	800	15.3
PV9	WT9	35	850	5.9
PV10	WT10	35	850	9.2
PV11	WT11	35	850	12.3
PV12	WT12	35	850	15.3

* PV0 and WT0 are SA516 and A709 parent metals.

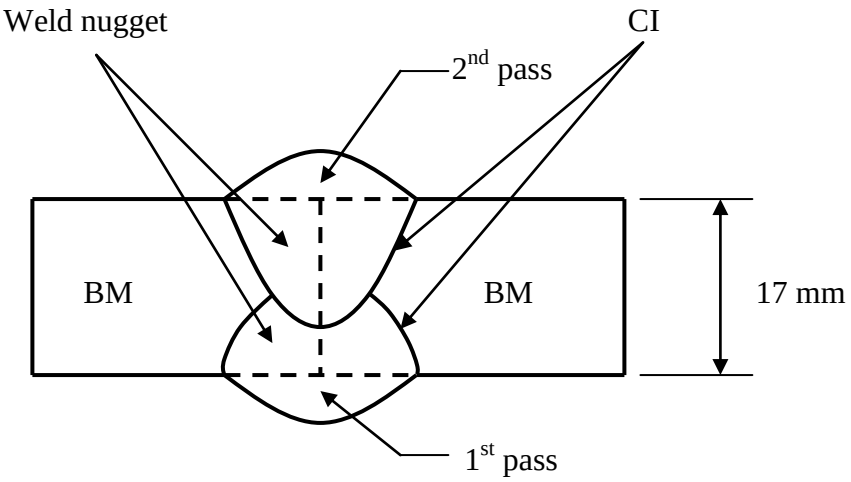

Figure 3.2. Schematic drawing showing a cross-section view of a butt weld joint geometry (BM = base metal, CI = cooling interface).

3.4 Sample Preparation

The initial sample preparations for both chemical analysis and for metallographic examinations were the same. Three samples of each welded joint and the base metals were prepared. The samples from each welded joint contained the fusion zone, the heat affected zone and the base metal. The samples were prepared in accordance with ASTM E3 standard metallographic technique [92]. The sample preparation included sectioning, grinding and polishing as well as etching.

3.4.1 Sectioning

Test samples measuring approximately 20 mm long x 15 mm wide were cut transverse to the weld joint with a Buehler Abrasimet abrasive Cutter located in room 2C24 the engineering building. The weldment was kept cool by a continuous flow of lubricant during cutting. Each section included the fusion zone, the heat affected zone and the base metal.

3.4.2 Grinding

After cutting, the samples were first rough ground using a LECO BG 20 belt grinder located in room 2C24 the engineering building with 120 grit silicon carbide grinding paper. This was followed by grinding on a Buehler Handimet II roll grinder using different grades of emery cloth (silicon carbide grit papers) successively increasing fineness from 240, 320, 400 and 600. Between each grinding step, the specimens were rinsed with water, visually inspected and rinsed with methanol. Grinding was done until all the scratches on the samples surface disappeared.

3.4.3 Polishing

Polishing of the samples was performed in two steps. In the first step, polishing was done using 6 μm diamond paste on a polishing wheel covered with HS Blue polishing cloth. In the second step, polishing was done using 1 μm diamond paste on a nylon cloth. The samples were rinsed with methanol between each polishing step. The Nikon YM-EPI light optical microscope located in room 2C26 the engineering building was used to monitor the sample preparation process.

3.4.4 Etching

The samples prepared for inclusion size and size distribution measurements on the SEM were not etched after polishing to 1 μm finish. The remaining polished samples were etched in standard 2% Nital (2 Vol. % nitric acid and 98 Vol. % alcohol) solution for about 10 to 15 s to reveal the weld profile showing the base metal (BM), the heat affected zone (HAZ) and the weld metal (WM). The prepared samples were dried by

blowing hot air, labeled and stored in a desiccant chamber. This is an air tight glass chamber with a layer of “Drierite” granular drying agent at the bottom. It is used to maintain a dry atmosphere to protect samples held inside it against corrosion, rust and other deterioration. The samples were taken as needed for the various tests and investigations which included chemical composition analysis, optical microscopy (OM), scanning electron microscopy (SEM) and energy dispersive X-ray spectrometry (EDS). Sample preparation for TEM observation however required different methods of preparation and will be discussed in section 3.8.

3.5 Weld Metal Chemical Composition

In the preceding chapter it was noted that alloying additions to steels, i.e., C, Mn and Si have large effects on the transformation microstructure and properties of the weld metals as solid solutions are formed when these elements dissolve in iron either interstitially or substitutionally. Other elements that can be present in the molten weld pool such as O, N, Al, Ti, Si and B also form inclusions which influence the final weld microstructure. The chemical composition of the weld metal is of primary importance in this study because the affect the obtained microstructure.

The C and S contents of the weld metals were analyzed by a combustion method using the LECO EF-400 carbon-sulphur analyzer. O and N contents were analyzed by inert gas fusion method in a LECO TC-436 furnace located at ESCO Limited, Saskatoon (formerly Quality Steel). For the analysis, approximately 5 g of the weld metal was obtained by drilling from selected areas of the prepared samples as shown in Figure 3.3.

The wt. % of all the other elements in the weld metal, i.e., Mn, P, Si, Cu, Ni, Al, Ca, Nb, Mo and Ti were measured using a Baird DV-4 optical emission spectroscope (OES) located at Evraz, Regina Steel (formerly IPSCO). The OES data were obtained from the marked WM areas shown in Figure 3.3. Three test spots were analyzed for each test sample and averaged to determine the composition of the WM.

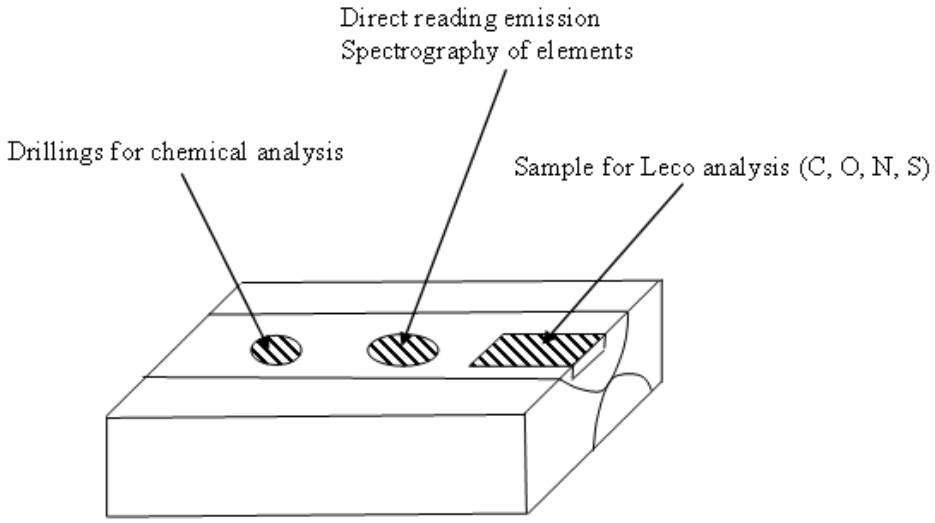

Figure 3.3. An illustration of weld metal sections used for chemical analysis.

3.6 Macrostructural Examination

After polishing and etching, the weld profile showing the weld metal, the heat affected zone and the base metal was visible even to the un-aided eye. Structures that are coarse that can be distinguished by the un-aided eye or under low magnifications are termed macrostructures. Photographs of the weld profile were taken with a Hitachi HDC 1409 digital camera located at the Western College of Veterinary Medicine, Saskatoon. These photographs were used to evaluate variations in weld nugget shape.

3.6.1 Weld Nugget and HAZ width Measurements

The weld nugget size measurements were made from photographs of the weld profile by tracing around the weld metal zone and measuring the enclosed nugget area (NA), which includes the weld penetration area (A_p) and the weld reinforcement area (A_r) and the cooling interface length (CI) as shown in Figure 3.4.

The width of the heat affected zone (HAZ) was measured as shown in Figure 3.4. The IMAQ Vision Builder 5.0 software (National Instruments Corporation, Austin, USA) was used for the measurements. For each weld sample, a minimum of three measurements were taken.

3.7 Examination and analysis of HAZ and WM Microstructures

Observation of and acquisition of micrographs from the prepared specimens were carried out at various magnifications for the weld metals and heat affected zones. Optical micrographs were acquired with a Nikon inverted optical light microscope, Eclipse MA-100, located in room 2C25 in the engineering building which is equipped with a 35 mm PAXCAM-3 camera and interfaced with the PAX-it image analysis software.

3.7.1 Scanning Electron Microscopy

SEM study was carried out at the materials characterization laboratory, University of Manitoba, Winnipeg. A JOEL JSM-5900V SEM equipped with light element INCA energy dispersive X-ray spectroscopy (EDS) was also used to acquire micrographs of

the weld metals and inclusions at high magnification. The EDS was used to analyze the chemical compositions of inclusions.

For scanning electron microscopy, the sample for observation was mounted onto the SEM specimen stage with a graphite tape. Though steel is electrically conductive, the graphite tape was necessary to ensure beam stability.

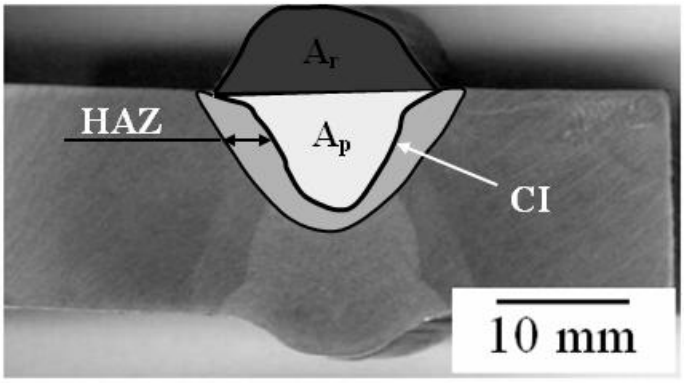

Figure 3.4. A photograph of a typical cross-section of the butt-welded joint showing the cooling interface (CI) and the heat affected zone (HAZ). A_p = weld penetration area and A_r = weld reinforcement area.

Micrographs of the weld metals of the two steels at different magnifications and from different regions were acquired. Images from the polished and etched and polished but unetched samples were acquired.

The acquired micrographs were used in the following analysis: (1) ferrite grain size measurements in accordance with ASTM E 112 standards with the PAX-it software; (2) determination of relative amounts of the constituting ferrites (i.e., AF, WF, and GBF) in the weld metals for different welding current and welding speed combinations; (3) inclusion morphologies and size and (4) prior austenite grain width measurement.

The prior austenite grains were delineated by the GBF and were easy to identify. Their widths were determined using the modified ASTM E 112-96e2 procedure [46]. In this method, intercept lines were drawn perpendicular to the major axes of the columnar grains and measured. Figure 3.5 shows a photomicrograph of a typical weld metal and an illustration of how the prior austenite grain width was measured.

3.7.2 Inclusion Size Measurement

SEM micrographs of the inclusions present in the weld metals were acquired using polished but unetched metallographic weld samples. For the inclusion size measurement, the acquired SEM micrographs were imported into the PAX-it software and calibrated. The analysis focused on the spherical inclusions because they were found to provide nucleation sites for AF.

3.7.3 X-ray Diffraction (XRD)

X-ray diffraction measurements were carried out on WMs of the two steels to determine if there was retained austenite within the weld metals. The X-ray diffraction samples were obtained by drilling out shavings with a diamond drill-bit. The shavings were collected and cleaned in alcohol to remove any oil, dust and other contaminations. After drying with a stream of hot air the shavings were placed in a test tube and stored in a desiccant chamber for use. A 3 kW Rigaku GFX-RAD3D X-ray diffractometer located in the Department of Geological sciences, University of Saskatchewan using a copper target and a Ni filter producing Cu K_α radiation ($\lambda = 0.15418$ nm) was employed. The

working voltage and current were 40 kV and 150 mA, respectively. X-ray diffraction spectra were acquired in the 2θ angle from 20 to 120 degrees.

From the diffraction peaks from the spectrum acquired, the presence or absence of austenite can be reasonably established. In this analysis, the five diffraction peaks in the spectrum were used in accordance with the Joint Committee on Powder Diffraction Standards (JCPDS) [93].

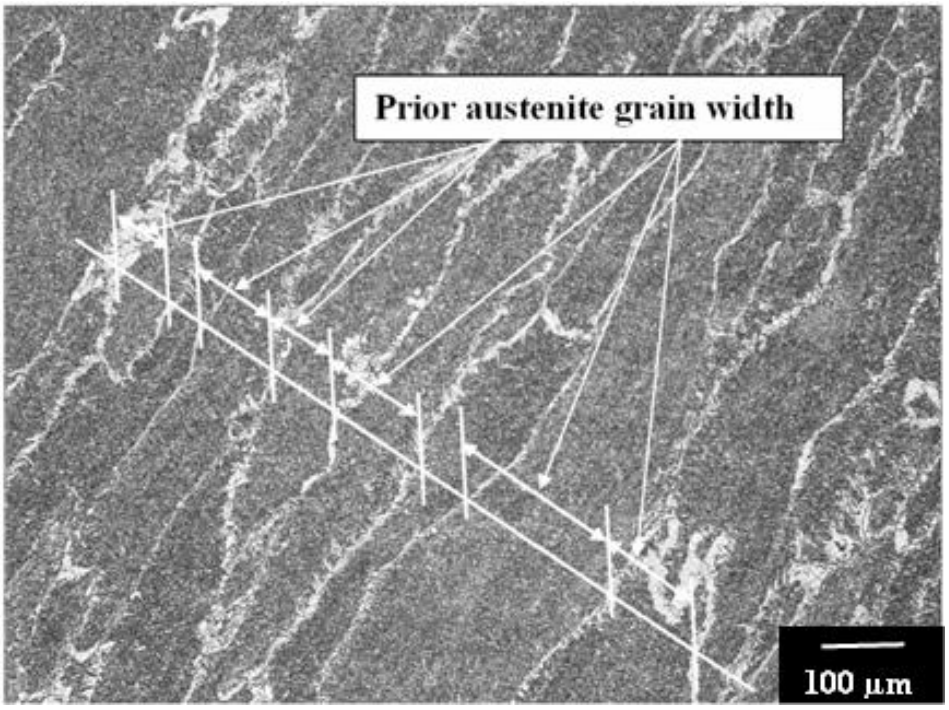

Figure 3.5. Photomicrograph of the weld metal illustrating the measurement of the prior austenite grain width.

3.8 Transmission Electron Microscopy (TEM)

TEM was used to analyze the WM inclusions more closely to help understand the AF development. Thin-foil samples prepared from A709 weld metal and carbon replica samples from SA516 weld metal were investigated.

3.8.1 Thin Foil Preparation

Thin slices about 1-2 mm thick were cut from the weld metal of the sample using a thin diamond-tipped circular saw with Imptech-Europe precision cutting machine located in room 2C26 Engineering Building. The cut slice was then mounted in a brass block and ground using 600-grit emery cloth to about 200 μm thickness.

Several 3 mm-diameter disks were then punched from the 200 μm slices. The disks were mechanically ground to a thickness of ~100 μm on 1200 grit SiC paper before electropolishing. The specimens were electropolished to electron transparency using a Struers Tunepol-3 jet electropolisher (located at the Materials Engineering Department, University of British Columbia, Vancouver) at 55 V and 15 A in an electrolyte of 5 vol.% perchloric acid, 25 vol.% glycerol in 70 vol.% ethanol at room temperature.

3.8.2 Carbon Extraction Replica Preparation

Carbon replica extraction technique was used to study the microstructure of the WM inclusions. The main advantage of replicas over thin foil specimens is that they eliminate any effect due to the iron matrix and thus enable the chemical composition of the inclusions to be determined more accurately. Samples used for making replicas were ground and polished with 1 μm diamond paste to a high surface finish and lightly etched with 2% nitric acid in ethanol. A thin film of carbon approximately 20 nm-thick was evaporated in a vacuum of ~10^{-5} torr on the etched WM surface. The thickness of the film was a critical factor because a very thin film would be destroyed by the electron

beam. In contrast, a thick film would be impossible to lift from the specimen surface. The coated surface was cut with a razor blade into 3 mm squares. The deposited film was then removed by etching in a solution containing 20 Vol. % nitric acid in methanol. The replicas were captured and dried on 400 square mesh copper grids for examination in a Hitachi H800 TEM at 200 kV located at the Materials Engineering Department, University of British Columbia, Vancouver. Figure 3.6 shows a schematic illustrating the carbon extraction replica procedure.

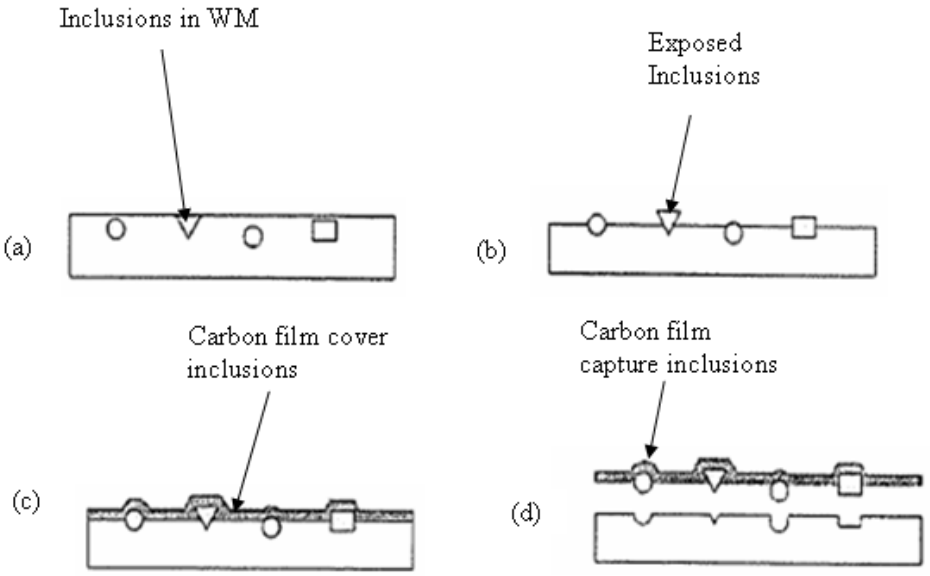

Figure 3.6. Schematic illustrating the carbon extraction replica procedure: (a) polished WM with embedded inclusions, (b) inclusions exposed on sample surface after etching, (c) carbon spray coat on over inclusions and (d) extracted carbon spray coat with inclusions.

3.9 Regression Model Development

It was mentioned previously that the welded joints investigated in this research were supplied by Hitachi Canadian Industries (HCI) Limited Saskatoon and as a result, the independent input variables of current (I) and speed (S) and their limits were predetermined by the company. Optimization of the SAW process variables within the

boundaries of the welding parameters set by HCI was done to determine the best combination of current and speed that provided the maximum acicular ferrite amount. Regression analysis was used to develop a mathematical model. The dependent or response variables that were measured, such as various ferrite amounts, oxygen level and prior austenite grain size, can be expressed [94] as:

$$Y = f(I, S) \tag{3.1}$$

where, Y is the dependent or response variable, I is the current and S is the welding speed.

A model with two independent variables, each in quadratic form with interaction, was chosen to represent the response. For two variables, the equation can be represented [95, 96] as:

$$Y_i = \beta_0 + \beta_1 I_i + \beta_2 S_i + \beta_3 I_i^{\,2} + \beta_4 S_i^{\,2} + \beta_5 I_i S_i + \varepsilon_i \tag{3.2}$$

The response surface for the model is expressed as:

$$Y = \beta_0 + \beta_1 I + \beta_2 S + \beta_3 I^2 + \beta_4 S^2 + \beta_5 IS + \varepsilon \tag{3.3}$$

Equation (3.3) is the equation of a conic section, where, β_0 is the free term of the regression equation (i.e., the intercept of the response surface), β_1, β_2, are the linear terms, indicating the response change when I or S is held constant, β_3 and β_4 are the quadratic terms, β_5 is the interaction term and ε is the error term.

3.9.1 Model Evaluation

The adequacy of the model was checked with residuals obtained and tested by ANOVA technique. The calculated model *F*-statistic values were compared to tabulated expected *F*-distribution values using the degrees of freedom associated with the independent variables and standard errors. The model is valid if the calculated model *F*-statistic value is greater than the expected *F*-distribution value. The significance of the predicted regression coefficients was determined using the *t*-statistics test at 95% confident level. Generally, for 12 observations used in this study, when the *t*-statistic is greater than or equal to 1.796 in absolute value, the coefficient is almost certainly significant at $\alpha = 0.05$ (95% confidence level), [94]. The sign of the *t*-test indicates whether the relation between the independent variable and the dependent variable is direct or inverse. The *F*-statistic is the ratio of the mean sum of regression (MSR) to the mean sum of error (MSE). SYSTA-11 statistics software was used for the model analysis. A typical ANOVA Table for multiple non-linear regression model analysis is shown in Table 3.5. Equations used to calculate the values in Table 3.5 are included in Appendix A.1.

The software output results included analysis of variance table, regression coefficients, residuals and confidence intervals for the estimated parameters. The approximate standard error (ASE), calculated as the standard deviation of each parameter used for error analysis is also shown. The ASE values were calculated at 95% confidence interval. The ratio of the estimated parameter divided by the asymptotic standard error (Param/ASE) represents the *t*-statistic, which was used to determine the significance of the estimated regression coefficients values.

Table 3.5. ANOVA Table for multiple regression analysis (MSR = mean sum of regression, MSE = mean sum of error)

Source of variable	Sum of squares	Degree of freedom	Mean square	F statistic
Regression	SSR	p	MSR	MSR/MSE
Error	SSE	(n-p-1)	MSE	
Total	SST	(n-1)		

CHAPTER 4 RESULTS AND DISCUSSION

The main objective of this study was to study the effect of submerged arc welding parameters on the microstructure of the weld joints of SA516 and A709 steels. The effect of heat input achieved by varying welding current and speed on the microstructure of weld metal and the heat affected zone was studied. The results of the experiments described in Chapter 3 are presented and discussed here.

4.1 Chemical Composition of Weld Metals of SA516 and A709 Steels

As discussed in Chapter 2, the final microstructure of steel welds and their properties are highly influenced by the weld metal chemistry. The average chemical composition of the weld metals (WMs) of SA516 and A709 steels (obtained using the optical emission spectroscopy and LECO combustion method) and their base metals are shown in Tables 4.1 and 4.2, respectively. As seen, since the flux and base metals used for welding were the same for all weld test samples, the average chemical compositions of the WMs of the two steels were not expected to change appreciably. This is because only the welding current and speed were varied. The flux and other welding consumables were the same for all the weld samples. However, some noticeable changes in composition were observed for some elements. The changes in the weld metal elemental compositions were due to the dilution effect of the base metals by the filler electrode.

Table 4.1. Chemical compositions of SA516 steel weld metals.

PV Plate	H kJ/mm	C wt.%	Mn wt.%	Si wt.%	Al wt.%	S wt.%	Cr wt.%	Mo wt.%	Ni wt.%	Ti wt.%	O ppm	N ppm
PV0*		0.220	1.140	0.240	0.054	0.008	0.010	0.002	0.010	0.004	200	83
PV1	4.39	0.186	1.320	0.258	0.028	0.004	0.019	0.002	0.010	0.002	370	85
PV2	2.50	0.176	1.270	0.020	0.001	0.005	0.020	0.003	0.010	0.002	270	85
PV3	1.89	0.181	1.275	0.010	0.001	0.005	0.021	0.003	0.010	0.002	260	70
PV4	1.52	0.179	1.290	0.010	0.001	0.004	0.019	0.004	0.010	0.002	220	81
PV5	5.02	0.169	1.291	0.249	0.026	0.005	0.020	0.003	0.010	0.002	388	85
PV6	2.86	0.170	1.315	0.304	0.030	0.004	0.022	0.003	0.010	0.003	409	80
PV7	2.16	0.167	1.315	0.303	0.031	0.004	0.025	0.002	0.010	0.003	514	85
PV8	1.74	0.173	1.331	0.315	0.031	0.005	0.027	0.004	0.010	0.003	264	90
PV9	5.33	0.153	1.340	0.306	0.023	0.004	0.030	0.005	0.010	0.003	393	88
PV10	3.04	0.153	1.314	0.292	0.027	0.005	0.028	0.004	0.020	0.002	406	85
PV11	2.30	0.160	1.298	0.305	0.031	0.006	0.026	0.003	0.020	0.003	270	99
PV12	2.185	0.168	1.298	0.304	0.031	0.006	0.025	0.005	0.010	0.003	254	89

*PVO = SA516 base metal

The extent of dilution of the base metal depended on the amount of electrode material melted, which depended on the heat input. The WM elemental compositions that were mostly affected by varying heat input were those of carbon, aluminum, oxygen, nitrogen and silicon. Those of chromium, nickel, molybdenum, titanium, sulphur and manganese were minimal.

Table 4.2. Chemical compositions of A709 steel weld metals.

WT Plate	H kJ/mm	C wt.%	Mn wt.%	Si wt.%	Al wt.%	S wt.%	Cr wt.%	Ni wt.%	Mo wt.%	Ti wt.%	O ppm	N ppm
WT0*		0.040	1.300	0.060	0.030	0.007	0.090	0.140	0.040	0.001	350	87
WT1	4.39	0.037	1.361	0.134	0.018	0.006	0.080	0.120	0.034	0.007	460	99
WT2	2.50	0.033	1.368	0.134	0.017	0.007	0.080	0.150	0.040	0.009	150	90
WT3	1.89	0.028	1.374	0.133	0.016	0.007	0.080	0.120	0.035	0.008	108	90
WT4	1.52	0.024	1.381	0.132	0.016	0.007	0.080	0.140	0.038	0.008	189	87
WT5	5.02	0.019	1.388	0.132	0.015	0.007	0.080	0.130	0.034	0.007	423	99
WT6	2.86	0.015	1.394	0.131	0.014	0.007	0.090	0.170	0.045	0.011	277	107
WT7	2.16	0.010	1.401	0.131	0.013	0.007	0.080	0.150	0.040	0.009	388	124
WT8	1.74	0.006	1.407	0.130	0.012	0.007	0.070	0.110	0.032	0.007	89	94
WT9	5.33	0.001	1.414	0.130	0.012	0.007	0.070	0.110	0.030	0.005	447	95
WT10	3.04	0.003	1.421	0.129	0.011	0.007	0.080	0.130	0.035	0.008	445	97
WT11	2.30	0.008	1.427	0.129	0.011	0.008	0.070	0.120	0.033	0.008	505	96
WT12	1.85	0.012	1.434	0.128	0.009	0.008	0.090	0.160	0.044	0.012	245	109

*WT0 = A709 base metal

4.1.1 Carbon

From the results shown in Table 4.1, the carbon content of SA516 steel weld metals ranged from 0.153 to 0.186 wt.%. The carbon contents of the base metal of SA516 and the electrode are 0.22 wt.% and 0.01 wt.%, respectively (see Table 3.2). Since carbon is present in the base metal and the filler rod at different levels, any change in carbon content of the weld metal is ascribed to dilution caused by the electrode. As the welding current increased, electrode melting increased which, in turn, increased dilution but reduced the carbon content of the SA516 weld metals.

Figure 4.1 shows the variation of the weld metal carbon content with welding current for SA516 steel weld metal. With increasing current the carbon content in the weld metals of SA516 decreased. The reduction in carbon content will reduce the carbides formed in the welds. Yang [97] reported a reduction in hardness of the weld metal of SA516 as heat input increased. The decrease in hardness was attributed to the decrease in the cooling rate with increased heat input. Low cooling rate will decrease the fraction of hard phases, such as martensite and bainite, formed in the weld metals. However, due to the low carbon equivalent of SA516 steel (*CE* = 0.41) and probably dilution effect, martensite was not formed in the weld metal, the micrographic evidence of which will be shown later. The reduction in hardness may also be due to other factors, such as grain coarsening and reduced solid solution hardening caused by dilution which reduced the weld metal carbon content as heat input increased.

The carbon content of the weld metal of A709 steel ranged from 0.001 to 0.037 wt.% (see Table 4.2). The carbon content of A709 base metal is 0.04 wt.%. The same type of electrode was used in welding both SA516 and A709 steels. Figure 4.2 shows the variation of the weld metal carbon content with welding current for A709 steel weld metal. It can be seen that the carbon content of A709 weld metals decreased as the welding current increased. Yang [97] also recorded a reduction in hardness with increasing heat input for A709 steel weld metal probably due to the reduction in the weld metal carbon content. Due to low carbon equivalent (*CE* = 0.132) of A709 steel, and dilution effect martensite was not formed in its weld metals.

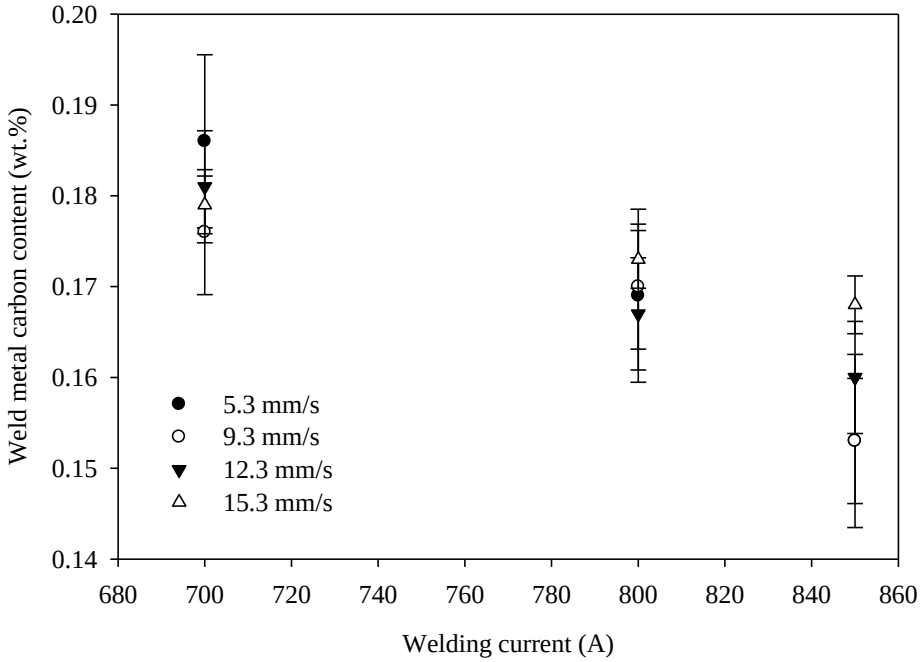

Figure 4.1. Relation between welding current and carbon content of SA516 steel weld metals.

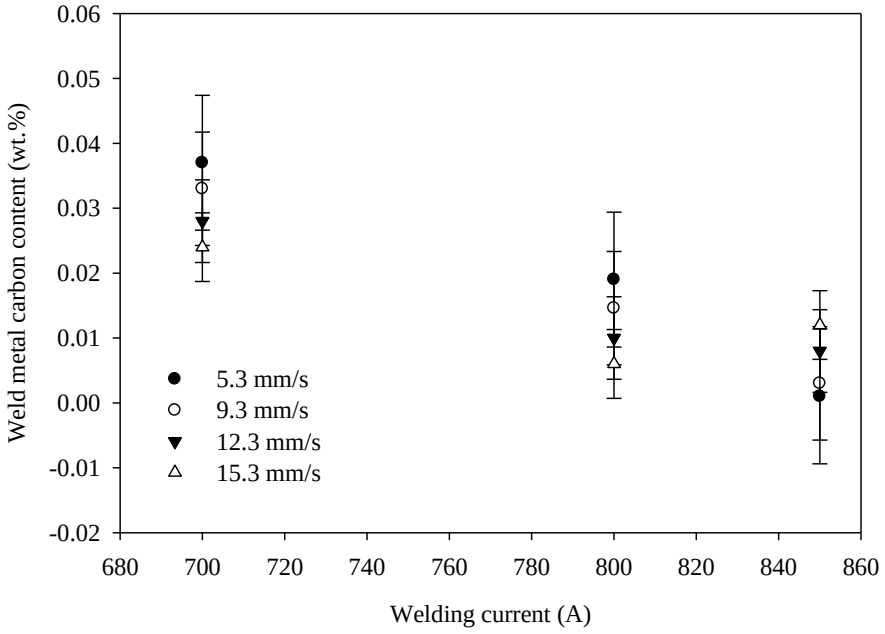

Figure 4.2. Relation between welding current and weld metal carbon content of A709 steel weld metals.

The reduction in hardness as the heat input increased occurred because of the reduction in solid solution hardening and/or due to grain coarsening effect caused by the reduction in cooling rate.

4.1.2 Aluminum

The source of aluminum in the weld metals of low carbon steels is mainly from the flux. As shown in Table 4.1, the aluminum content of SA516 base metal is 0.054 wt.%, but this was substantially reduced in the weld metals. It ranged from 0.001 wt.% to 0.031 wt.%. Since aluminum is a strong oxide and nitride former, it is possible the decrease in its content in the weld metals was due to its utilization in forming oxides and nitrides. For A709 welds, the aluminum contents of the weld metals were lower than that of the base metal (0.030 wt.%) as shown in Table 4.2; they. ranged from 0.009 wt.% to 0.018 wt%. The decrease of Al content in the WMs was ascribed to Al being used to form inclusions.

4.1.3 Silicon

The silicon content of the base metal of SA516 steel was 0.240 wt.% (see Table 4.1). This value increased to 0.306 wt.% for PV9 (850A, 9.3 mm/s). The lowest silicon content value was 0.010 wt.% for PV4 (700A, 15.3 mm/s). The source of additional silicon into the weld metal was from the flux. Any increase in flux melting would increase the WM silicon content. For A709 steel welds, there was generally a silicon pick-up in all cases. The A709 base metal silicon content was 0.06 wt.%. The highest silicon content was 0.134 wt.% for WT1 (700A, 5.3 mm/s). The lowest silicon level of 0.125 wt.% was obtained for WT12 (850A, 15.3 mm/s). Since the source of the silicon

pick-up was from the flux, it meant that increased heat input resulted in increased flux consumption which increased the silicon content of the weld metal.

4.1.4 Nitrogen

Nitrogen concentrations in the base metals of SA516 and A709 were 83 ppm and 87 ppm, respectively (see Tables 4.1 and 4.2). Small amounts of nitrogen pick-up were observed for both welds. Nitrogen concentration in the weld metals of SA516 steel ranged from 70 to 99 ppm. For A709 steel welds, it ranged from 87 to 99 ppm. The nitrogen concentration in both welds in general increased with increasing heat input.

4.1.5 Oxygen

A close look at Tables 4.1 and 4.2 shows that unlike nitrogen, the oxygen content changed appreciably with heat input in both SA516 and A709 weld metals. The oxygen concentrations in the base metals of SA516 and A709 steels were 200 ppm and 350 ppm, respectively, while they ranged from 220 to 514 ppm and 89 to 505 ppm in the weld metals of SA516 and A709, respectively. The flux is the main source of oxygen pick-up in the weld metals. In the weld metals of SA516, the highest oxygen concentration was 514 ppm for PV7 (800 A, 12.3 mm/s) while the lowest was 220 ppm for PV4 (700 A, 15.3 mm/s). For A709 steel welds, the highest oxygen level was 505 ppm for WT11 (850 A, 15.3 mm/s) while the lowest was 89 ppm for WT8 (800 A, 15.3 mm/s). The oxygen content of the weld metal has an influence on the inclusions which provide nucleation sites for the formation of ferrites [10, 14, 17, 36, 39].

At low oxygen level (less than 220 ppm), it was found that the number of inclusions formed in the weld metal does not provide adequate nucleation sites for ferrite nucleation and austenite is able to transform to bainite and martensite [37].

The variation of WM oxygen concentration with welding current is shown in Figures 4.3 and 4.4 for SA516 and A709 steels welds, respectively. Figure 4.3 indicates that, in general, the WM oxygen increased with welding current at fixed welding speeds of 5.3, 9.3 and 15.3 mm/s for SA516 steel. However, at 12.3 mm/s welding speed, WM oxygen increased substantially from 260 to 514 ppm when welding current increased from 700 to 800 A and thereafter decreased to 270 ppm with further increase of welding to 850 A for SA516 steel. Similarly, Figure 4.4 shows that the WM oxygen level increased with increasing welding current for welding speeds fixed at 9.3 and 12.3 mm/s for A709 steel. However, a mixed trend was observed for WM oxygen variation for welding speeds fixed at 5.3 and 15.3 mm/s, where WM oxygen initially decreased as welding current increased to 800 A and then increased with further increase of welding current to 850 A. In principle, WM oxygen content was expected to increase with increasing welding current. This is because increasing weld current also increases flux consumption.

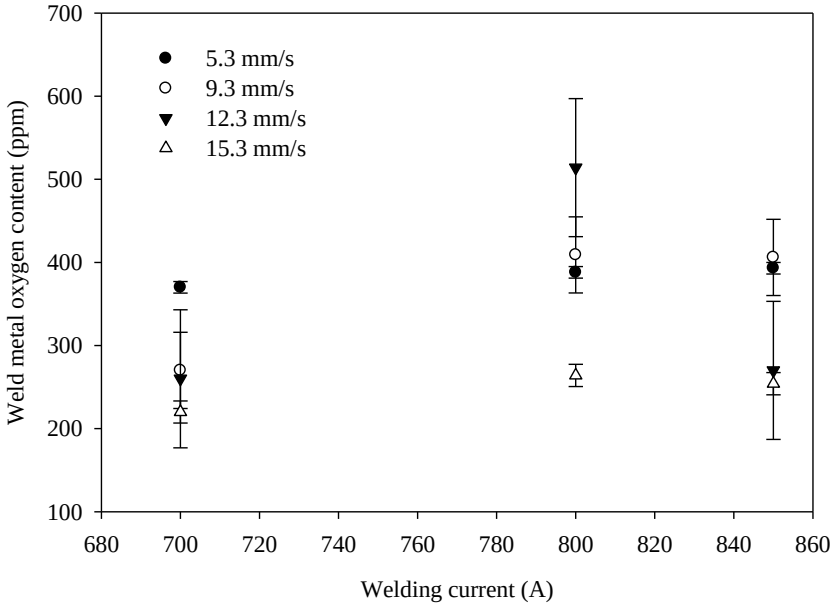

Figure 4.3. Variation of WM oxygen content with welding current for SA516 steel welds.

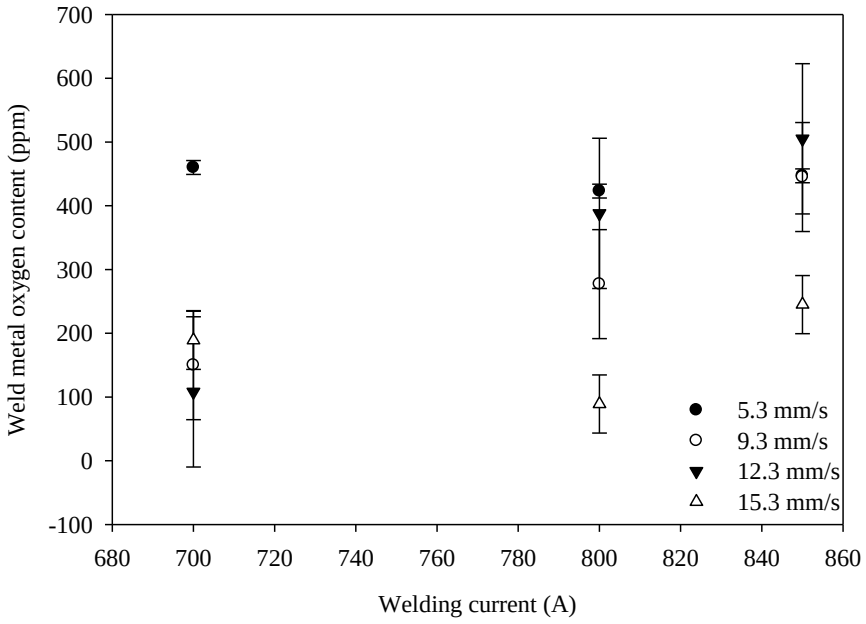

Figure 4.4. Variation of WM oxygen content with welding current for A709 steel welds.

Figures 4.5 and 4.6 show the variation of WM oxygen content with welding speed for SA516 and A709 steel welds, respectively. Figure 4.5 shows that the WM oxygen level for a given welding current generally decreased with increasing welding speed except for welding current of 800 A for SA516 steel. For SA516 steel, WM oxygen maximum value was realized at 12.3 mm/s (514 ppm) and thereafter reduced to 264 ppm. Figure 4.6 shows also a mixed trend observed for the WM oxygen content of A709 steel. The WM oxygen content decreased with increasing welding speed at a fixed welding current of 700 A. For other high welding currents (800 and 850 A), the WM oxygen content initially decreased when welding speed increased from 5.3 to 9.3 mm/s. As welding speed increased to 12.3 mm/s, there was a noticeable increase in the WM oxygen content. However, with further increase in welding speed, WM oxygen content reduced. With increasing welding speed, it was expected the WM oxygen content would decrease due to decreased heat input.

Figures 4.7 and 4.8 show the relationship between WM oxygen content and heat input for SA516 and A709 steel welds, respectively. The WM oxygen content showed a general increase with increasing heat input in for both metals. However, for 800 A welding current, WM oxygen content increased substantially from 264 to 514 ppm as heat input increased form 1.74 to 2.16 kJ/mm and thereafter decreased to 388 ppm at 5.02 kJ/mm for SA516 steel. For A709 steel a trend was not established for the variation of WM oxygen content with heat input. The increase in heat input was expected to increase flux consumption. Since the main source of WM oxygen is from the flux, any increase in its consumption will increase the oxygen level in the weld metal.

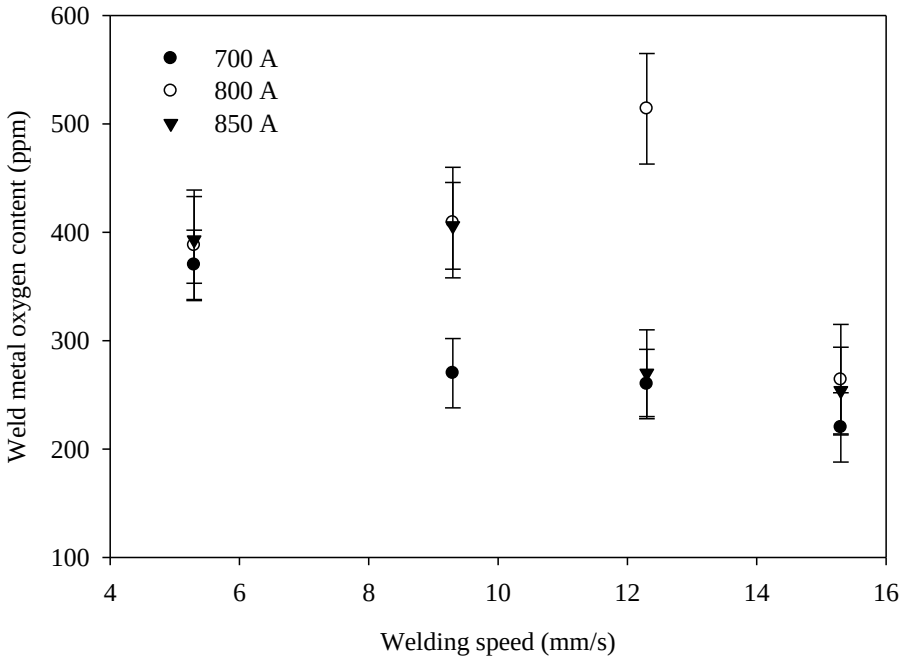

Figure 4.5. Variation of WM oxygen content with welding speed for SA516 steel welds.

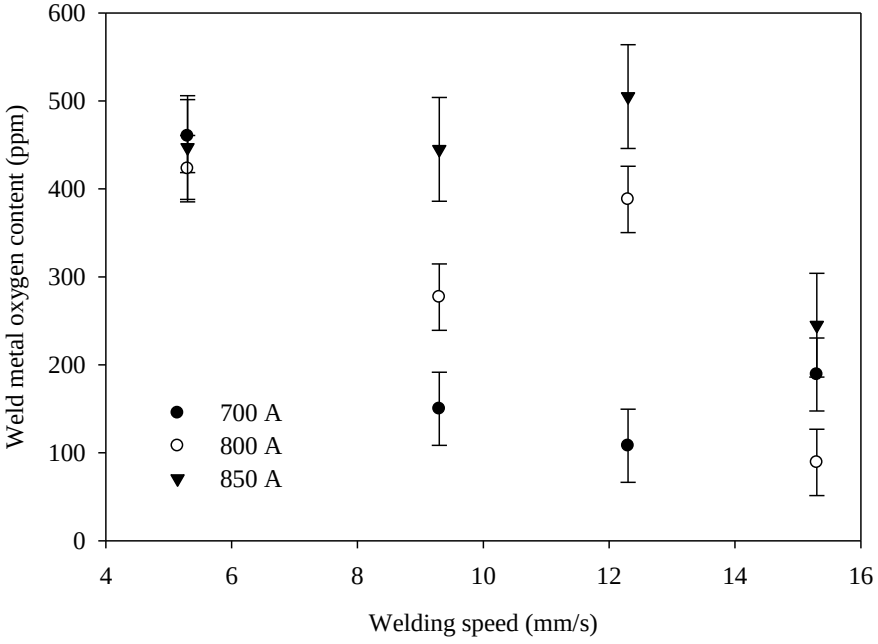

Figure 4.6. Variation of WM oxygen content with welding speed for A709 steel welds.

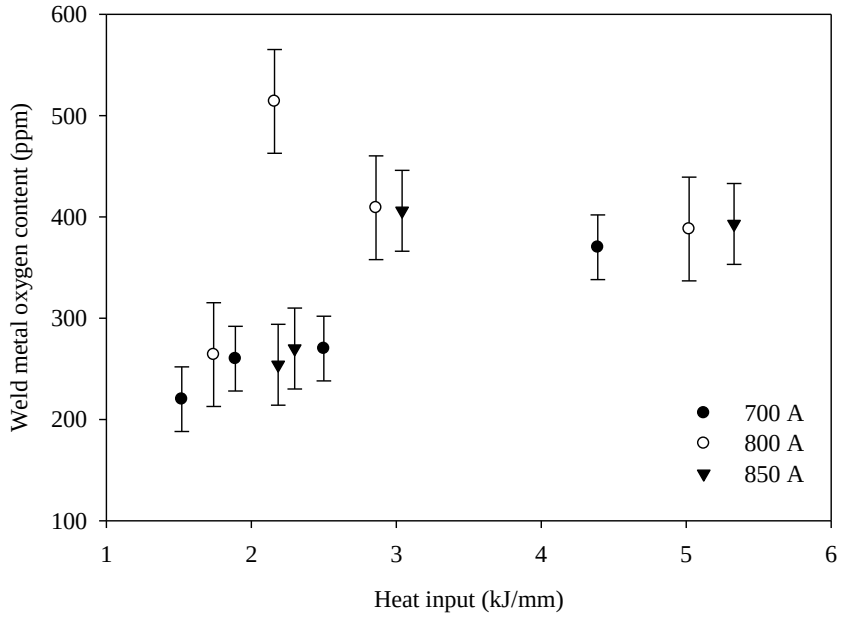

Figure 4.7. Variation of WM oxygen content with welding heat input for SA516 steel welds.

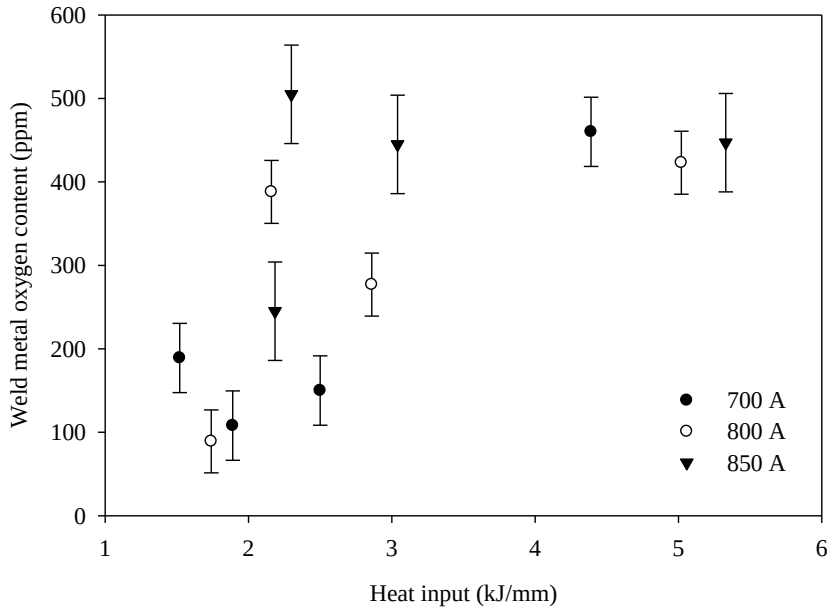

Figure 4.8. Variation of WM oxygen content with welding heat input for A709 steel welds.

The results in general showed that increasing heat input achieved either by increasing welding current or by reducing welding speed increased the WM oxygen content for both steels. Since the dilution effect and flux consumption obtained with increasing welding current are more than that obtained with increasing welding speed, the increase in the weld metal oxygen was not expected to be the same for both conditions.

4.2 Weld Nugget Geometry, Cooling Rate Parameter and Calculated Cooling Rate

The results of weld nugget geometry measurements are tabulated in Table 4.3. The table shows that high heat input produced large bead nugget area. Increased heat input is associated with increased electrode melting and increased volume of the molten pool. The nugget area of the weld bead is a good indicator of the weld mechanical properties [13, 48] because the diffusion distance for hydrogen, which causes weld metal embrittlement, increases with the nugget area.

Figure 4.9 shows typical optical macrographs illustrating the weld profiles obtained for SA516 using different welding currents, but with a fixed welding speed of 9.3 mm/s. It can be seen that the nugget width (w) is larger, but with less weld reinforcement (h), at lower welding currents. As welding current increased from 700 to 850 A (i.e., heat input also increased from 2.50 to 3.04 kJ/mm), weld nugget width decreased while the weld penetration (p) and reinforcement (h) increased. This is understandable because, as welding current increased, more filler material was added per unit length of weld and the weld pool depth was increased. Thus, the molten pool was deeper and the added filler metal solidified on top of the joint surface as weld reinforcement.

Table 4.3. Bead morphology and cooling rate parameters for SA516 and A709 weld metals.

Weld #	H kJ/mm	$\Delta t_{8/5}$ s	CR* °C/s	NA* mm^2 SA516	CI* mm SA516	NA/CI mm SA516	NA mm^2 A709	CI mm A709	NA/CI mm A709
1	4.39	21.96	13.66	199.0	36.0	5.5	173.0	33.0	5.2
2	2.50	12.51	23.98	109.5	27.0	4.1	107.0	24.0	4.5
3	1.89	9.46	31.71	83.0	23.5	3.5	99.0	23.0	4.3
4	1.52	7.61	39.42	68.5	20.5	3.3	72.0	23.0	3.1
5	5.02	25.09	11.96	226.0	36.0	6.3	234.0	38.0	6.2
6	2.86	14.30	20.98	141.0	30.0	4.7	159.0	29.0	5.5
7	2.16	10.81	27.75	108.0	23.0	4.7	106.0	24.0	4.4
8	1.74	8.69	34.52	82.0	21.0	3.9	90.0	22.0	4.1
9	5.33	26.66	11.25	209.0	40.0	5.2	258.0	38.0	6.8
10	3.04	15.19	19.75	151.0	29.0	5.2	128.0	24.0	5.3
11	2.30	11.49	26.11	134.0	22.0	6.1	110.0	23.0	4.8
12	1.85	9.24	32.47	98.0	21.0	4.7	88.0	21.0	4.2

* CR = Cooling Rate *NA = Nugget Area; CI = Cooling Interface length.

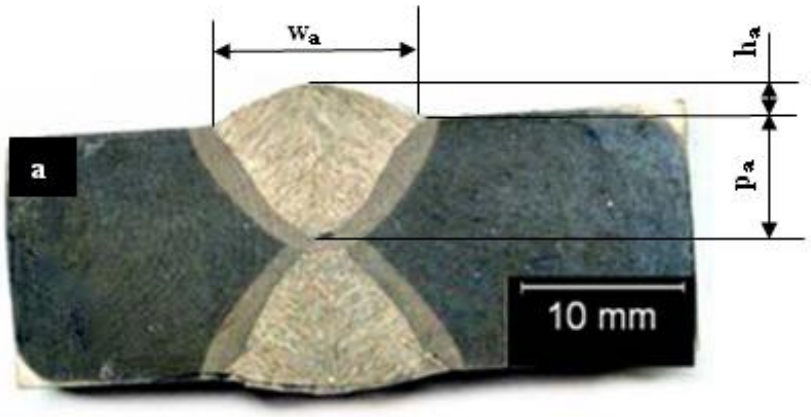

Figure 4.9. Weld profiles for SA516 steel welded using a welding speed of 9.3 mm/s and: (a) 700 A, (b) 800 A, and (c) 850 A. (w = weld bead width, h = reinforcement, p = penetration).

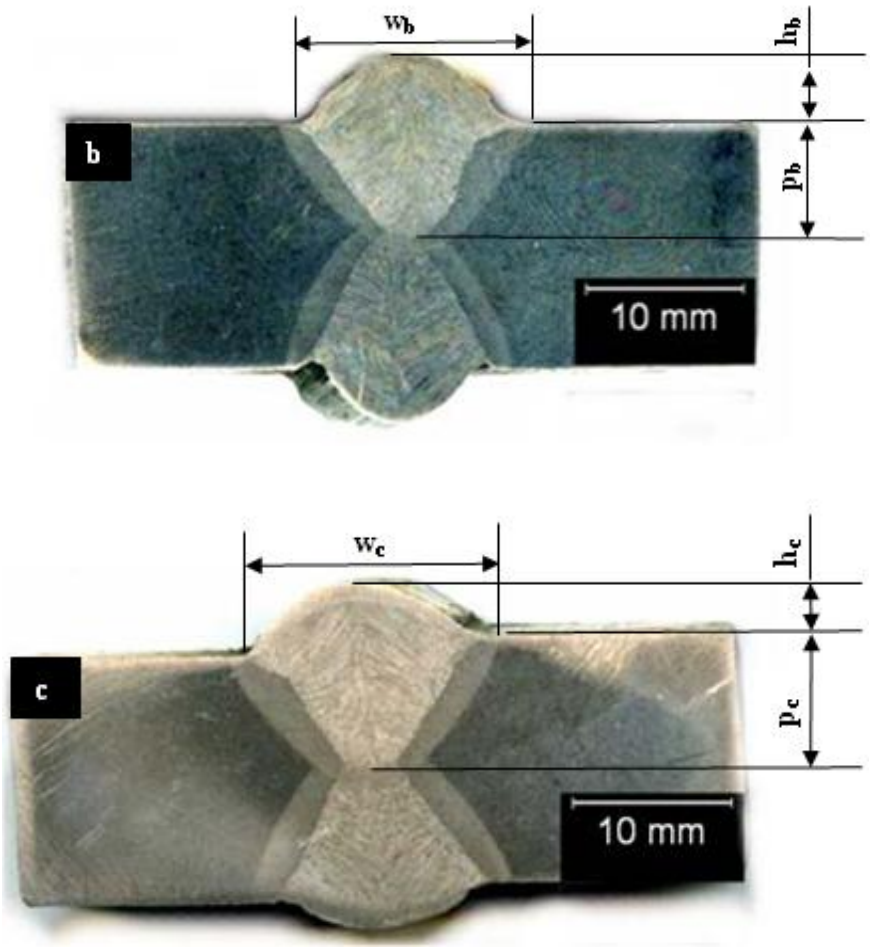

Figure 4.9 continued.

Figures 4.10 and 4.11 show the variation of weld nugget area (NA) with welding current for SA516 and A709 steel weld metals, respectively. An increase in nugget area was recorded also for the A709 weld metal at 9.3 mm/s welding speed where NA increased from 107 to 159 and then to 128 mm^2. Basu and Raman [13] reported a sharp increase in NA when the welding current was increased from 425 to 625 A at a fixed welding speed range of 3 to 13 mm/s. They observed that with further increase of welding current from 625 to 800 A, the change in NA was very gradual.

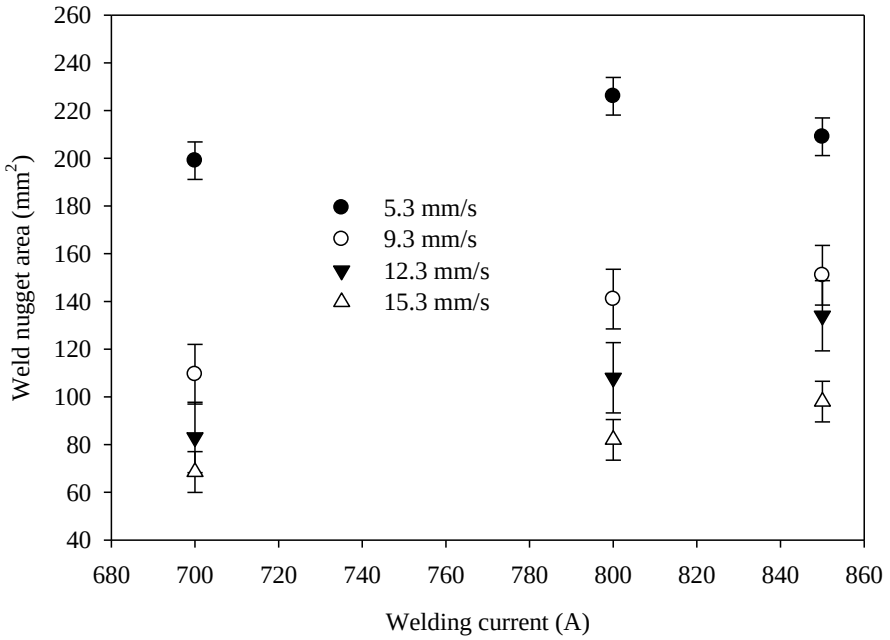

Figure 4.10. Variation of weld nugget area with welding current for SA516 steel welds.

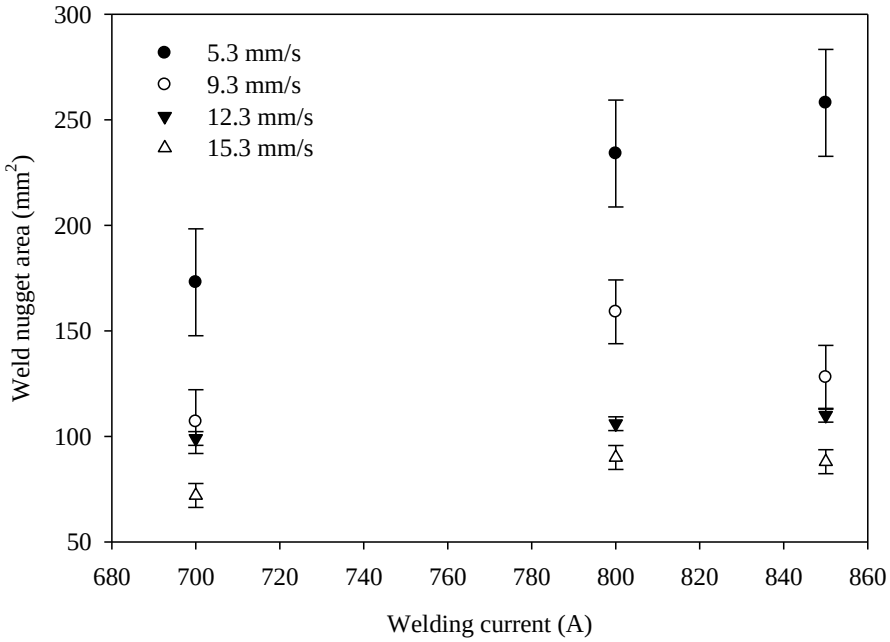

Figure 4.11. Variation of weld nugget area with welding current for A709 steel welds.

Although the welding current range used in this study is different from that used in [13], the results obtained are consistent with their findings. The variation of the cooling rate parameter with heat input is shown in Figures 4.12 and 4.13 for SA516 and A709 welds, respectively. For both welds, the cooling rate parameter (NA/CI) increased with increasing heat input. As increasing heat input corresponds to low cooling rate, it means increased cooling rate parameter corresponds to reduced cooling rate. As a result, high value of the NA/CI ratio, which is associated with high heat input, will produce low cooling rate [13]. A high value of the NA/CI ratio also translates to an increased time constant ($\Delta t_{8/5}$), therefore, the weld dwelt longer time at higher temperatures above the $Ac_{3,}$ the temperature for the austenite-to-ferrite transformation. The increase in time spent at high temperatures enabled the formation of grain boundary and Widmanstatten ferrites. The cooling rate calculated using Equation 2.6 (i.e., CR = $300/\Delta t_{8/5}$) and the cooling rate parameter ratio NA/CI are tabulated in Table 4.3. The table also shows the cooling rate constant, the time taken for the weld metal to cool from 800 to 500ºC ($\Delta t_{8/5}$), which increased with increasing heat input.

4.3 BM Microstructure of SA516 and A709 Steels

Figures 4.14 and 4.15 are optical micrographs showing the microstructures of ASME SA516 Grade 70 and ASTM A709 Grade 50 steel base metals, respectively. The microstructure of the SA516 base metal consists primarily of equiaxed ferrite grains (light etched), F, and pearlite colonies (dark etched), P, aligned with the rolling direction.

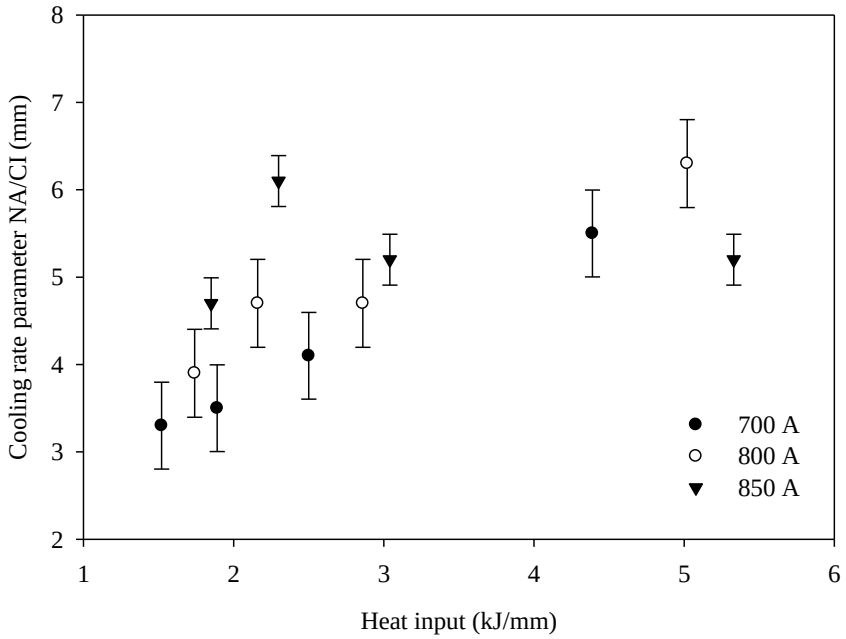

Figure 412. Relationship between heat input and cooling rate parameter for SA516 steel welds.

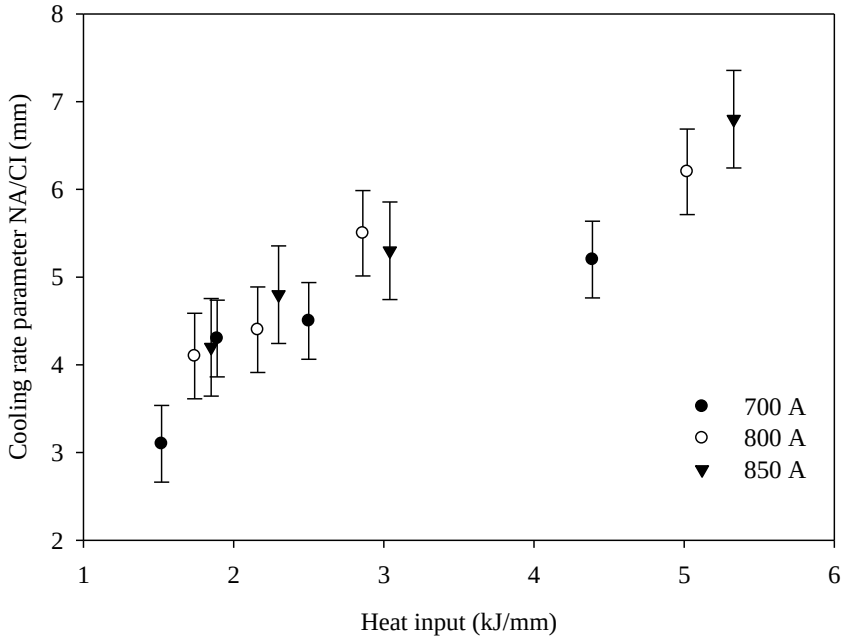

Figure 4.13. Relationship between heat input and cooling rate parameter for A709 steel welds.

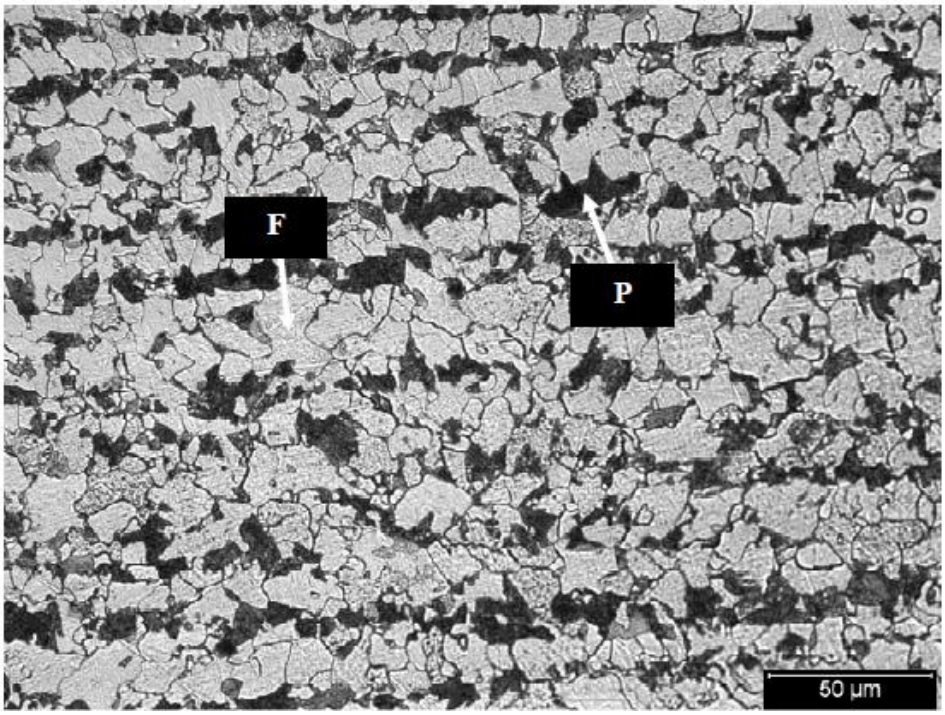

Figure 4.14. Optical micrograph of as-received ASME SA516 Grade 70 steel. F = ferrite, P = pearlite.

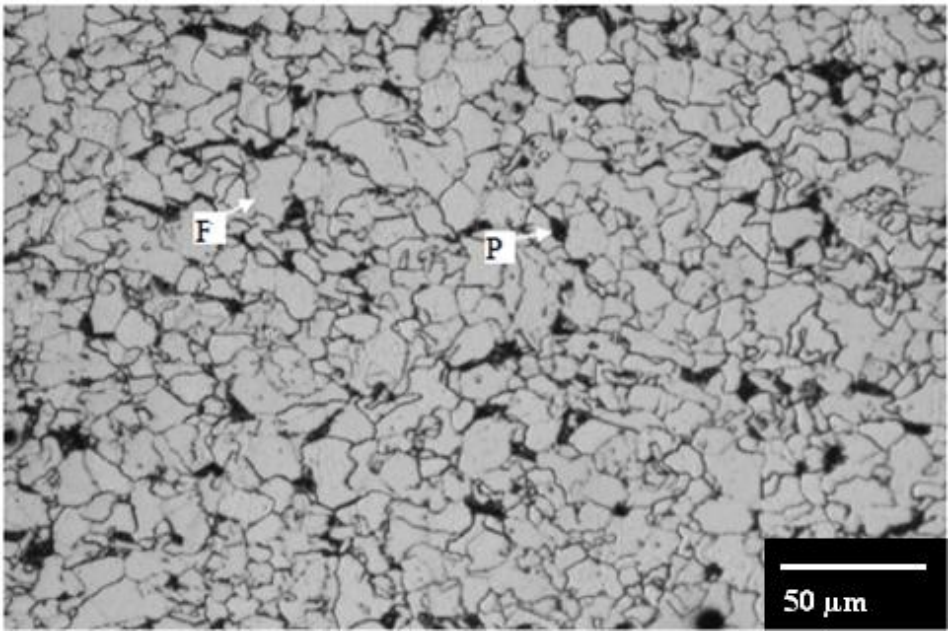

Figure 4.15. Optical micrograph of as-received ASTM A709 Grade 50 steel. F = ferrite, P = pearlite.

Quantitative analysis of the proportions of SA516 steel base metal microconstituents using PAX-it image analysis software showed that ferrite constituted approximately 70%, while pearlite constituted approximately 30%. The proportions of ferrite and pearlite in SA516 base metal calculated using the inverse lever rule were 73.5% and 26.5%, respectively. The average the ferrite grain size determined using PAX-it was ~ 32 µm, which corresponds to ASTM grain size number 7.

The microstructure of the A709 base metal consists primarily of equiaxed ferrite grains (light etched), F, and pearlite colonies (dark etched), P, aligned with the rolling direction. Image analysis of the microconstituents showed that the ferrite constituted approximately 94%, while pearlite constituted approximately 6%. The ferrite and pearlite microconstituents in A709 parent metal calculated using the lever rule are 96.5% and 4.5%, respectively. The average ferrite grain size number determined using PAX-it is ~ 27 µm, which corresponds to ASTM grain size number 7.5. Details of the lever rule calculations and ASTM grain size number determination are shown in Appendix D.

4.4 HAZ of SA516 and A709 Steel Welds

4.4.1 Effect of Current and Speed on HAZ Size

A typical welded joint with clearly visible HAZ around the weld metal was shown in Figure 4.9. Figures 4.16 and 4.17 show respectively the effects of welding current and speed on the HAZ size (measured with the PAX-it image analysis software) for SA516 steel welds, while Figures 4.18 and 4.19 show similar results for A709 steel welds.

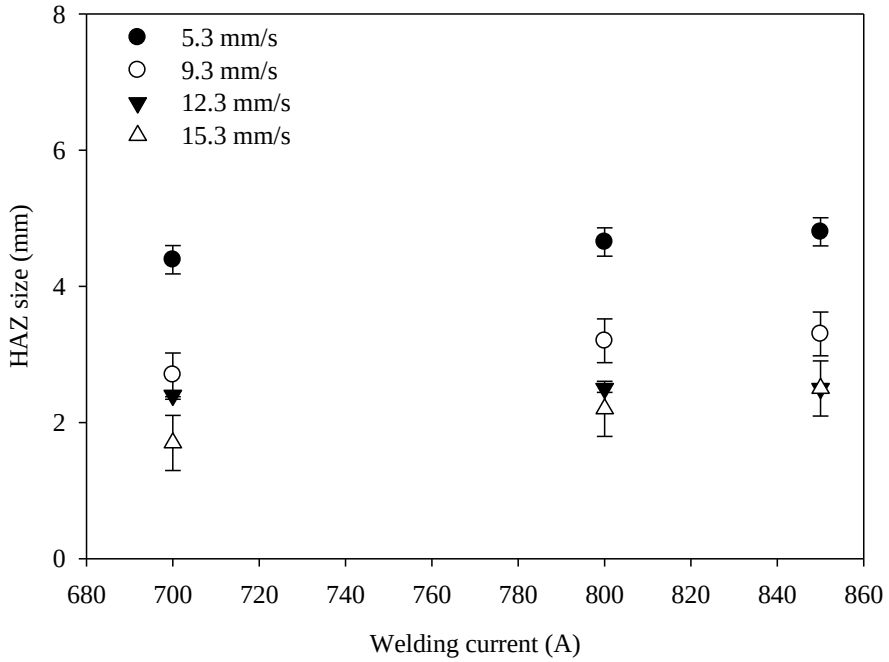

Figure 4.16. Effect of welding current on HAZ size for SA516 steel welds.

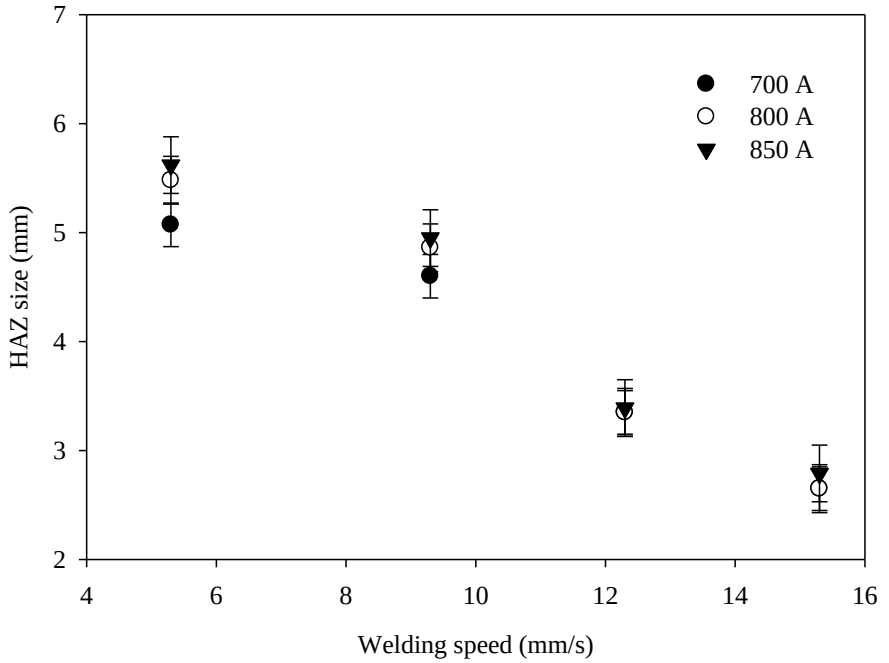

Figure 4.17. Effect of welding speed on HAZ size for SA516 steel welds.

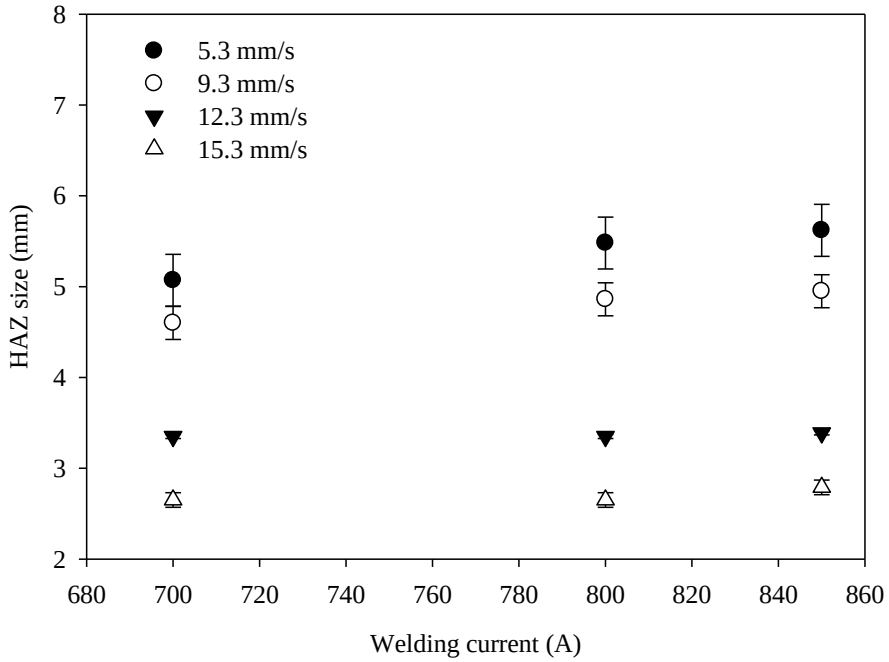

Figure 4.18. Effect of welding current on HAZ size for A709 steel welds

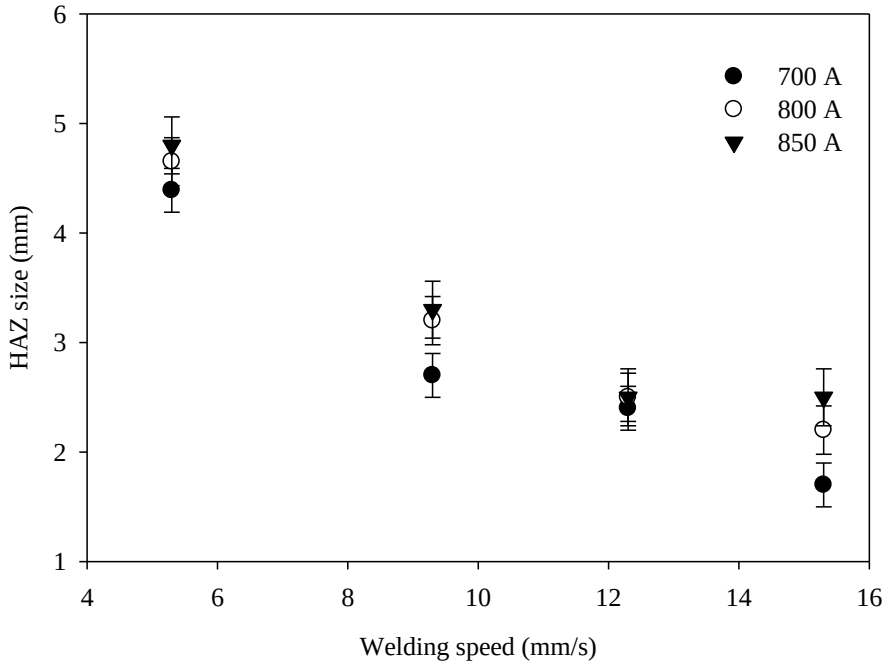

Figure 4.19. Effect of welding speed on HAZ size for A709 steel welds.

Examination of these figures show that the HAZ size in all cases decreased with increasing welding speed, but increased with increasing welding current.

When heat input is increased by increasing welding current, for a given welding speed, electrode melting increases and so does the volume of the molten pool. This increases the amount of heat that must be conducted through the surrounding base metal sink and, subsequently, results in an increase in the HAZ size. Increase in welding current for a given welding speed was reported to increase penetration depth, bead size and weld width due to the increased electrode melting [98]. On the other hand, for a given welding current, if the heat input is increased by reducing the welding speed, plate melting increases. It was reported that plate melting is related to weld penetration depth and HAZ size, while electrode melting controls the weld bead shape [98].

Since increasing welding current also increases electrode consumption, the pool of molten metal in the welded joint is enlarged which increases heat flow into the base metal, thereby increasing HAZ size and penetration depth. Figures 4.16 and 4.18 show the increase in the HAZ size was gradual when welding current was increased. Figures 4.17 and 4.19 show a more drastic reduction in the HAZ size when the welding speed was increased. At a fixed current, increasing welding speed means that the electrode travels faster and the distance it covers per unit time increases. As a result, the heat input per unit length of weld bead decreases and so also the metal deposition rate.

4.4.2 Microstructures of HAZ of SA516 Steel Welds

A typical HAZ microstructure developed in SA516 steel weld is shown in Figure 4.20. The figure shows different prior austenite grains in the various regions of the HAZ and WM. The coarsening of the prior austenite grains, moving from the base metal on the far left toward the fusion line on the far right, can be observed.

The grain size in the coarse-grained heat affected zone (CGHAZ) ranged from ASTM grain size number 4 to 3.5 (i.e., 87μm to 110 μm) near the fusion line. At approximately 1.5 mm from the fusion line, where there is a high temperature gradient, the ASTM grain size ranged 7 to 5.5 (i.e., 30 μm to 56 μm). The microstructure of the CGHAZ of SA516 welds produced using different welding currents and a welding speed of 9.3 mm/s are shown in Figure 4.21. It consists primarily of grain boundary ferrite (GBF), Widmanstatten ferrite (WF), pearlite (P) and bainite (B). On the average, the prior austenite grain size within the HAZ increased from 87 μm to 127 μm as the welding current increased from 700 A to 850 A for a welding speed of 9.3 mm/s.

Figure 4.22 shows the micrographs of the CGHAZ for SA516 welds produced using different welding speeds and a fixed welding current of 800 A. As heat input decreased with increasing welding speed causing the cooling rate to increase, small prior austenite grains and fine ferrite laths were produced as welding speed increased. The prior austenite grain size number changed from ASTM grain size number 3 (i.e., 127 μm) for welding speed of 5.3 mm/s (high heat input) to ASTM grain size number 6 (i.e., 45 μm) for a welding speed of 15.3 mm/s (low heat input).

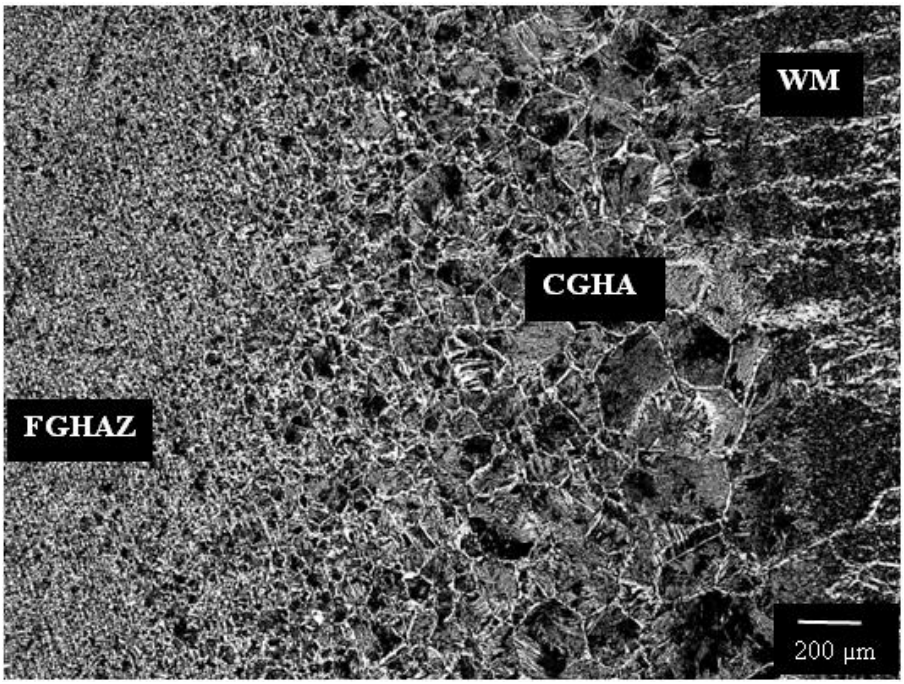

Figure 4.20.Typical microstructure of the FCHAZ, CGHAZ and WM for SA516 steel weld.

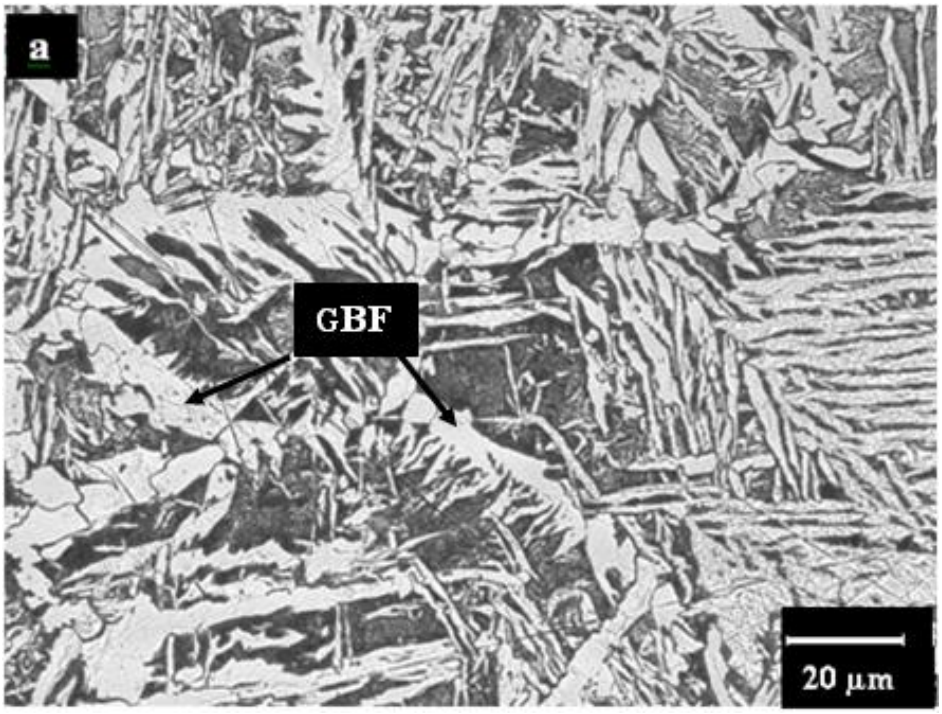

Figure 4.21. Microstructure of CGHAZ of SA516 steel weldment produced using (a) 700, (b) 800 A and (c) 850 A and a welding speed of 9.3 mm/s. B = bainite, GBF = grain boundary ferrite and WF = Widmanstatten ferrite.

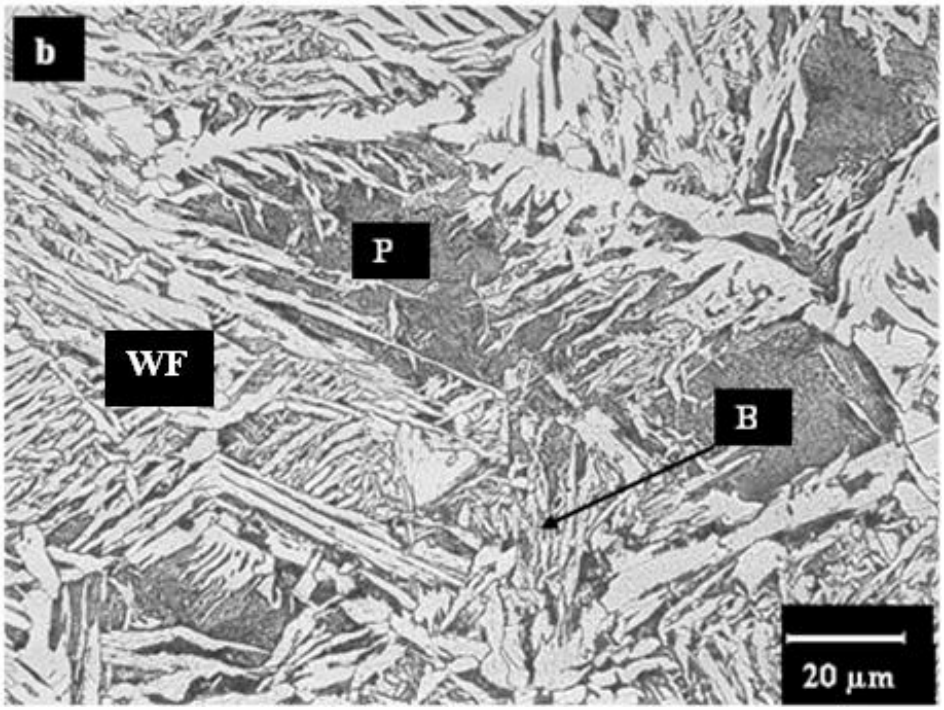

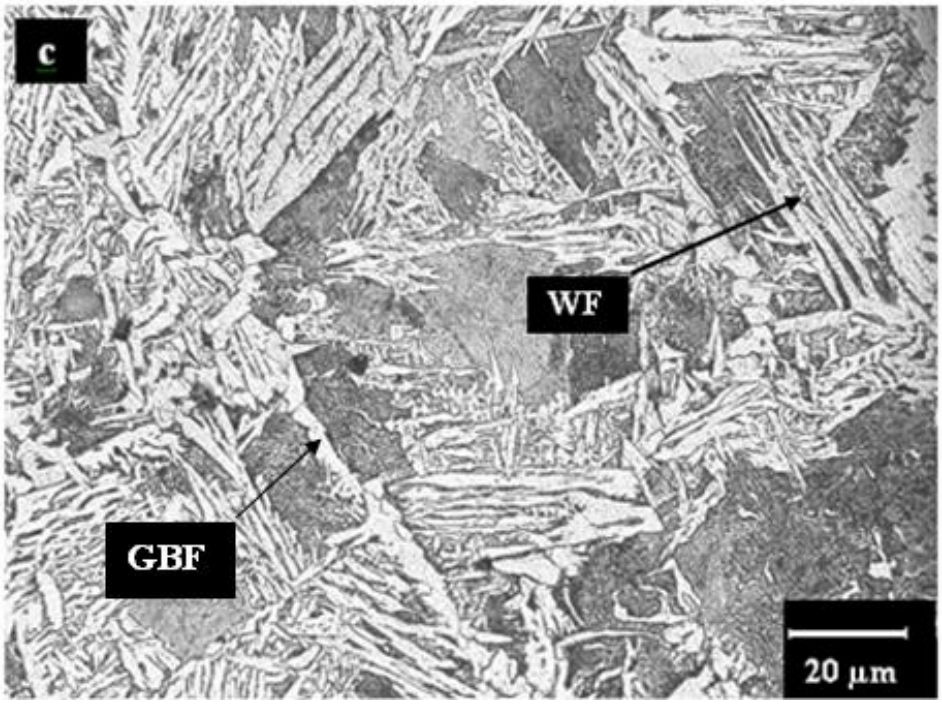

Figure 4.21 continued.

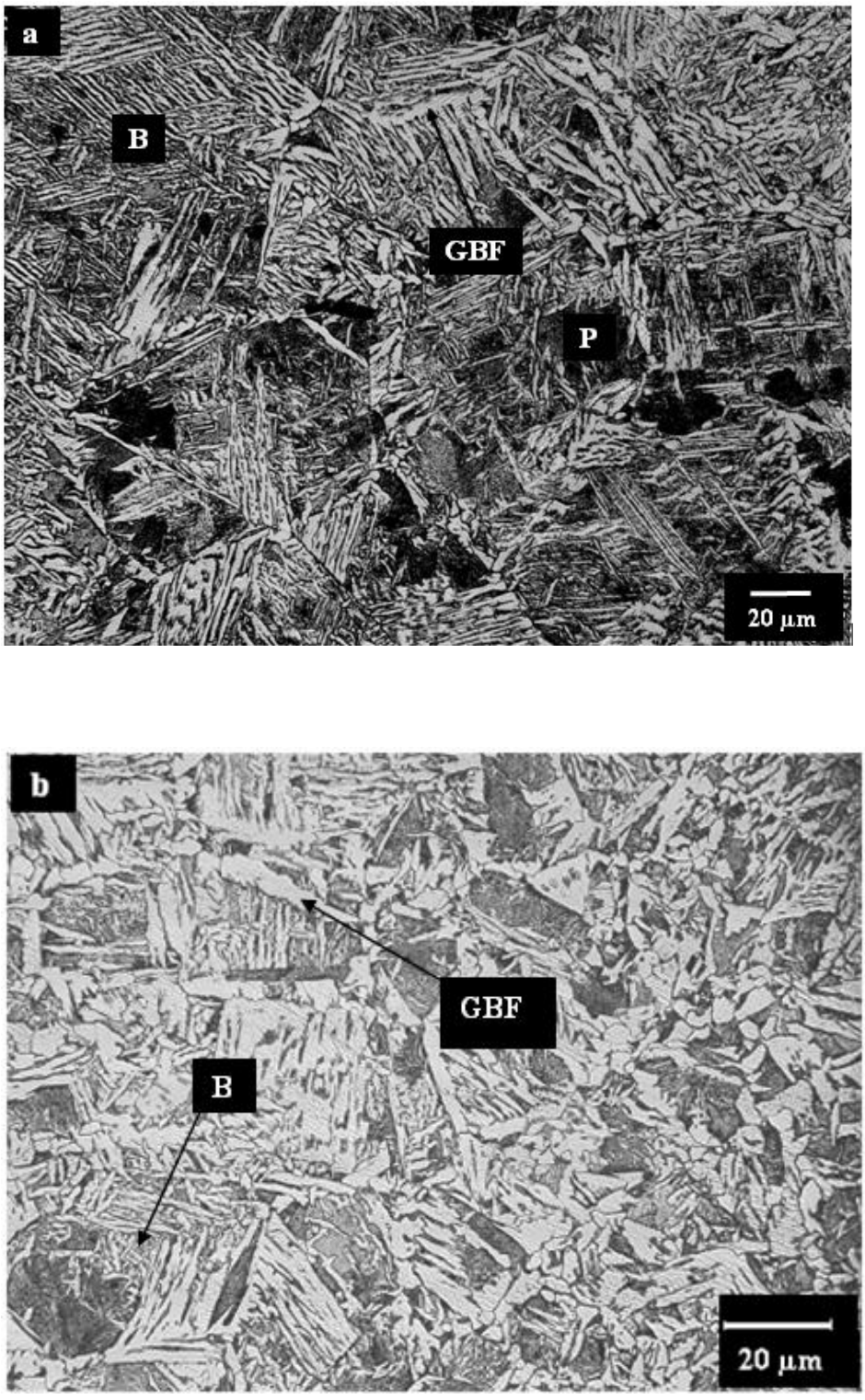

Figure 4.22. Microstructure of CGHAZ of SA516 steel weldment produced using a welding current of 800 A and different welding speeds of (a) 5.3 mm/s, (b) 9.3 mm/s, (c) 12.3 mm/s and (d) 15.3 mm/s. (B = bainite, GBF = grain boundary ferrite, P = pearlite WF = Widmanstatten ferrite).

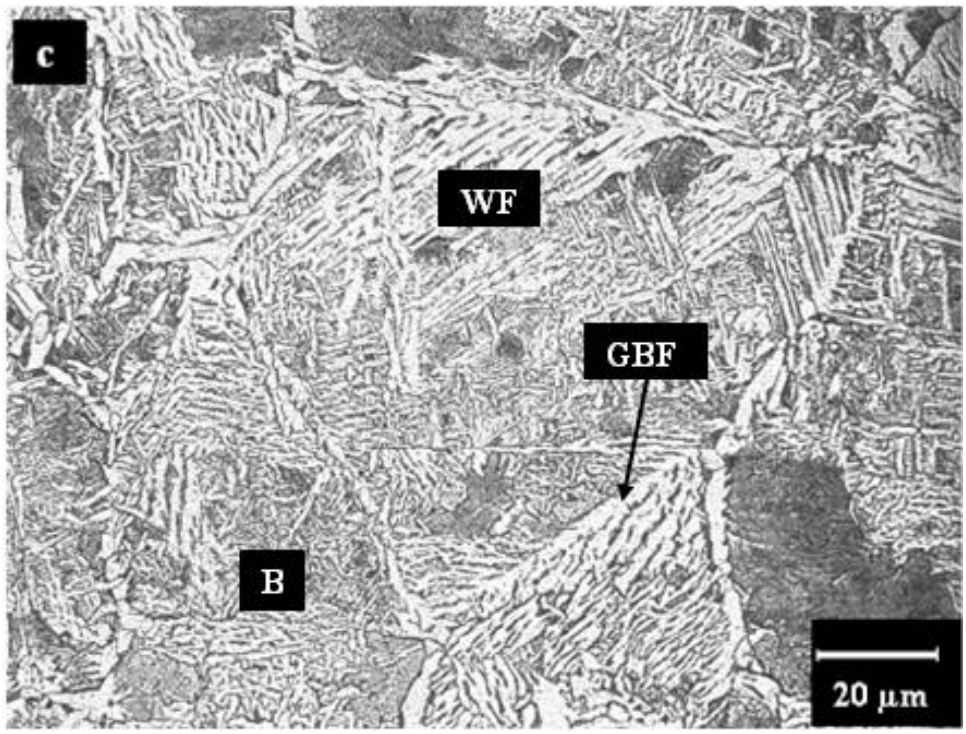

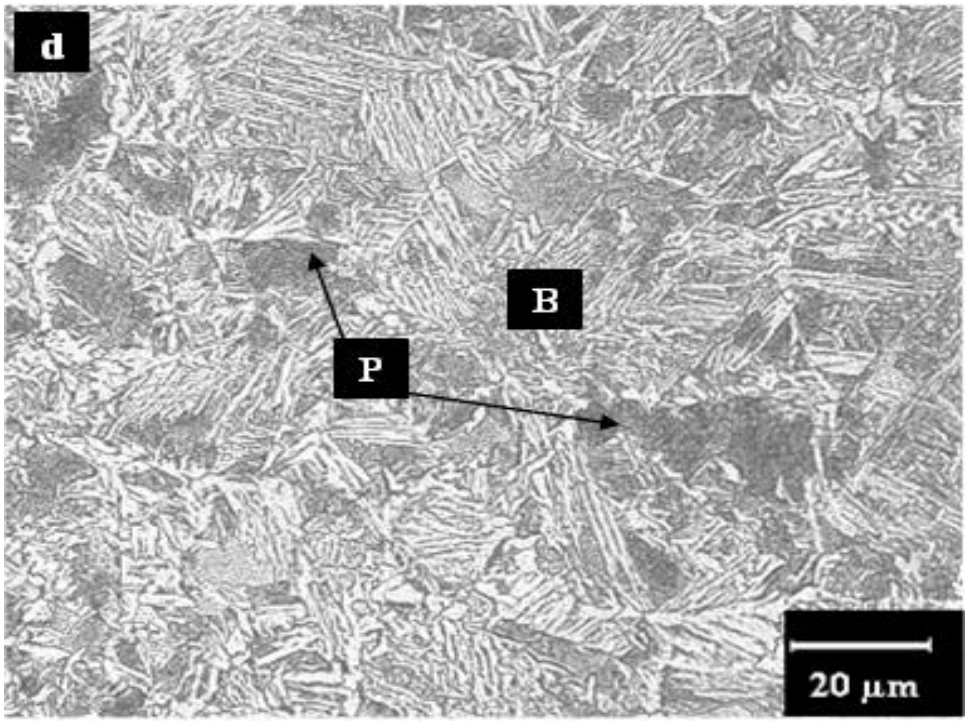

Figure 4.22 continued.

4.4.3 Microstructures of HAZ in A709 Steel Welds

The microstructures of the CGHAZ produced with a welding current of 850 A and different of welding speeds (5.3, 9.3, 12.3 and 15.3 mm/s) are shown in Figure 4.23 for A709 steel welds. The microstructure though not distinguished clearly, typically comprises primarily bainite (B) and ferrite (F) for all welding speeds.

4.4.4 Microstructures of SA516 and A709 Steel Weld Metals

The main microconstituents found in a typical weld metal of SA516 steel produced using 800 A and 9.3 mm/s are shown in Figure 4.24. They consisted of proeuctectoid grain boundary ferrite (GBF), Widmanstatten side plate ferrite (WF) and acicular ferrite (AF). Quantitative metallographic analysis of the micrographs obtained showed that the weld metal consisted of approximately 76% AF, 17% GBF and 7% WF. The main microconstituents found in a typical weld metal of A709 steel produced using 850 A and 15.3 mm/s are shown in Figure 4.25. They also consisted of GBF, WF and AF. Quantitative metallographic analysis of the micrographs obtained showed that the weld metal consisted approximately of 81% AF, 7.6% GBF and 11.4% WF.

In both weld metals of SA516 and A709 steels, GBF and WF formed on prior austenite grain boundaries, while the interior contained mostly AF. Additional micrographs of the HAZ and WM of the welds of both steels are provided in Appendix C.

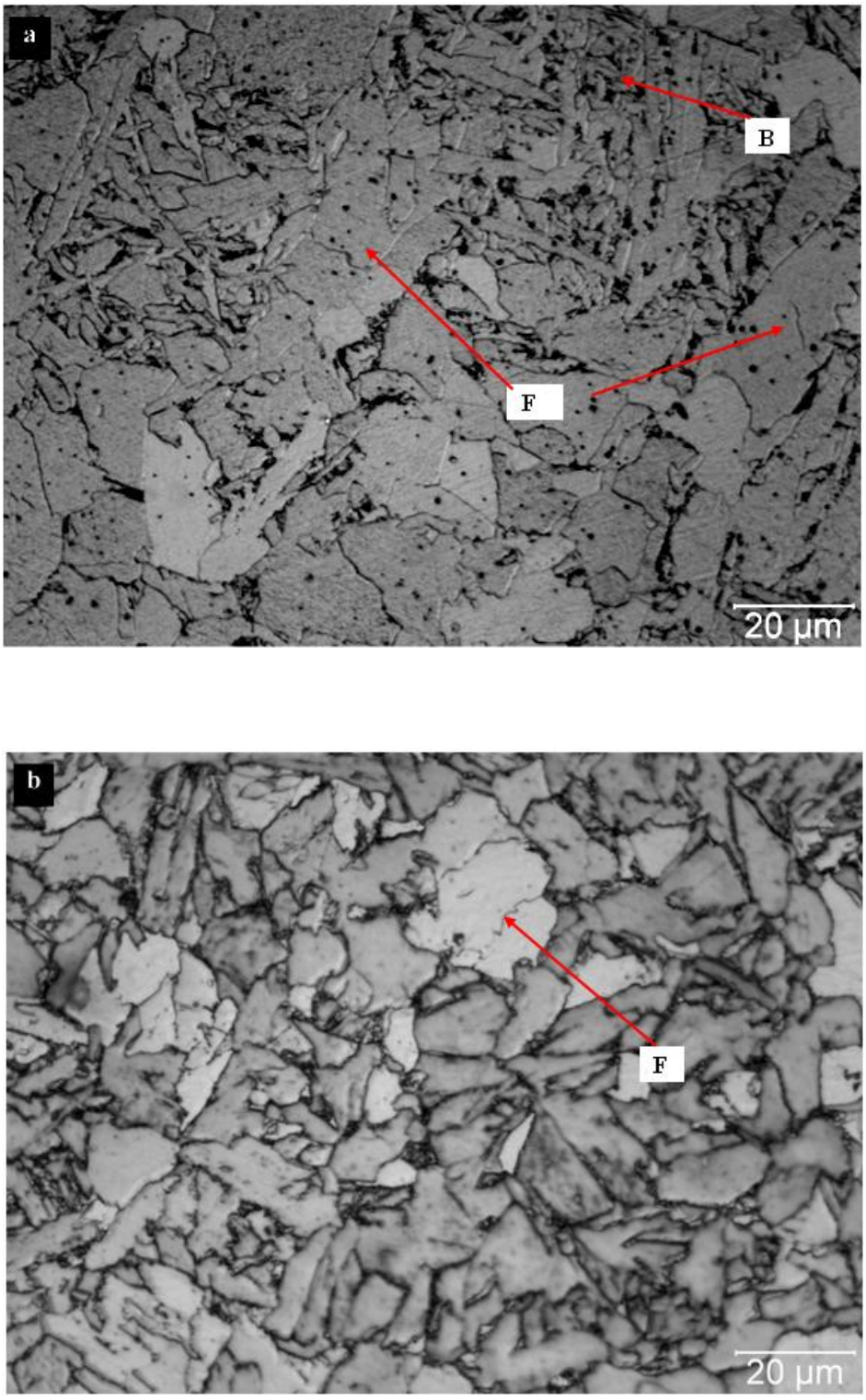

Figure 4.23. Microstructure of CGHAZ of A709 steel weldment produced using welding current of 850 A and different welding speeds (a) 5.3 mm/s, (b) 9.3 mm/s, (c) 12.3 mm/s and (d) 15.3 mm/s.

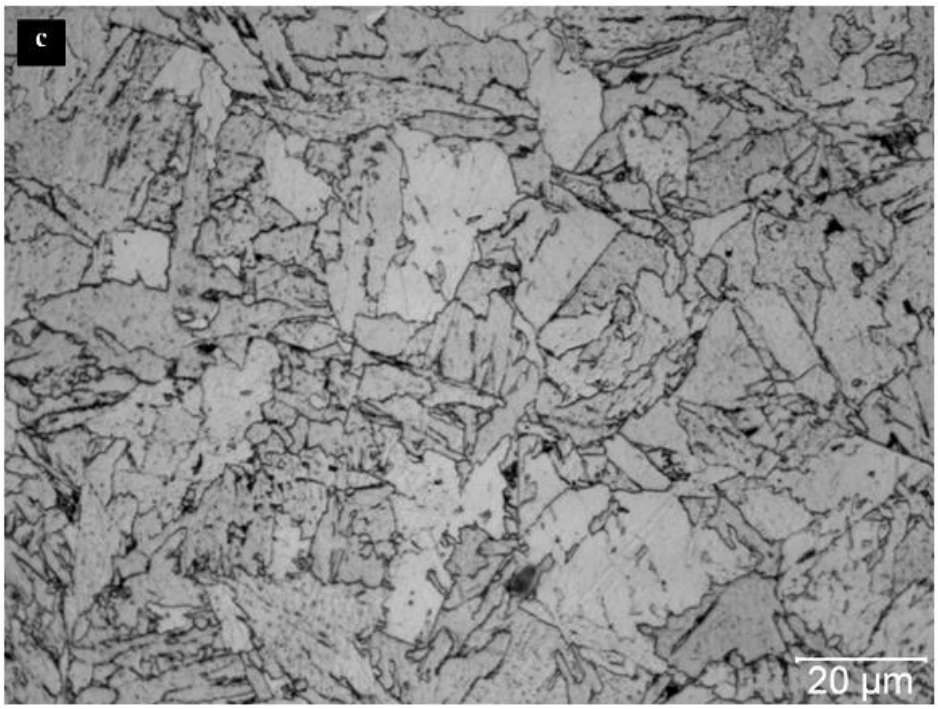

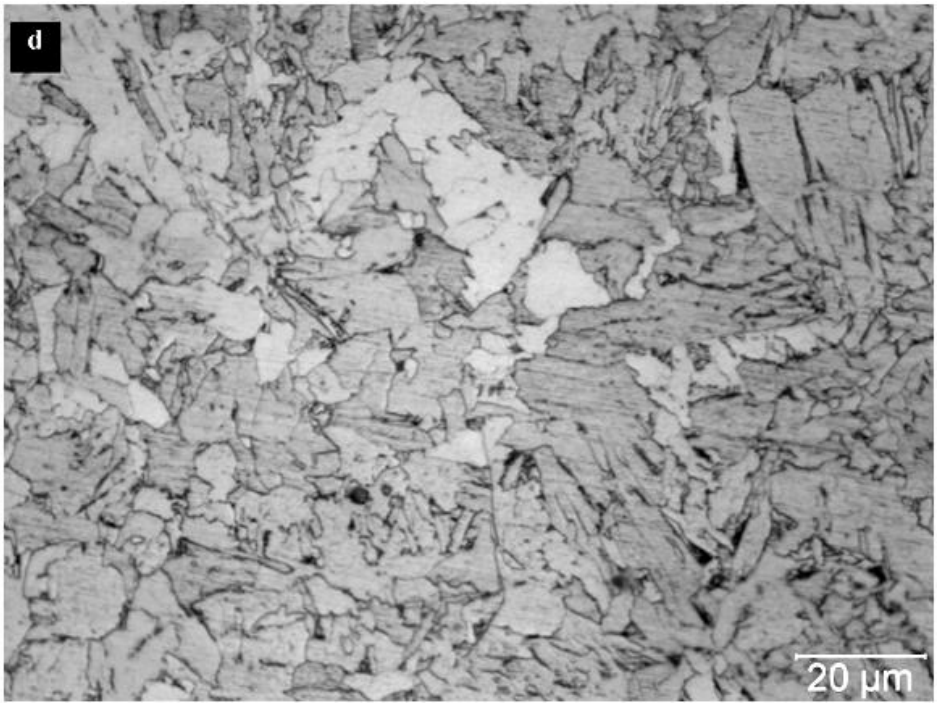

Figure 4.23 continued.

Figure 4.24. The main microconstituents in the weld metal of SA516 steel produced using 800 A and 9.3 mm/s.

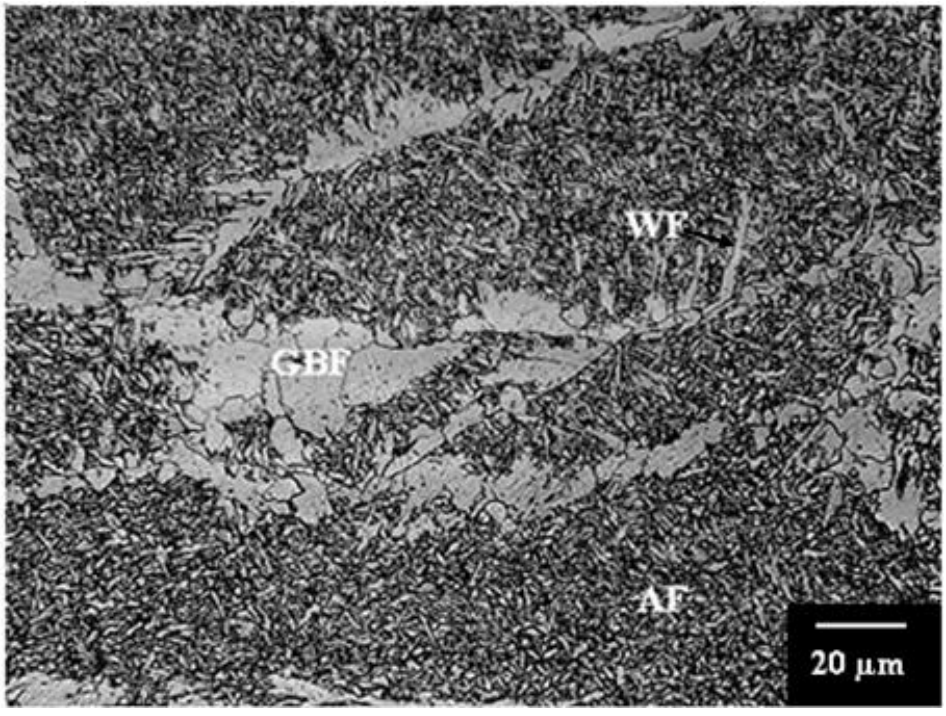

Figure 4.25. The main microconstituents in the weld metal of A709 steel produced using 850 A and 15.3 mm/s.

4.5 Effect of Welding Speed and Current on Prior Austenite Grain Width

4.5.1 Welding Speed

Figures 4.26 and 4.27 show typical optical micrographs of weld metals of SA516 and A709 steels, respectively. They show the different sizes of austenite grains produced using a welding current of 700 A and welding speeds of 5.3, 9.3, 12.3 and 15.3 mm/s. A close visual inspection reveals that the prior austenite grains were largest at the lowest welding speed (5.3 mm/s), which corresponded to the highest heat input (4.39 kJ/mm) and lowest cooling rate at this welding current (700 A). It was found in all cases that the prior austenite grain width decreased as the speed increased. This is understandable because at low welding speeds, the resultant high heat input produced large weld nuggets which took long time to solidify. As a result, the welds spent a long time in the high temperature range and produced large prior austenite grains. High welding speed resulted in reduced heat input but increased cooling rate which resulted in reduced dwell time at high temperature.

The relationship between the measured prior austenite grain width and welding speed is shown graphically in Figures 4.28 and 4.29 for SA516 and A709 steel welds, respectively. The grain width decreased with increasing welding speed for the welds of both steels. For a given welding current, increasing welding speed will reduce the heat input. With decreasing heat input and increased cooling rate, the weld will spend less time in the high temperature range after solidification to promote grain growth.

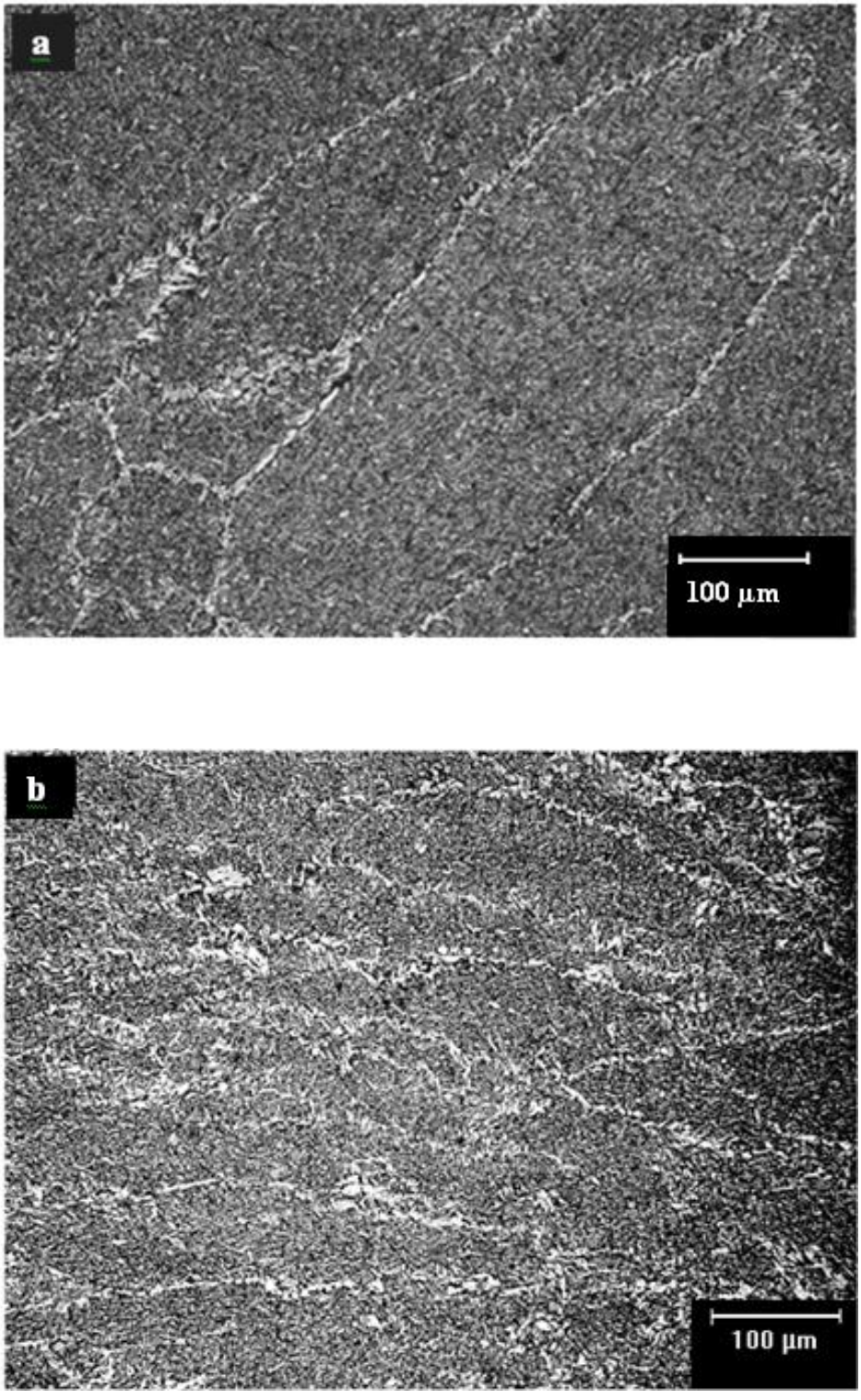

Figure 4.26. Micrographs showing prior austenite grains for SA516 steel weld metals produced with a welding current of 700 A and different welding speeds: (a) 5.3 mm/s, (b) 9.3 mm/s, (c) 12.3 mm/s and (d) 15.3 mm/s.

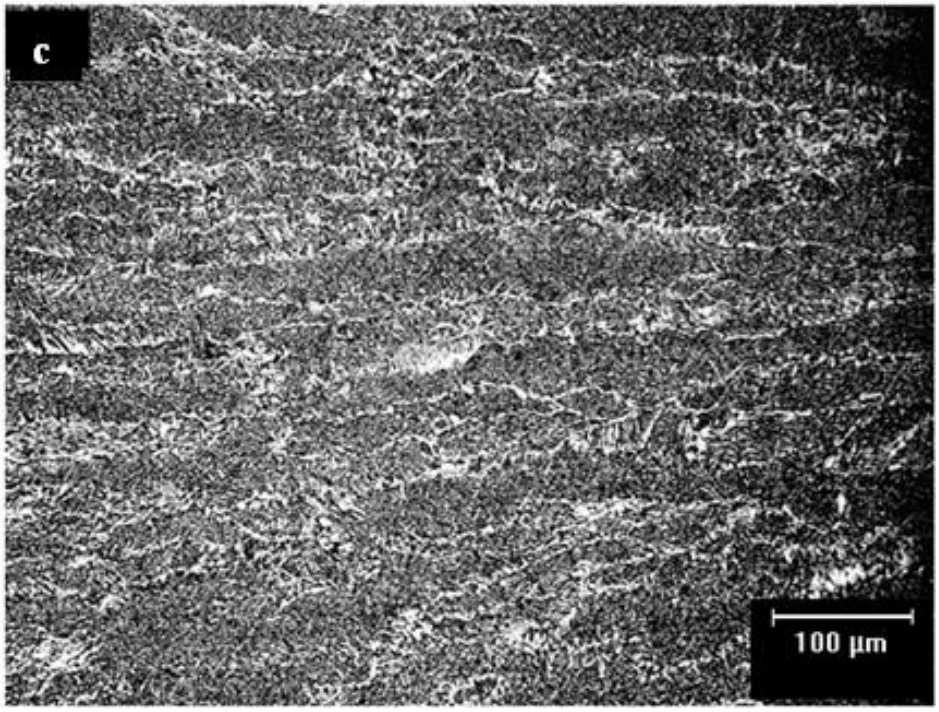

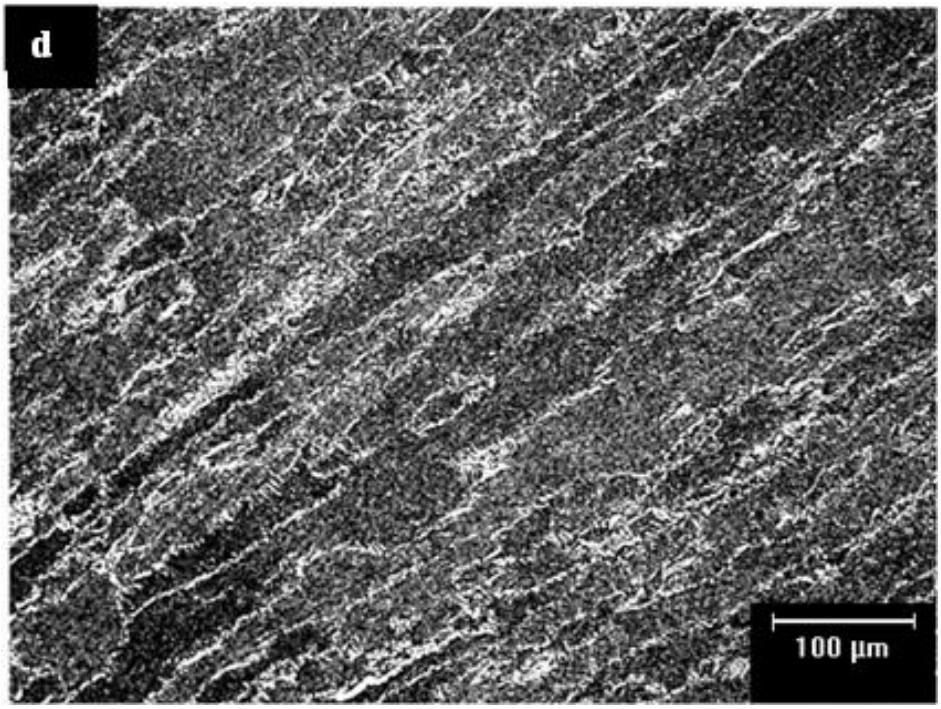

Figure 4.26 continued.

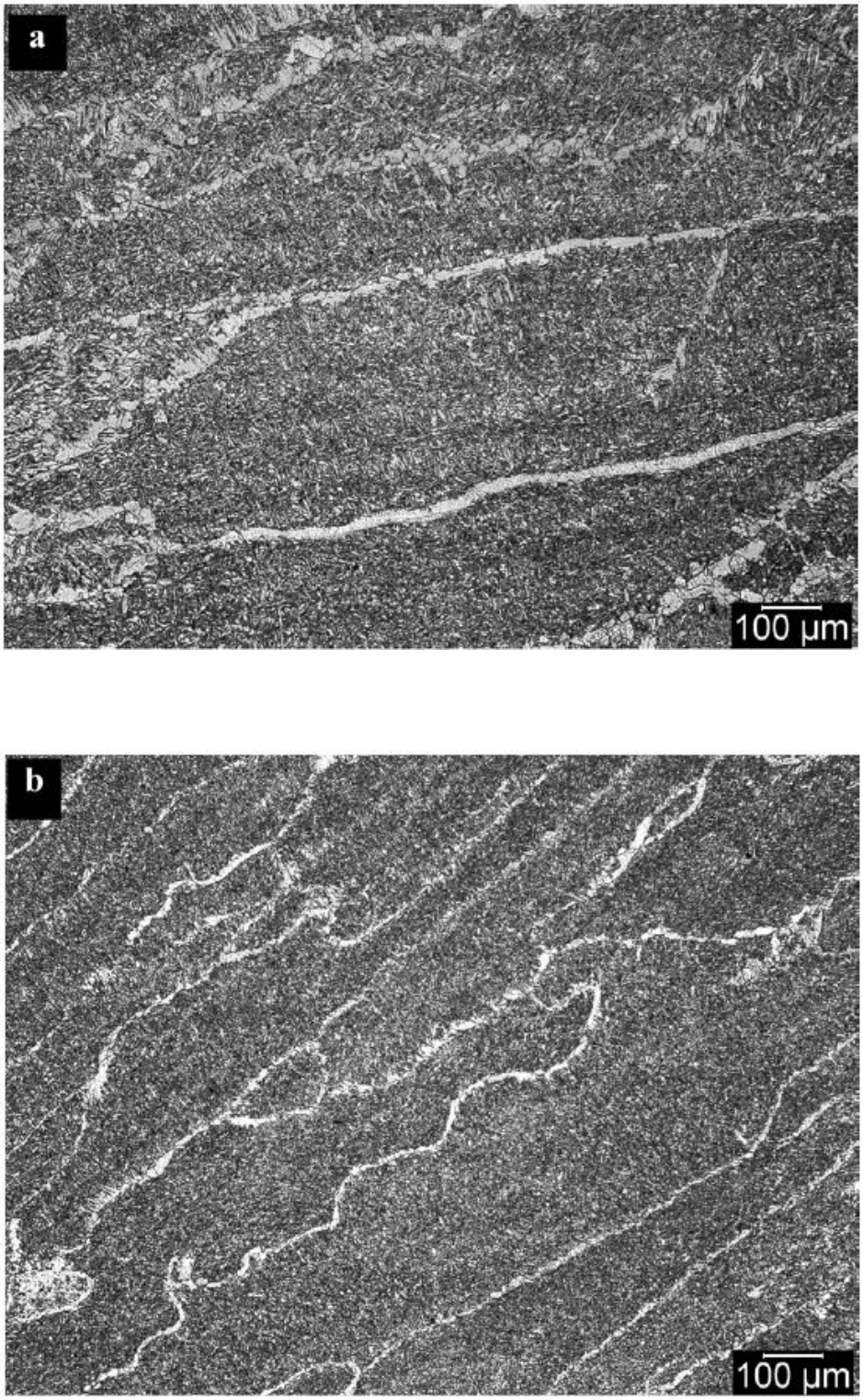

Figure 4.27. Micrographs showing prior austenite grains for A709 steel weld metals produced with a welding current of 800 A and different welding speeds: (a) 5.3 mm/s, (b) 9.3 mm/s, (c) 12.3 mm/s and (d) 15.3 mm/s.

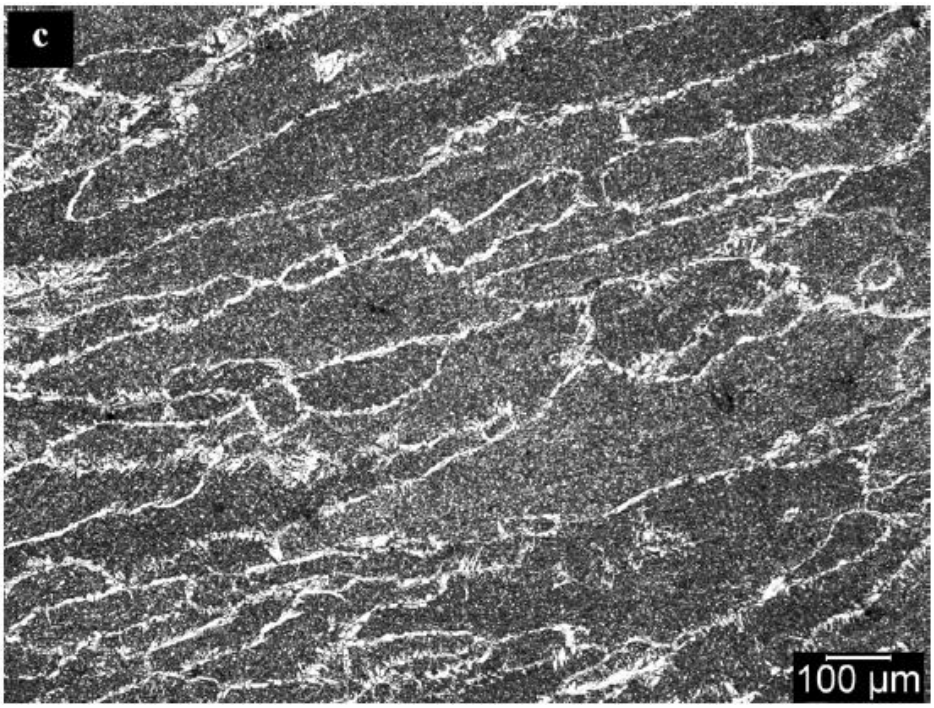

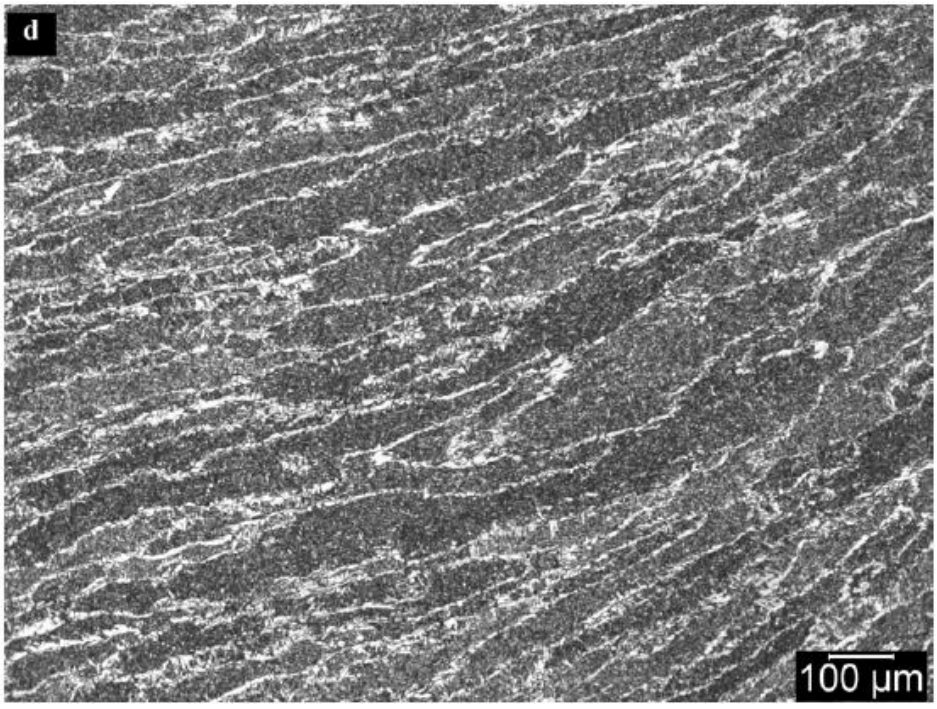

Figure 4.27 continued.

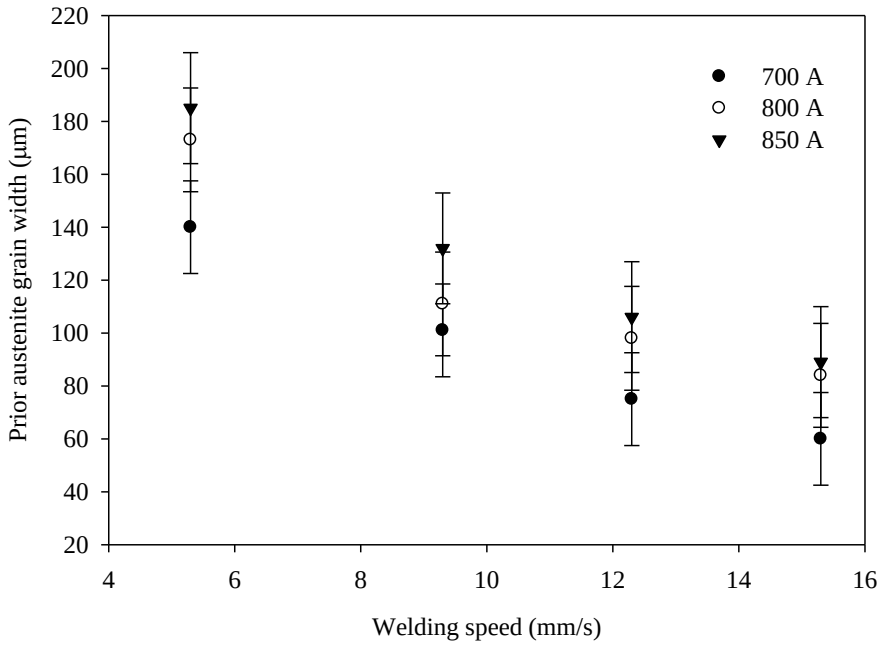

Figure 4.28. Variation of prior austenite grain width with welding speed for SA516 weld metals.

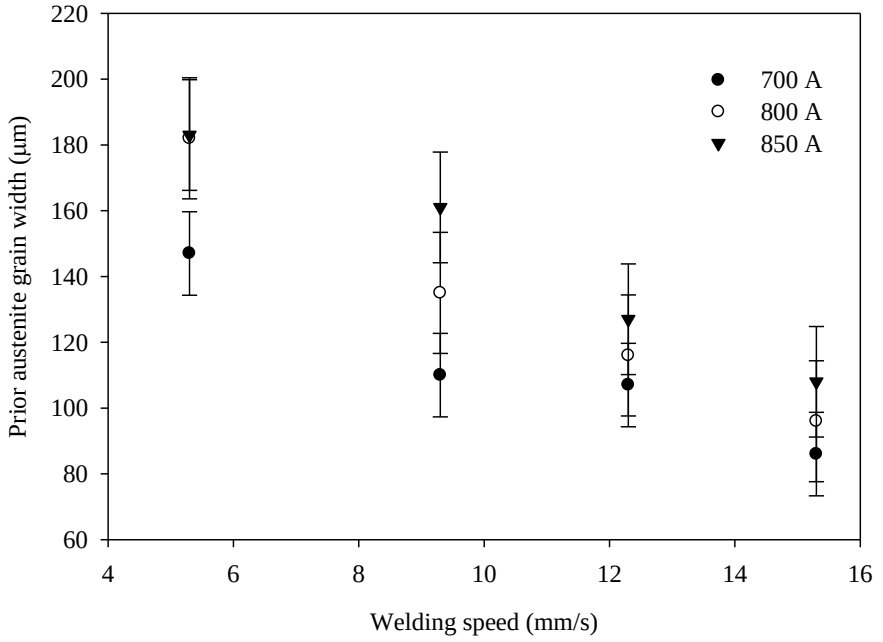

Figure 4.29. Variation of prior austenite grain width with welding speed for A709 weld metal.

4.5.2 Welding Current

Figures 4.30 and 4.31 show respectively optical micrographs of the weld metals of SA516 and A709 produced with a welding speed of 9.3 mm/s and different welding currents of 700 A, 800 A and 850 A. For both steels, large prior austenite grains were obtained as welding current increased. This was expected because increasing the welding current also increased the heat input which resulted in reduced cooling rate. Consequently, the WMs spent a long time at high temperatures during the austenite-to-ferrite transformation allowing grain coarsening. Results obtained from the prior austenite grain size measurements for both SA516 and A709 steel welds are shown respectively in Figures 4.32 and 4.33. In both cases the measured prior austenite grain width increased with increasing welding current.

The reason for the different effects of welding speed and current on the microstructure is that the weld bead size and cooling rate are affected differently when heat input is achieved by either increased welding current or by reduced welding speed. Increased welding current, as mentioned previously, increases metal deposition rate and, subsequently, increases HAZ width and grain coarsening. On the contrary, when heat input is achieved by decreasing welding speed at a fixed current, the metal deposition rate per unit length of weld bead increases because the electrode travel speed reduces.
The combined effect of increased heat input and metal deposition rate is to increase weld bead width and HAZ size. As the weld bead width increases with decreasing welding speed, increasing welding speed reduces the heat input delivered into the base plate and causes less filler metal to be deposited, resulting in a narrow weld bead.

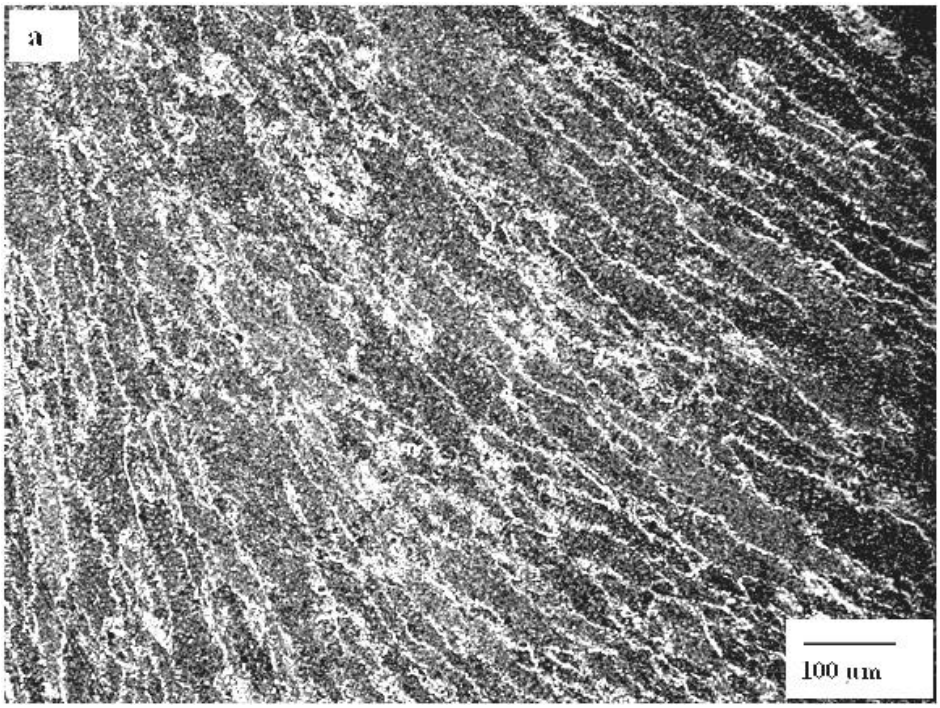

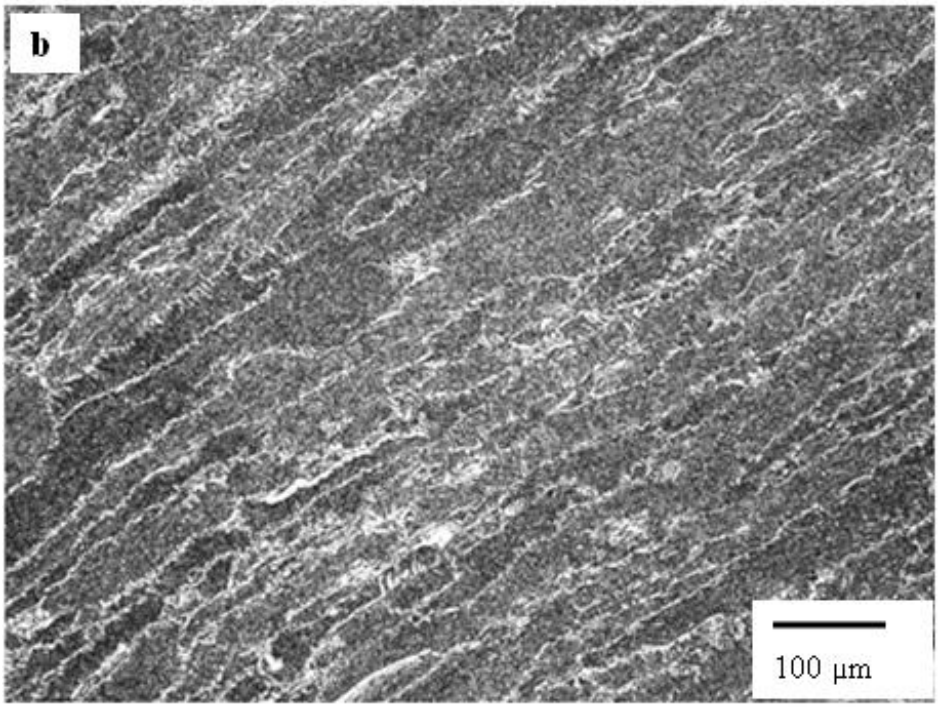

Figure 4.30. Typical micrographs of weld metals of SA516 showing prior austenite grains produced using a welding speed of 9.3 mm/s and different welding currents: (a) 700 A (b) 800 A and (c) 850 A.

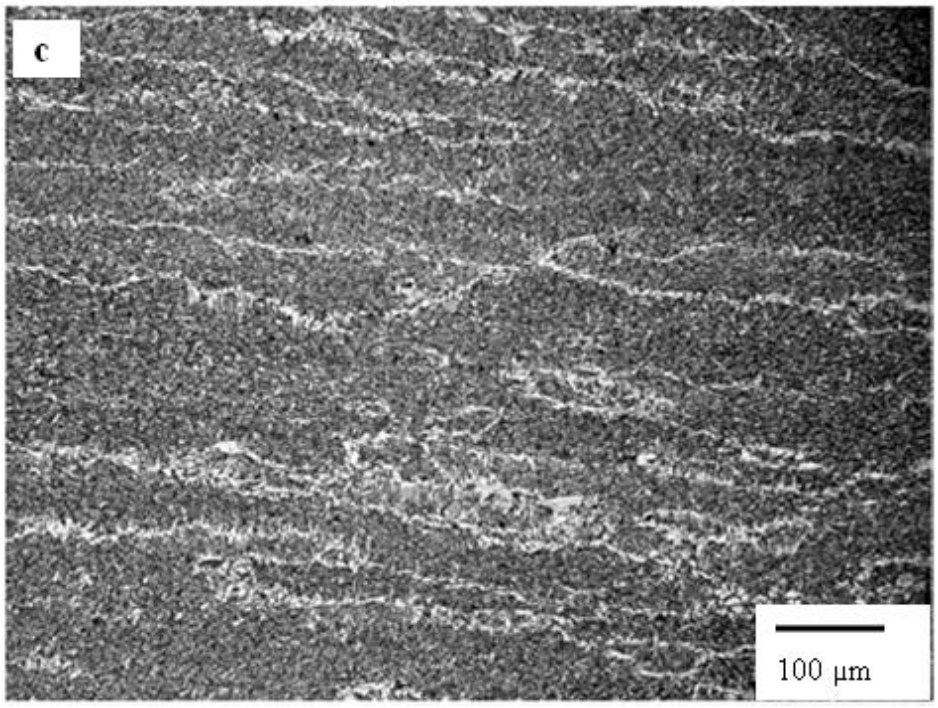

Figure 4.30 continued.

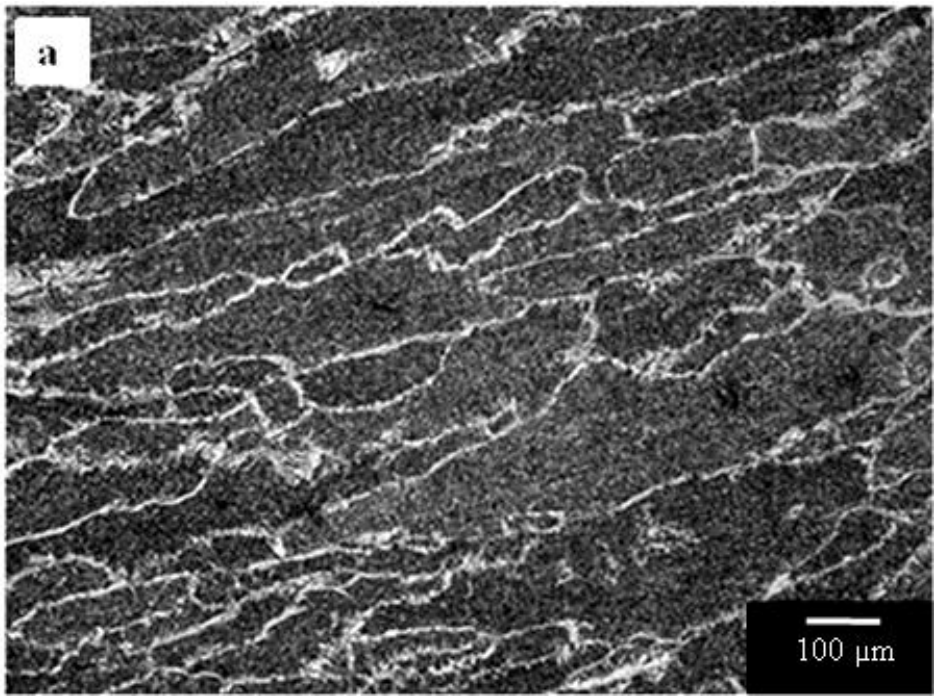

Figure 4.31. Typical micrographs of weld metals of A709 steel showing prior austenite grains produced using a welding speed of 9.3 mm/s and different welding currents: (a) 700 A (b) 800 A and (c) 850 A.

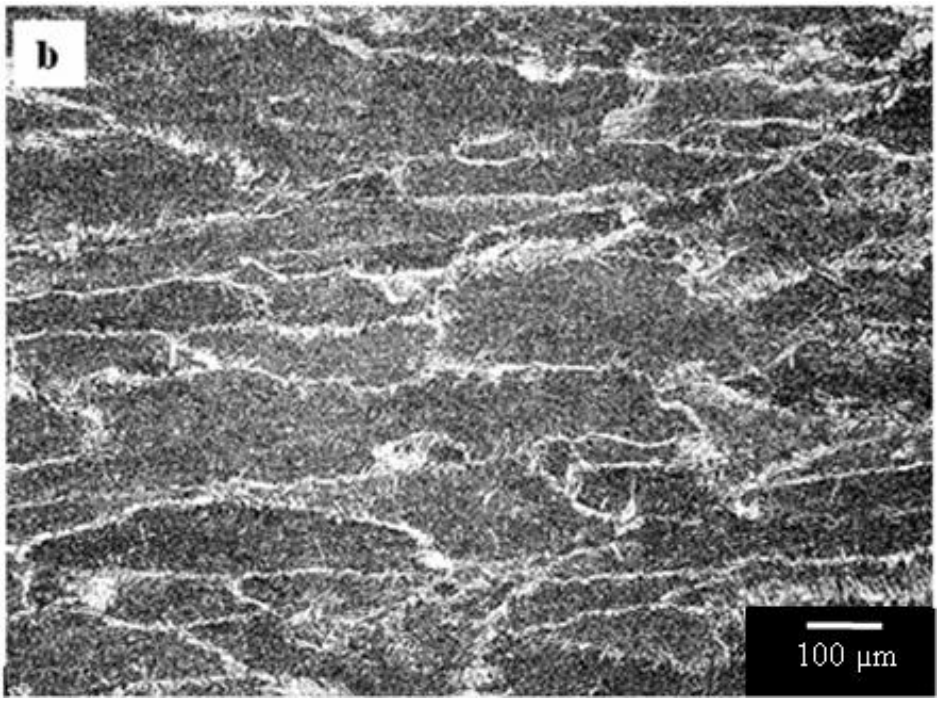

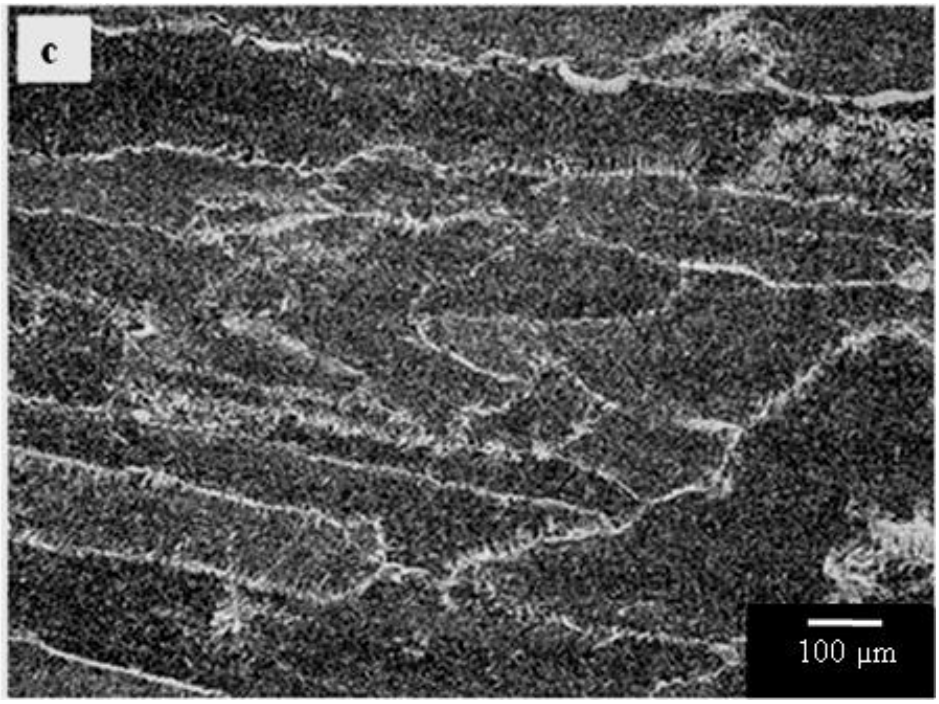

Figure 4.31 continued.

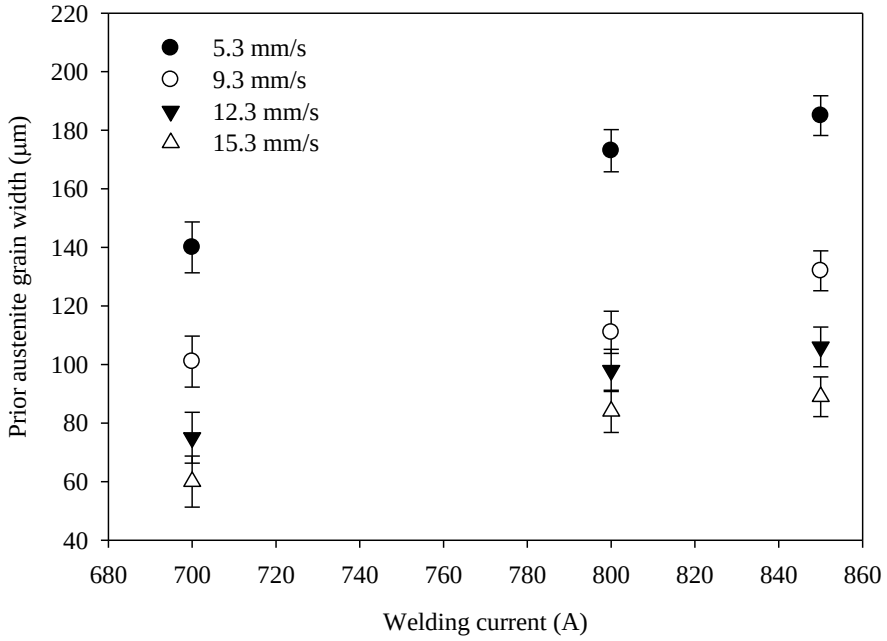

Figure 4.32. Variation of prior austenite grain width with welding current for SA516 weld metals.

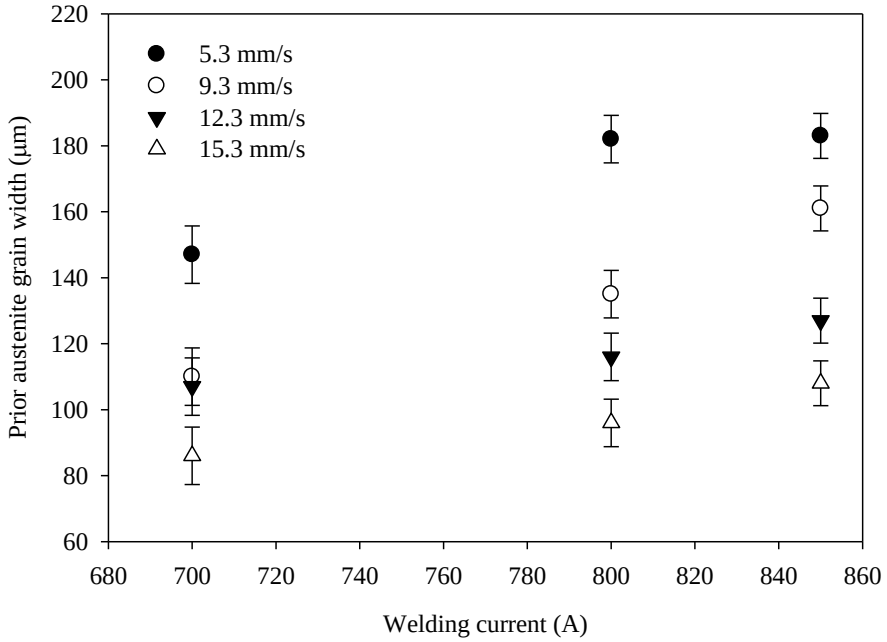

Figure 4.33. Variation of prior austenite grain width with welding current for A709 weld metals.

With decreased or increased volume of weld pool, heat transfer by conduction through the base metal sink is either decreased or increased and thin or thick HAZ is formed. This ultimately affects austenite grain growth in the CGHAZ. This effect is unlikely to be observed when the input parameters are lumped together as heat input.

4.5.3 Heat Input

The effect of heat input on the prior austenite grain width is shown in Figures 4.34 and 4.35 for SA516 and A709 steel welds, respectively. The prior austenite grain size increased with increasing heat input for weld metals of both steels. It was mentioned that austenite grain growth occurs after solidification during cooling in the high temperature range ~1200ºC [23]. High heat input and low cooling rate favour grain growth. It is generally accepted that the prior austenite grain size is affected by the weld metal oxygen content [83, 84]. The growth of austenite grains is an indication that there were not enough inclusion particles in the weld metal to restrict their growth.

From the above discussion in section 4.5, it can be deduced that the effect of heat input on the obtained WM microstructure did not depend only on the prior austenite grain size and the cooling rates but perhaps on other factors such as diffusion of alloying elements. Farrar *et al.* [49] reported that the diffusion of carbon was faster and a longer time was available in smaller austenite grains during GBF formation reaction than in large austenite grains.

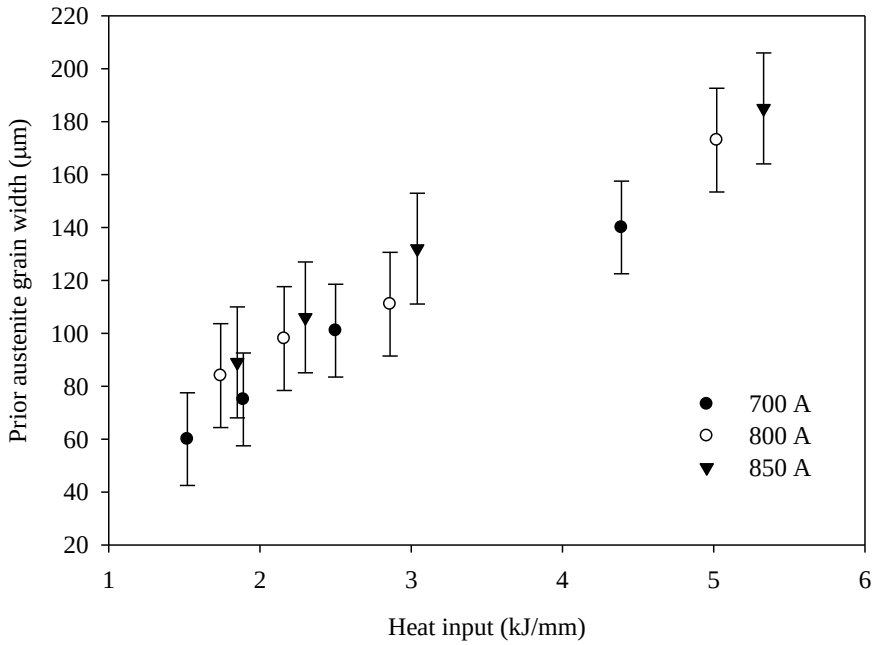

Figure 4.34. Variation of prior austenite grain width with heat input for WMs of SA516 steel.

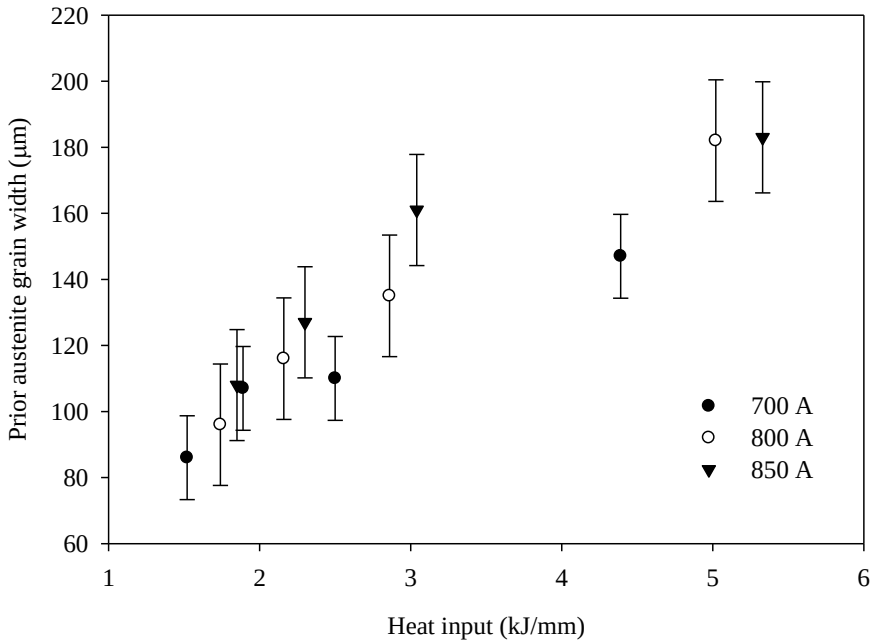

Figure 4.35. Variation of prior austenite grain width with heat input for WMs of A709 steel.

4.6 Determination of the Amounts of Various Ferrites in the Weld Metals of SA516 and A709 Steels.

The results of quantitative image analysis of the ferrite phases (WF, GBF and AF) present in the weld metals of SA516 and A709 steels are summarized in Figures 4.36 and 4.37. The figures show respectively the variation of proportion of weld metal ferrite with welding current for SA516 and A709 steel weld produced using 9.3 mm/s. As expected, the main austenite-to-ferrite transformation product was acicular ferrite ranging from 70.6 to 85.0% for SA516 steel welds and 72.5 to 87.8% for A709 steel welds.

A close examination of Figures 4.36 and 4.37 shows the AF amount increased as welding current increased from 700 A to 800 A. The increase in the AF amount was accompanied by a corresponding decrease in the amounts of GBF and WF. It is generally accepted that AF can form at the expense of high temperature ferrite products, such as GBF and WF. The reason for the AF increase can be attributed to the increase in the prior austenite grain size (approximately 140 to 173 μm) which occurred in the weld metals. As welding current increased further from 800 to 850 A, a decrease in the amount of AF occurred in both steels. The prior austenite grain size on the other hand continued to increase to from 173 to 185 μm (see Table B.1), which is contrary to the hypothesis that large prior austenite grains produce less GBF and thus increase the proportion of AF [14].

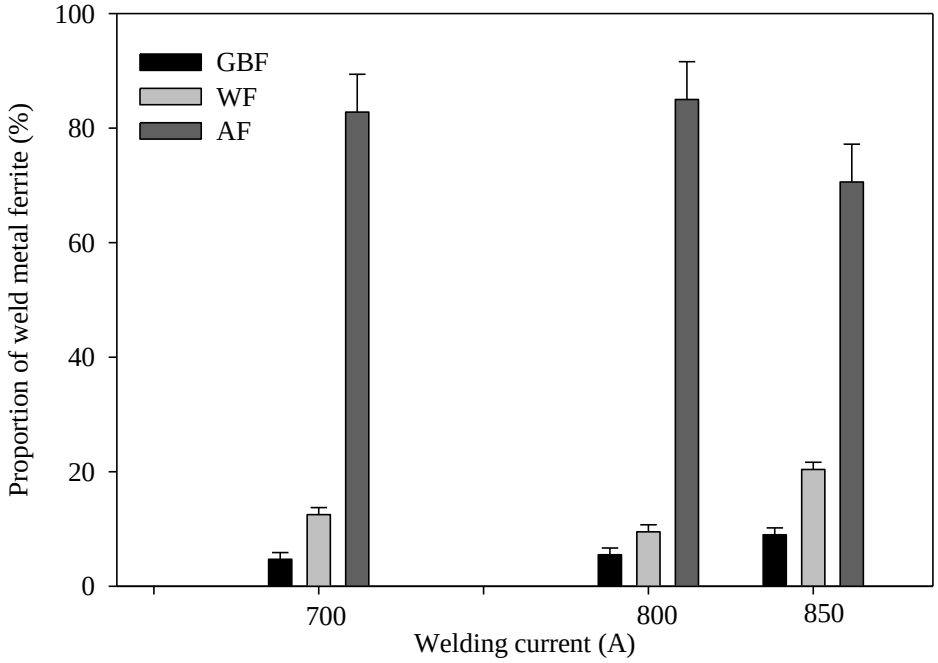

Figure 4.36. Variation of proportion of weld metal ferrite with welding current for SA516 steel welds produced using a welding speed of 9.3 mm/s.

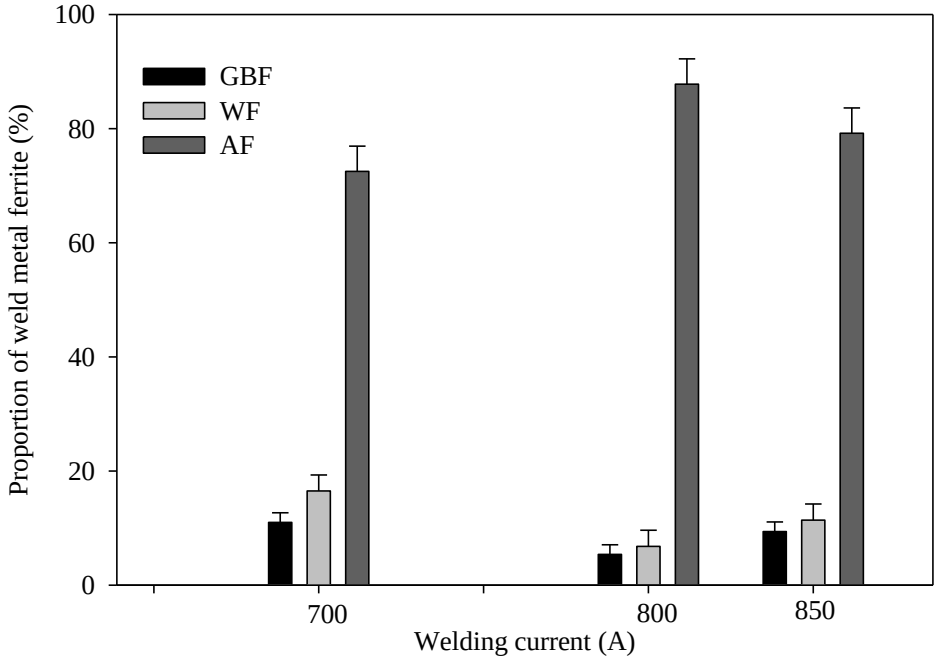

Figure 4.37. Variation of proportion of weld metal ferrite with welding current for A709 steel welds produced using a welding speed of 9.3 mm/s.

Viano *et al.* [99] reported that increasing heat input from 2 to 5 kJ/mm substantially increased the ferrite grain size from 25 to 60 μm for HSLA-80 steel welds. These researchers also reported that increasing heat input from 2 to 100 kJ/mm lowered the fraction of AF from 80% to 45% in the welded joints. The decrease in the proportion of AF obtained in the present study is much lower than in [99], probably due to the fact that the range of heat input used in both studies differed remarkably (2 to 100 kJ/mm as compared to 1.52 to 5.33 kJ/mm).

Figures 4.38 and 4.39 show respectively the variation of the amount of ferrites in the weld metal with variable welding speed at a fixed current of 800 A for SA516 and A709 weld metals. It can be seen from Figure 4.37 that the amount of weld metal ferrites did not change appreciably with variation in welding speed for SA516 steel. The reason for this is that the change in heat input achieved by varying welding speed did not change the weld metal chemistry since more of the base metal was melted and less dilution was obtained because the electrode melting rate was not much changed. Since the concentration of the different alloying elements in the weld metals remained almost the same, except for a few such as Al and Si (see Tables 4.1 and 4.2), the rate of diffusion was not expected to change much and hence the microstructure remained the same. For A709 steel welds, there was also no noticeable increase in the amount of AF (85.3 to 87.8%) as welding speed increased from 5.3 to 15.3 mm/s.

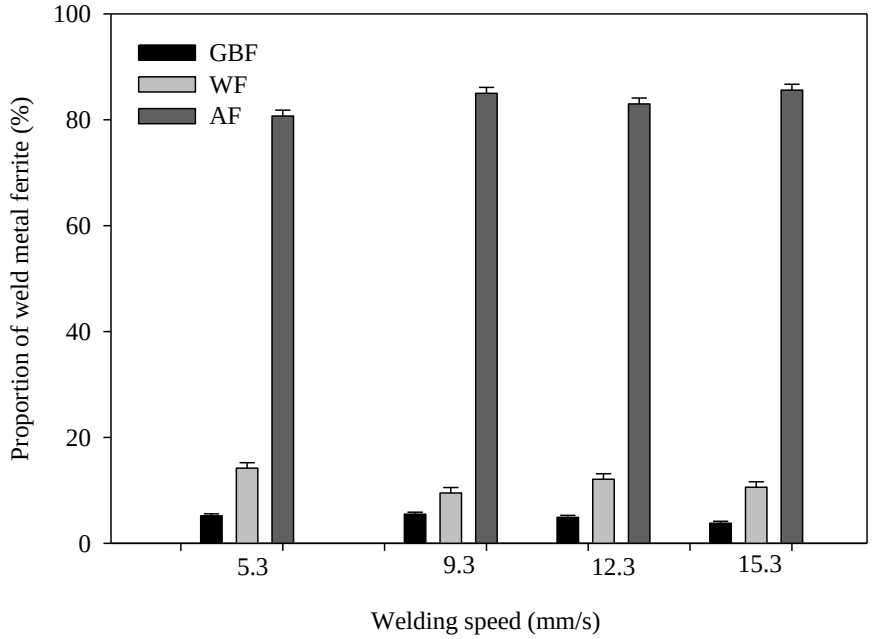

Figure 4.38. Variation of proportion of weld metal ferrite with welding speed for SA516 steel welds produced using a welding current of 800 A.

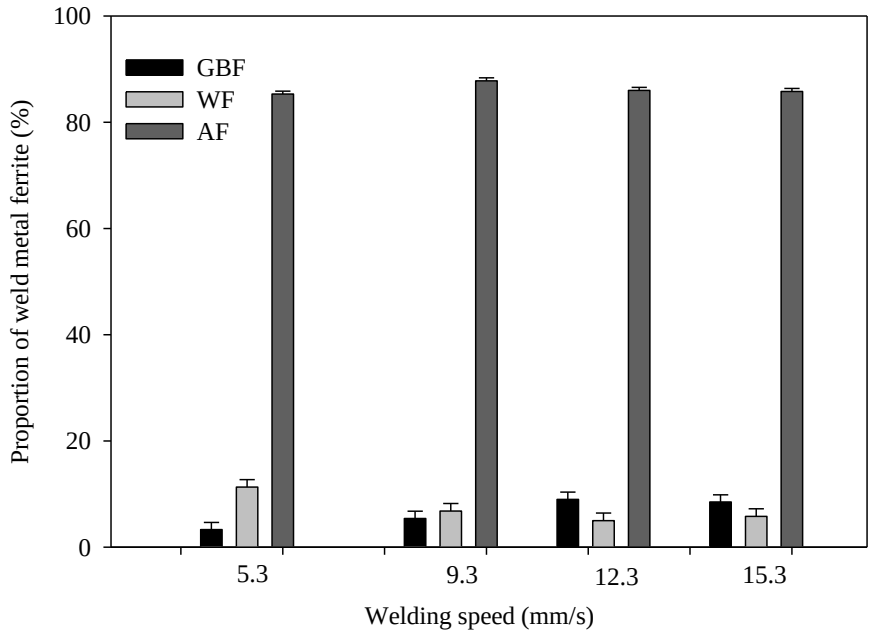

Figure 4.38. Variation of proportion of weld metal ferrite with welding speed for A709 steel welds produced using a welding current of 800 A.

4.7 X-ray Diffraction (XRD) Analyses

To ensure the weld quality, X-ray diffraction analyses were carried out to determine phase constitution and ascertain if there was any retained austenite within the weld metals. Figure 4.40 shows typical X-ray diffraction patterns obtained for the weld metal of SA516 steel produced using 850 A and 15.3 mm/s. The figure shows the peak positions where the incident X-ray beam has been diffracted by the crystal lattice. The unique set of five diffraction peaks that were recorded were compared with the X-ray diffraction data for α-Fe published by the Joint Committee on Powder Diffraction Standards (JCPDS) data card No. 6-696 [93]. There was a good match between the spectrum intensities. The diffraction spectrum indicated therefore that only the α-Fe phase was present in the weld metal. However, it is possible that the quantity of any residual retained austenite was below the detection limit of the XRD method used.

4.8 Process Variables and Microstructure

The results obtained in this study revealed the complex relation between welding process parameters and weld metal microstructure. The correlation of WM microstructure with any of the input parameters alone is inadequate. To better understand the combined effect of welding current and welding speed on WM microstructure, contour plots were employed. Figure 4.41 shows a contour plot welding current and speed and their effect on the amount of AF for SA516 steel weld metals. The numbers on the contour lines show the proportion of the ferrite in %. The maximum AF amount of 85% was obtained between welding current from 740 to 800 A and welding speed from 8 to 13 mm/s for SA516 steel.

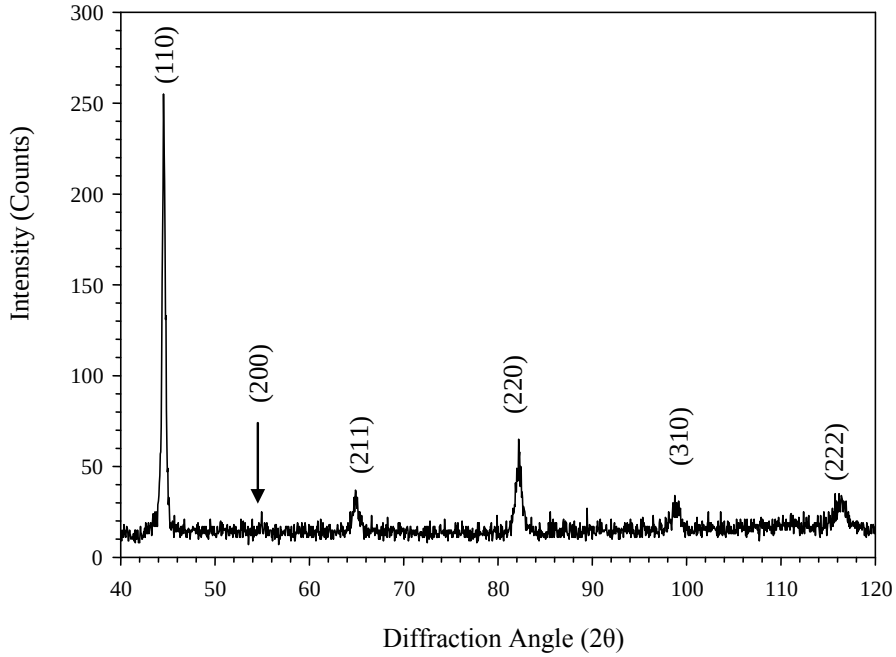

Figure 4.40. X-ray diffraction patterns from SA516 weld metal produced using a welding current of 850 A and a welding speed of 15.3 mm/s.

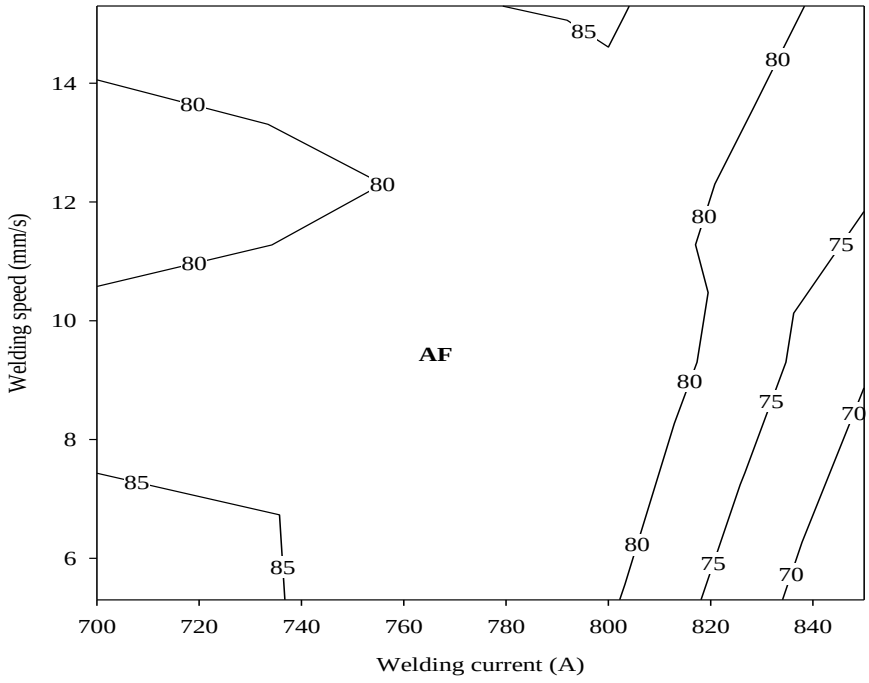

Figure 4.41 Combined effect of welding speed and current on volume fraction of acicular ferrite (AF) for SA516 welds.

The contour plots of the combined effect of welding current and speed on grain boundary ferrite (GBF) and Widmanstatten ferrite (WF) are shown respectively in Figures 4.42 and 4.43. The plots show that the amount of AF is high whenever the sum of GBF and WF amount is small.

Figure 4.44 shows a similar contour map indicating the range for optimum amount of AF for A709 steel weld metals. An optimum amount of 85% AF was obtained at 800 A. This amount of AF is obtainable at all the welding speeds between 5.3 to 15.3 mm/s. Figures 4.45 and 4.46 show the combined effects of welding current and speed on the weld metal grain boundary ferrite and Widmanstatten ferrite, respectively. However, Figure 4.45 shows that the least amount of GBF (4 to 6 %) was obtainable at welding currents below 800 A. From Figure 4.46, the lowest amount of WF (10 %) was obtained in the current range 780 to 800 A and speed range 8 to 9 mm/s.

4.9 Microstructural Analysis and Nucleation of Acicular Ferrite

SEM and TEM analyses were carried out to establish the possible role of inclusions on the nucleation of AF and to understand why some inclusions favor the nucleation of AF in the weld metal. SEM and EDS were employed primarily to evaluate the morphology and elemental compositions of the inclusions in the weld metals. TEM analysis was carried out using carbon extraction replicas and thin foil specimens.

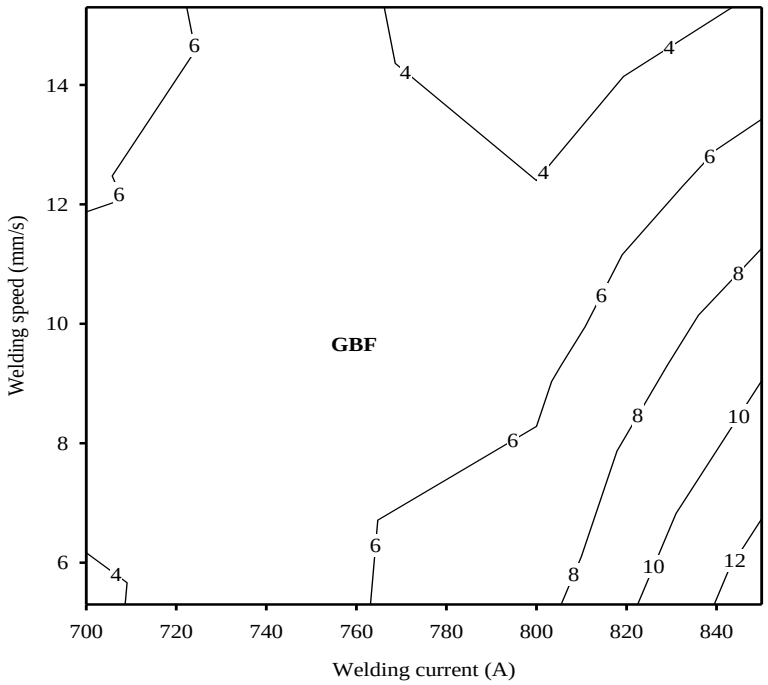

Figure 4.42 Combined effect of welding speed and current on volume fraction of grain boundary ferrite (GBF) for SA516 welds.

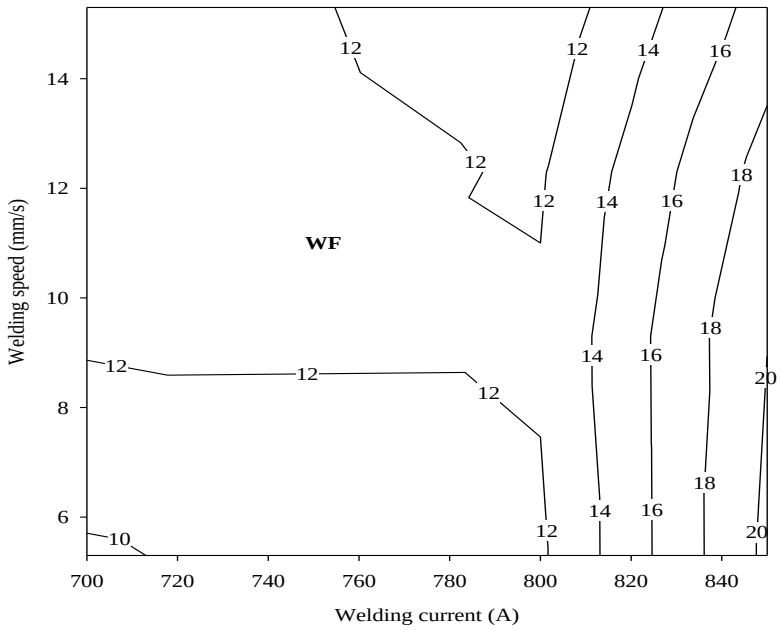

Figure 4.43 Combined effect of welding speed and current on volume fraction of Widmanstatten ferrite (WF) for SA516 welds.

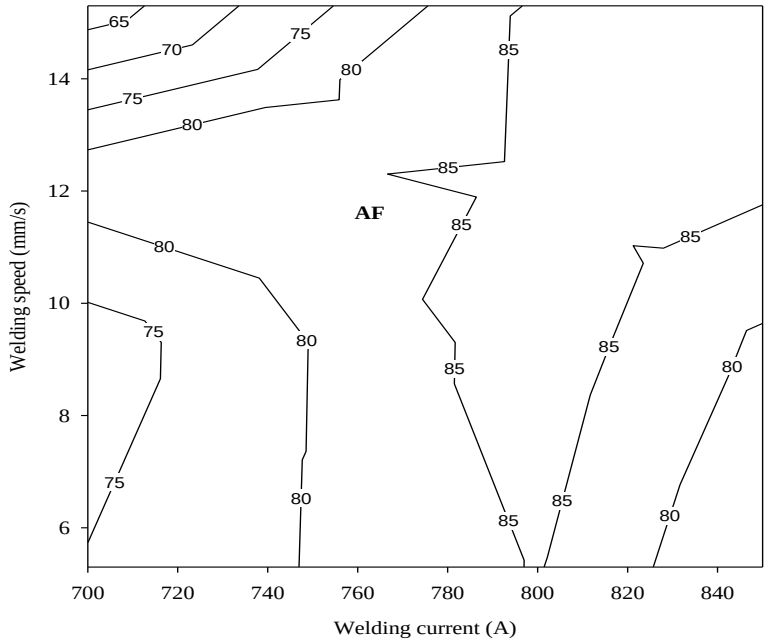

Figure 4.44 Combined effect of welding speed and current on volume fraction of acicular ferrite (AF) for A709 welds.

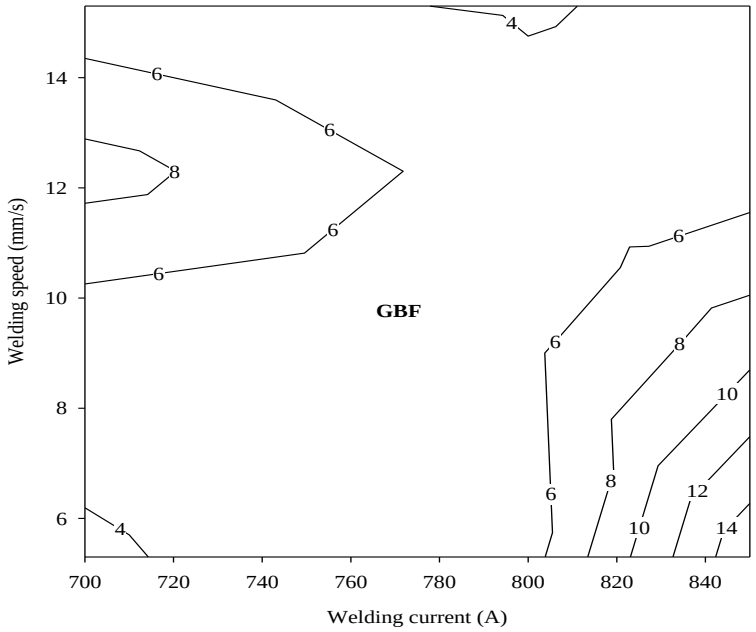

Figure 4.45 Combined effect of welding speed and current on volume fraction of grain boundary ferrite (GBF) for A709 welds.

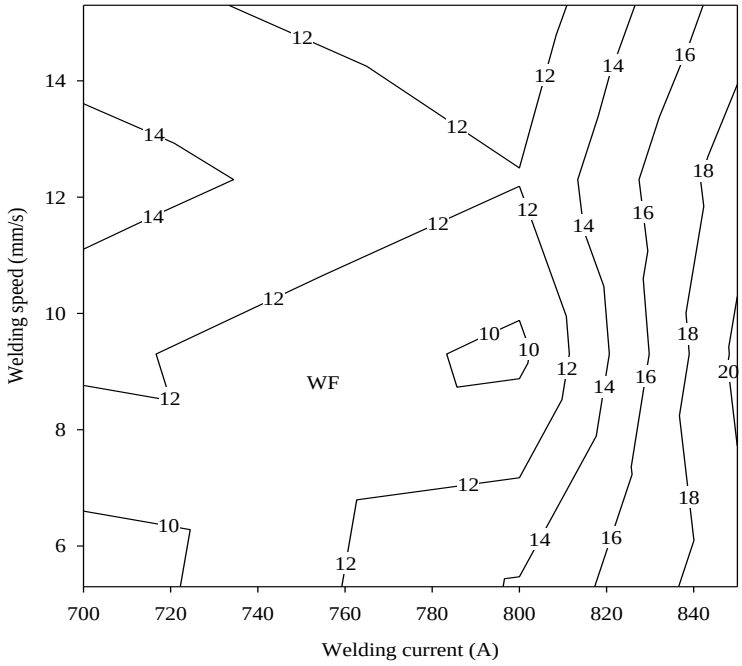

Figure 4.46 Combined effect of welding speed and current on volume fraction of Widmanstatten ferrite (WF) for A709 welds.

4.9.1 Inclusions Analysis using SEM

Selected weld samples were polished and examined under SEM. Figure 4.47 shows typical SEM micrographs of the types of inclusions observed in the weld metals of both SA516 and A709 steels. Figure 4.47(a) shows inclusions from polished unetched A709 weld metal. A spherical smooth inclusion is shown in this micrograph. Figure 4.47(b) is an example of the faceted multi-sided type of inclusion. Upon closer examination of the faceted inclusions, they seem to be a conglomeration of a number of inclusions. Further examination of some etched weld samples showed that some of the inclusions appeared to promote the nucleation of AF. It was established after several observations that only some of the spherical inclusions nucleated AF. The faceted inclusions did not nucleate AF.

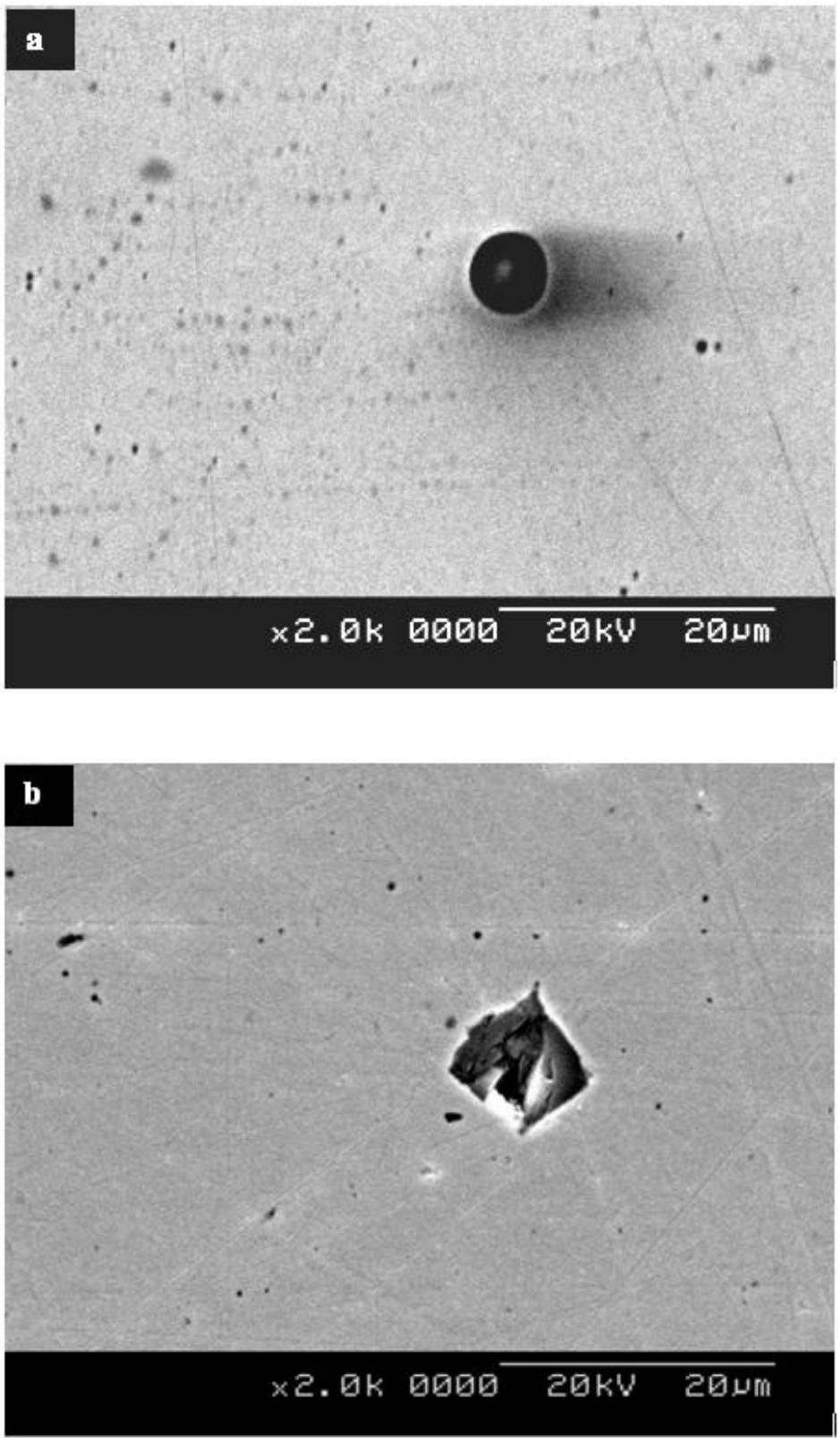

Figure 4.47. SEM micrographs showing the two types of inclusions found in the weld metals; (a) spherical inclusions (SA516) and (b) faceted inclusions (A709).

A close examination of polished and etched WM samples showed that acicular ferrite nucleated on some spherical inclusions as shown in Figure 4.48. Also, it can be seen from Figure 4.48 that although some of the inclusions are spherical, they did not nucleate AF. An example of a non-AF-nucleating faceted inclusion is shown in Figure 4.49.

4.9.2 Weld Metal Inclusions Chemical Composition Analysis using SEM

The EDS spectra of typical spherical and faceted inclusions found in SA516 WM are shown in Figure 4.50. A summary of the results of elemental compositions of inclusions obtained for the spherical and faceted inclusions in SA516 and A709 steel weld metals is tabulated in Table 4.4. It shows that the nucleating spherical inclusions were rich in aluminum, manganese and oxygen. The results also indicate that there are common basic elements in the inclusions of both steels. However, the relative proportions of the major elements varied for inclusions found in SA516 and A709 steel weld metals. This was expected because A709 and SA516 steels have different chemistry.

4.9.3 Inclusion Size Distribution

Figure 4.51 shows the size distribution obtained for spherical inclusions found in SA516 steel weld metals. The average diameter of the particles ranged from 0.4 to 0.6 μm. It was estimated from the graphed area that approximately 62% of the inclusions have diameters within this range.

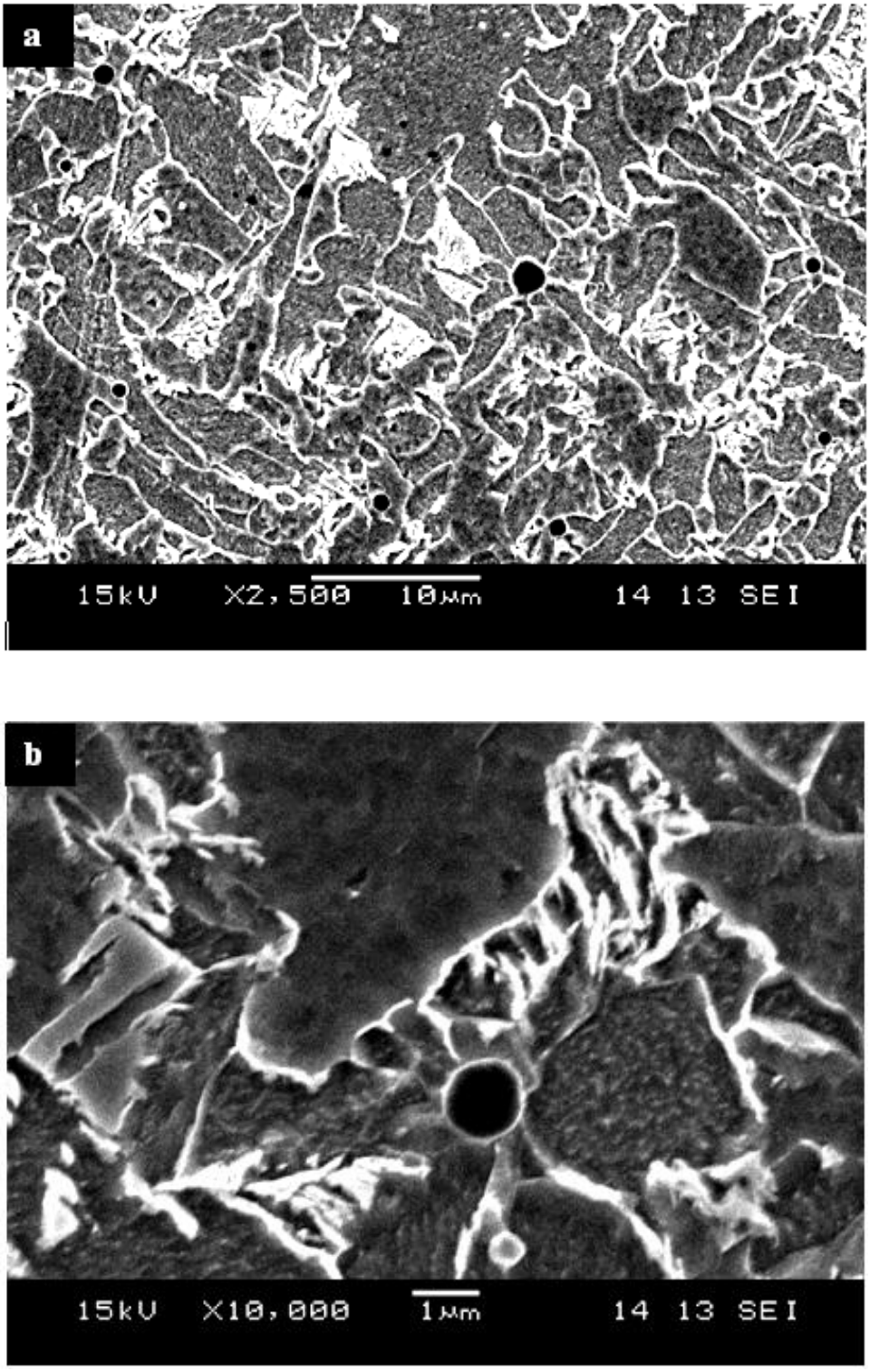

Figure 4.48. (a) SEM micrograph showing acicular ferrite nucleation on spherical inclusion for SA516 weld metal produced using 800 A and 12.3 mm/s (b) enlarged view of a nucleating spherical inclusion.

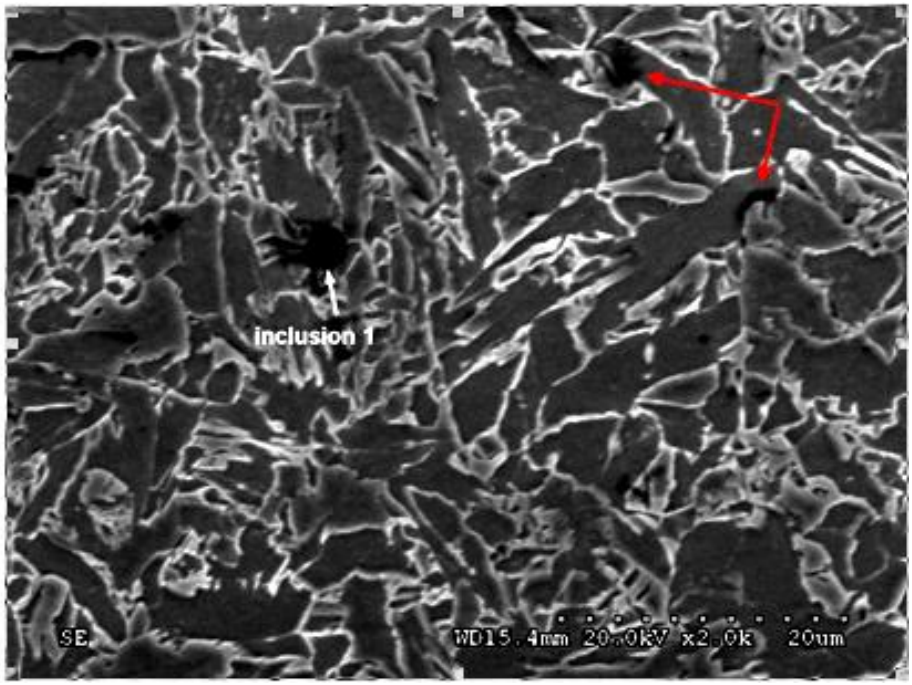

Figure 4.49. SEM micrograph showing non-AF-nucleating faceted inclusions in SA516 weld metal produced using 800 A and 12.3 mm/s.

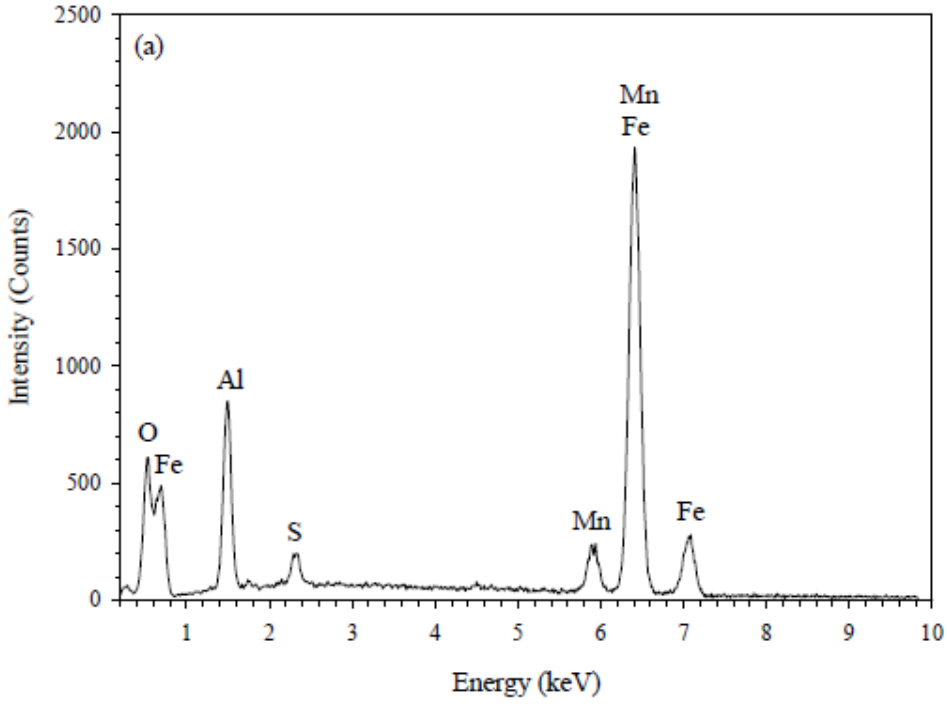

Figure 4.50. Typical EDS spectra obtained for inclusions in SA516 weld metal: (a) spherical inclusions (b) faceted inclusions.

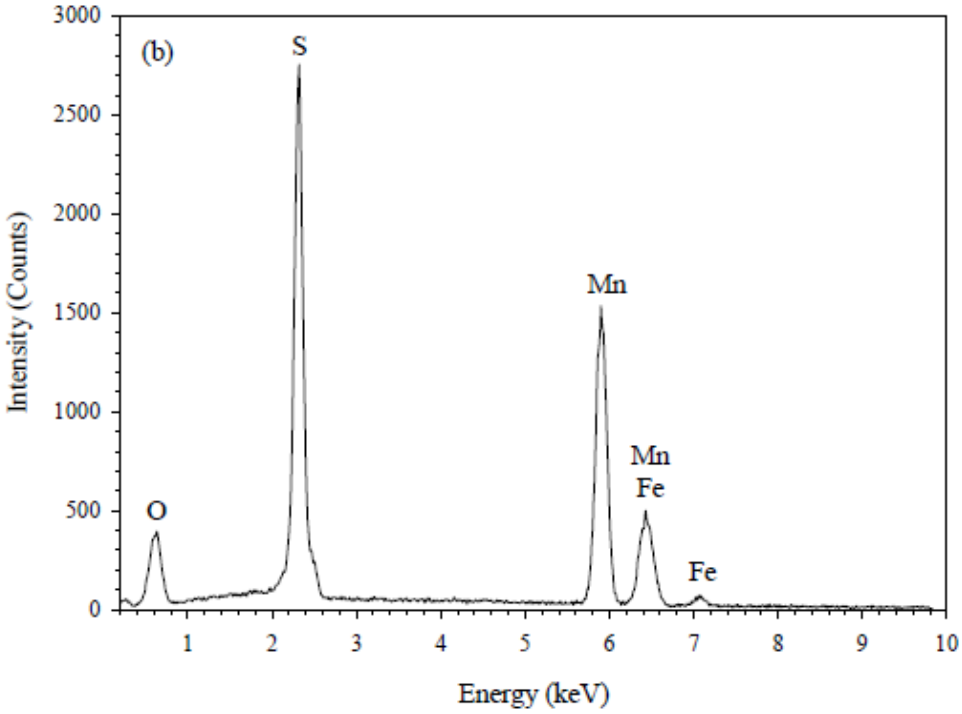

Figure 4.50 continued.

Table 4.4. SEM chemical compositions of typical inclusions in the weld metals of SA516 (PV) and A709 (WT) steels. (S = spherical inclusion; F = faceted inclusion).

Weld	Elements wt.%								
No.	Si	Mn	Al	Ca	S	Ti	Mg	O	Fe
PV(S)	4.02	2.48	5.47	4.87	-	0.64	1.41	22.42	52.44
PV(F)	2.18	7.10	20.45	4.87	2.68	0.64	1.41	23.46	75.12
WT(S)	16.75	14.58	18.68	23.65	-	3.25	0.69	17.32	-
WT(F)	7.91	56.85	18.38		8.28	8.15	-	0.44	-

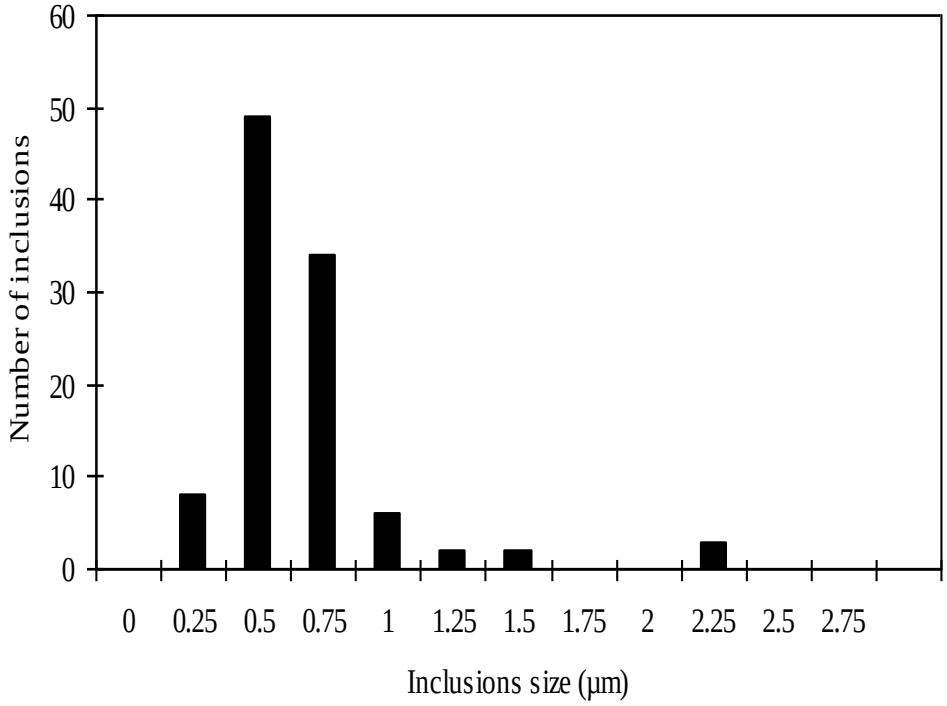

Figure 4.51. Size distribution for inclusions found in the weld metals of SA516 steels.

4.10 TEM Analysis

TEM was used to investigate AF development in the WMs of the two steels. Figures 4.52 and 4.53 show TEM bright field micrographs (extraction replica) of two adjacent spherical inclusions and a faceted inclusion in the WM of SA516 produced using 800 A and 12.3 mm/s. These particles were subsequently analyzed using EDS to understand their chemical compositions.

Figure 4.54 shows typical TEM thin foil micrographs of AF which nucleated on two spherical inclusions found in the WM of A709 steel produced using 800 A and 12.3 mm/s. The ferrite lath structures of AF can be seen emanating from the inclusions.

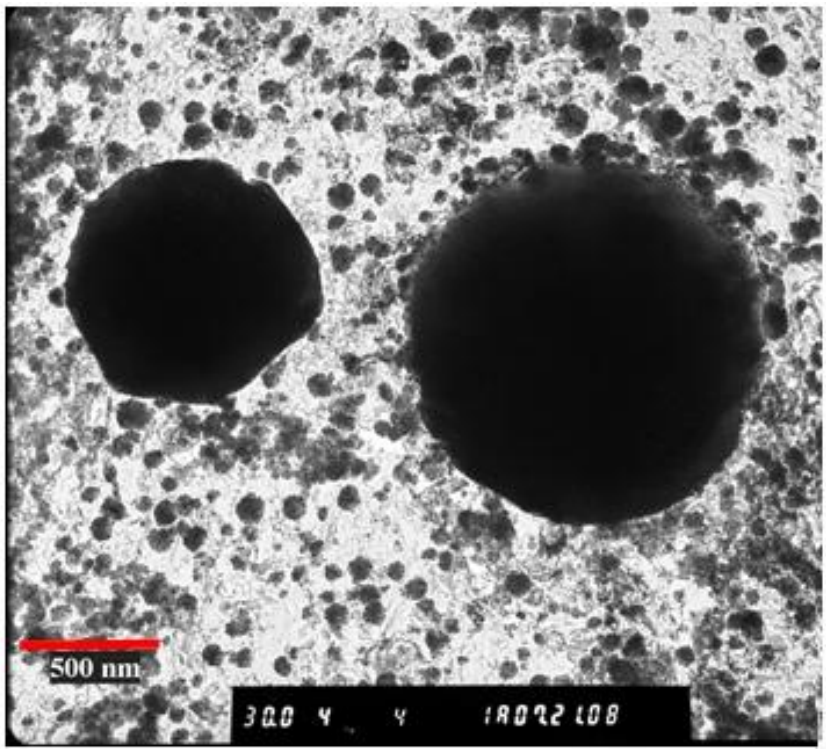

Figure 4.52. TEM bright field micrograph (carbon extraction replica) showing spherical inclusions in the WM of SA516 steel.

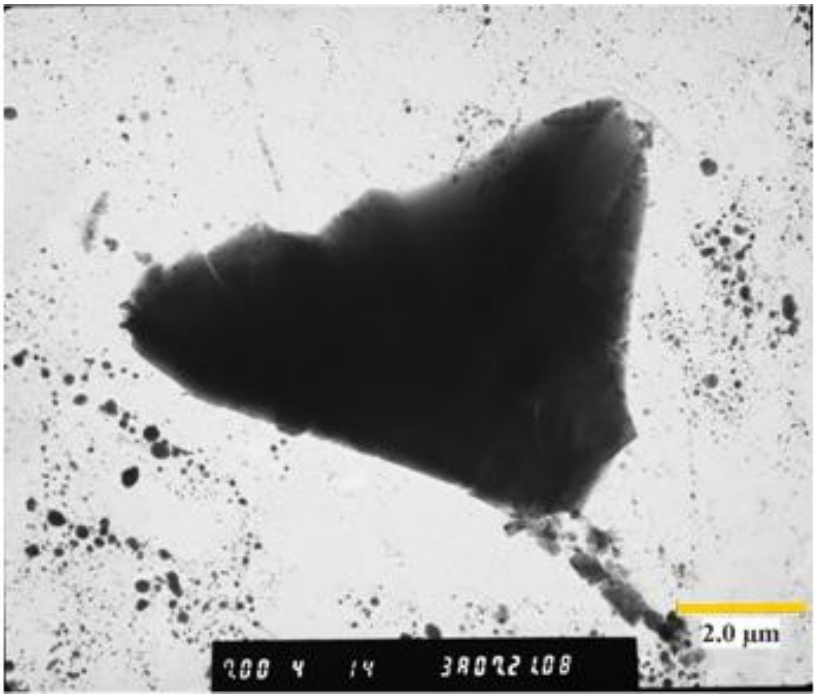

Figure 4.53. TEM bright field micrograph (carbon extraction replica) showing a faceted inclusion found in the WM of SA516 steel.

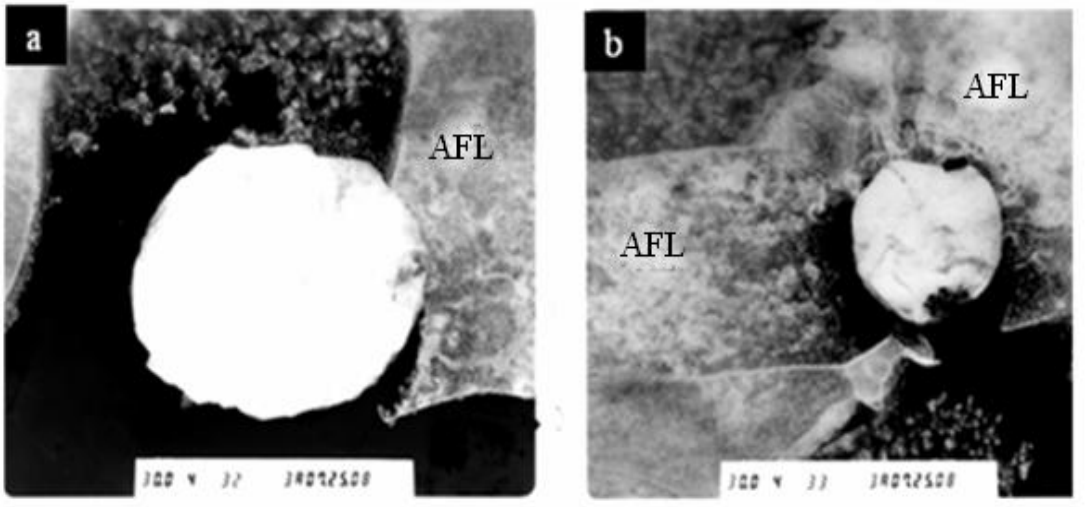

Figure 4.54 (a-b). TEM thin foil micrographs showing AF which nucleated on spherical inclusions in the WM of A709 steel produced using 800 A and 12.3 mm/s
(AFL = acicular ferrite lath).

4.10.1 EDS Line Scanning of Inclusions

TEM EDS was used to carry out a line scan through a typical spherical and a faceted inclusion to determine if there was any difference in chemistry that would influence acicular ferrite nucleation. The TEM micrographs of the inclusions, the line scanned through the inclusions and their elemental distributions are shown in Figure 4.54. The results indicate the spherical inclusions are composed of oxygen, silicon, manganese, aluminum and iron. The faceted inclusion is composed mostly of silicon. The reason for the difference in inclusion composition is not clear and will need further investigation.

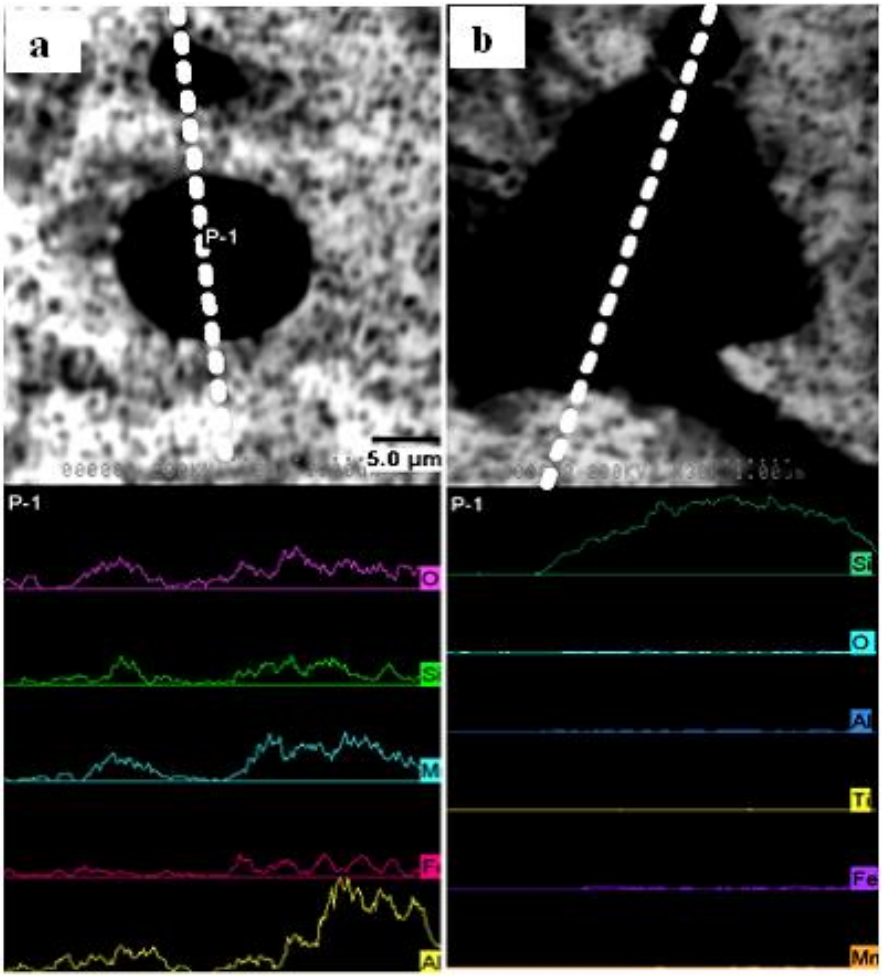

Figure 4.55. TEM EDS line scan through different types of inclusions found in the WM of SA516: (a) two spherical inclusions and (b) through faceted inclusion.

4.11 Statistical Analysis

4.11.1 Regression Analysis

The regression analysis relates the input variables of welding current and speed to the response variables: AF, GBF and WF. The model was fitted to the experimental results shown in Table B.2 in Appendix B using SYSTAT-11 statistical analysis software.

4.11.2 Model Predicting the Amount of Acicular Ferrite (AF) in the WM of A709 Steel.

The regression equation relating the amount of acicular ferrite (AF) produced in the WM of A709 steel to the welding process variables (current and speed) is:

$$AF = -752.36 + 2.20I - 6.69S - 0.17S^2 + 0.01IS \quad (4.1)$$

where, AF is the amount of acicular ferrite (%), I is welding current (A) and S is the welding speed (mm/s).

The quadratic term in current (I) is absent from this expression compared to the model equation 3.3. The regression coefficients pertaining to equation (4.1) and the analysis of variance (ANOVA) for the model are presented in Table B.3 of Appendix B. The adequacy of the model was checked with the residuals obtained and tested by the ANOVA technique. According to this technique, if the calculated value of the model's *F*-statistic is equal to or more than its tabulated value for a confidence level of 95%, then the model is adequate [98]. The *F*-statistic value, calculated as the ratio variance of mean sum of regression to the mean sum of errors as shown in Table B.3, is 468.37. At 95% confidence, the critical (tabulated) *F*-statistic = 4.28. The critical *t*-statistic is 1.796 for the 12 observations used in this study. The least *t*-statistic value for the regression coefficients was β_2 = -1.14, which is the linear term in welding speed. This means the term is non-significant. The raw *R*-squared value, which indicates the goodness of the fit, was 1.00 and the adjusted *R*-square (corrected) value was 0.75. Figure 4.56 shows the plot of the residuals versus the initial model predictions.

A close look at the residuals plot shows an outlier in the data for the test sample produced using 700 A and 9.3 mm/s which might be the source of the difference in the R-square values. Therefore, it was removed and the data re-analyzed using the same model. The model predictions and analysis of variance without the outlier data are shown in Table 4.5. The equation without the outlier is:

$$AF = -887.91 + 2.59I - 11.60S - 0.07S^2 + 0.02IS \quad (4.2)$$

The raw R-square and corrected R-square values are 1.00 and 0.98, respectively. The residuals plot for the data with the outlier removed is shown in Figure 4.57. There is a fairly good spread of data around the horizontal zero line. The tabulated *F*-statistic value is 4.95, whereas the model *F*-statistic is 4399.68. Since the calculated *F* value is greater than the tabulated *F*-value, the adequacy of the model is established. The *t*-statistic for the 11 observations is 1.812. Compared to the *t*-statistic values of the predicted regression coefficients in Table 4.5, only the *t*-value of β_4 is lower than the critical *t*-value. Therefore the quadratic term in welding speed is non-significant. The interaction effect of welding current and speed on the amount of AF formed in the WM of A709 steel is shown in Figure 4.58. The amount of AF increased to a maximum of approximately 87 % at 800 A and 12 mm/s and subsequently decreased with current. This value compares well with the value of 85% obtained for AF from Pax-it image analysis in section 4.6 (see Figure 4.44).

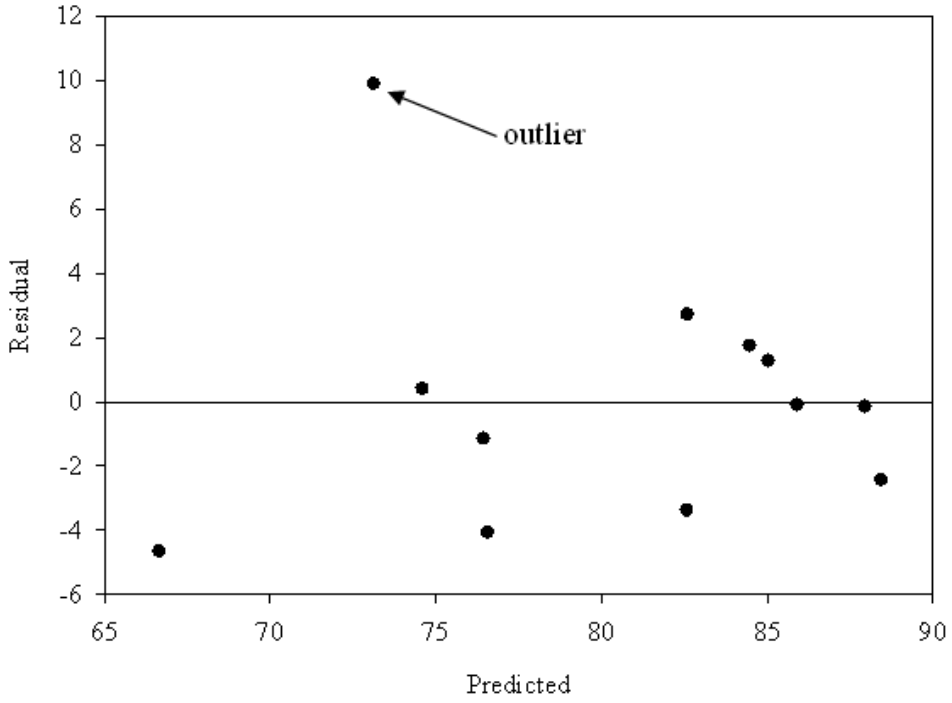

Figure 4.56. Plot of residuals for the initial model prediction for acicular ferrite (AF) in A709 steel weld metal.

Table 4.5 Model estimates without outlier data for acicular ferrite (AF) produced in the WM of A709 Steel.

(a) Regression Coefficients

Regression Coefficients	Estimated Regression Coefficients(ERC)	Asymptotic Standard Error (ASE)	ERC/ASE (t*)	Confidence Interval < 95%>	
				Lower	Upper
B_0	-887.91	125.66	-7.07	-1210.93	-564.90
β_1	2.59	0.33	7.96	1.75	3.43
β_2	-11.60	1.97	-5.88	-16.66	-6.53
β_3	-0.00	0.00	-8.22	-0.00	-0.00
β_4	-0.07	0.04	-1.61	-0.19	0.04
β_5	0.02	0.00	7.78	0.01	0.02

(b) Analysis of Variance

Source of variable	Sum of squares	Degree of freedom	Mean square	F statistic model	F-statistic tabulated
Regression	71274.78	6	11879.13	4399.68	4.95
Error	13.90	5	2.78		
Total	71288.68	11			

(c) R-square

Raw R-square (1-Residual/Total)	1.00
Mean corrected R-square (1-Residual/Corrected)	0.98
R(observed vs predicted) square	0.98

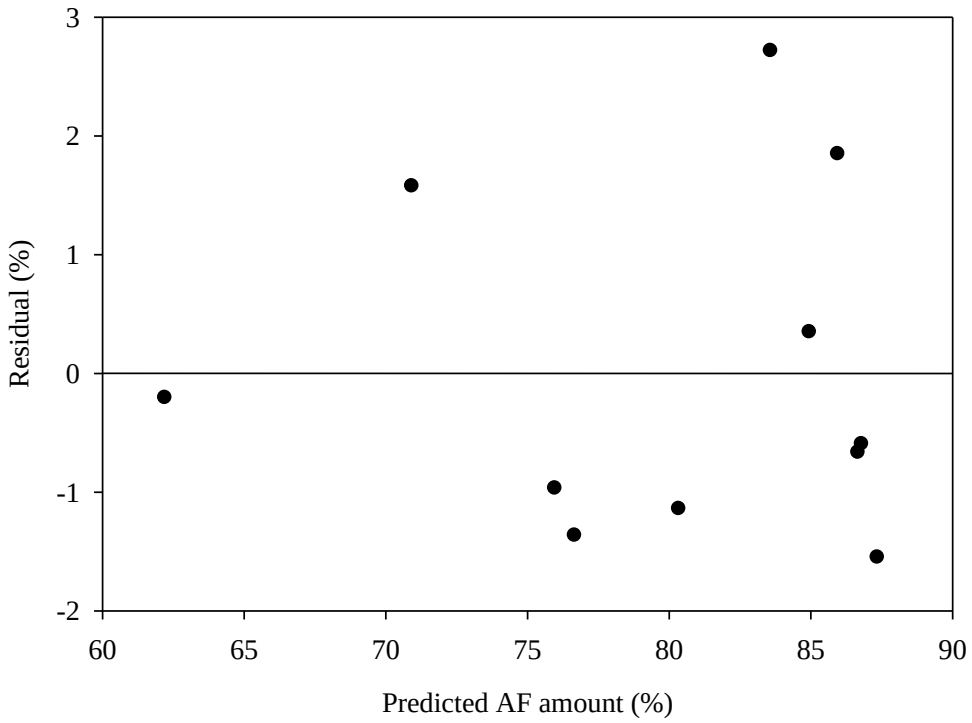

Figure 4.57. Plot of residuals for the model prediction without the outlier data for acicular ferrite (AF) in A709 steel weld metal.

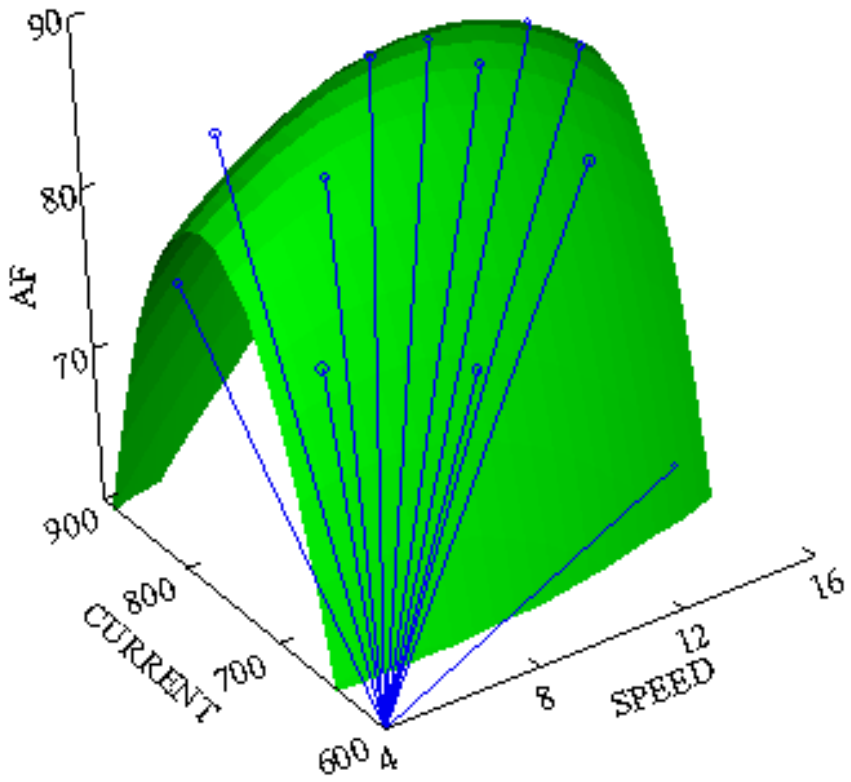

Figure 4.58. Combined effect of welding current and speed on acicular ferrite (AF) formation in the WM of A709 steel.

4.11.3 Model Predicting the Amount of Grain Boundary Ferrite Amount (GBF) in A709 Steel Weld Metal.

The model derived from regression analysis results which shows the relationship between grain boundary ferrite (GBF) formed in the WM of A709 steel and welding process parameters (current and speed) is shown in equation 4.3. Table B.4 in Appendix B shows the output of the regression analysis.

$$GBF = 386.67 - 1.02I + 5.61S - 0.01IS \quad (4.3)$$

The quadratic terms in both current (*I*) and speed (*S*) are absent from this expression compared to equation 3.3. The raw *R*-square and the corrected *R*-square values for GBF are 0.98 and 0.86, respectively. The tabulated *F*-statistic is 4.95 and the model *F*-statistic is 40.84. Since the calculated *F* value is greater than the tabulated *F*-value, the adequacy of the model is established The tabulated *t*-statistic value is 1.812..The predicted regression coefficients are all significant since their *t*-statistic values are more than 1.812. The residuals plot for the regression analysis is shown in Figure 4.59. There is a fairly good spread of data around the horizontal zero line. The interaction effect of welding current and speed on GBF formation in the WM of A709 steel is shown in Figure 4.60. The amount of GBF decreased to a minimum of ~ 5.5% at 800 A and 6.5 mm/s and subsequently increased with current. The amount of GBF obtained with Pax-it image analysis was 7.6% (see Figure 4.45).

4.11.4 Model Predicting the Amount of Widmanstatten Ferrite (WF) in A709 Steel Weld Metal.

Equation 4.4 is the regression model derived for the amount of Widmanstatten ferrite (WF) formed in the WM of A709 steel as current and speed were varied. Table B.5 in Appendix B shows the regression analysis results.

$$WF = 603.67 - 1.57I + 5.92S + 0.07S^2 - 0.01IS \quad (4.4)$$

where *I* and *S* retain their previous meanings.

The quadratic term in current (*I*) is absent from this expression compared to equation 3.3. The raw *R*-square and the corrected *R*-square values for WF are 1.00 and 0.97, respectively.

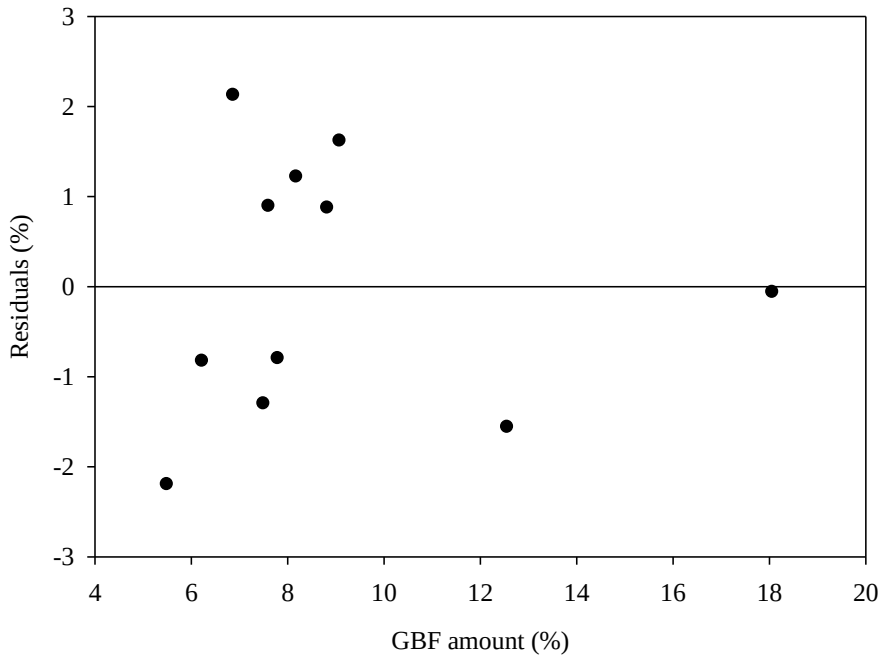

Figure 4.59. Plot of residuals for the model prediction for grain boundary ferrite (GBF) formation in the WM of A709 steel

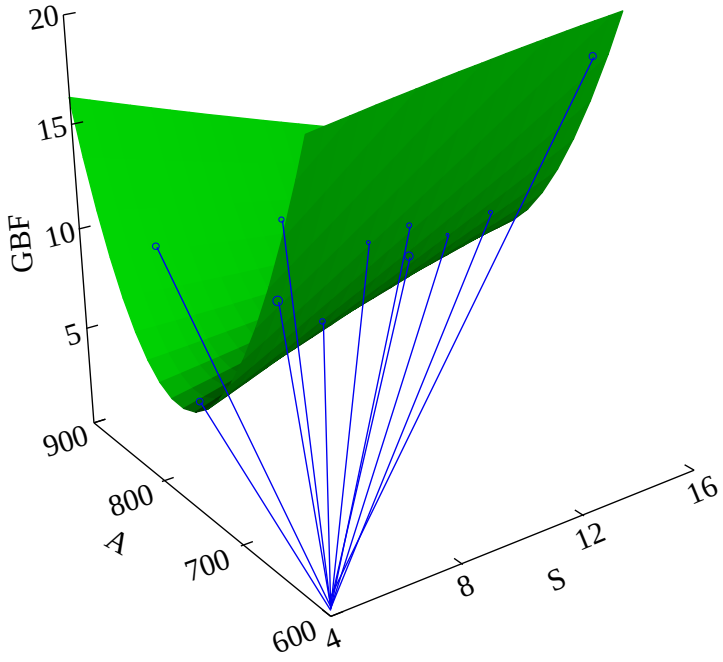

Figure 4.60. Combined effect of welding current and speed on GBF formation in the WM of A709 steel.

The tabulated *F*-statistic is 4.95 and the model *F*-statistic is 172.35. Since the calculated *F* value is greater than the tabulated *F*-value, the adequacy of the model is established. The tabulated *t*-statistic value is 1.812. Since the *t*-statistic values for the predicted regression coefficients are more than the tabulated value, it means they are all significant. The plot of residuals obtained from the regression analysis is shown in Figure 4.61. There is a fair spread of data around zero. The interaction effect of welding current and speed on WF formation in the WM of A709 steel is shown in Figure 4.62. The amount of WF decreased to a minimum of ~ 5.8% at 800 A and 11 mm/s and subsequently increased with current. The amount of WF in A709 steel weld metals obtained with Pax-it was 11.4% (see Figure 4.46).

4.11.5 Model Predicting the Amount of Acicular Ferrite (AF) in the WM of SA516 Steel.

The regression equation relating the amount of acicular ferrite (AF) produced in the WM of SA516 steel to the welding process variables (current and speed) is:

$$AF = -697.16 + 2.23I - 10.96S + 0.05S^2 + 0.01IS \quad (4.5)$$

where, *AF* is the amount of acicular ferrite (%), *I* is welding current (A) and S is the welding speed (mm/s).

The quadratic term in current (*I*) is absent compared to equation 3.3. The regression coefficients pertaining to equation (4.5) and the analysis of variance (ANOVA) for the model are presented in Table B.6 of Appendix B.

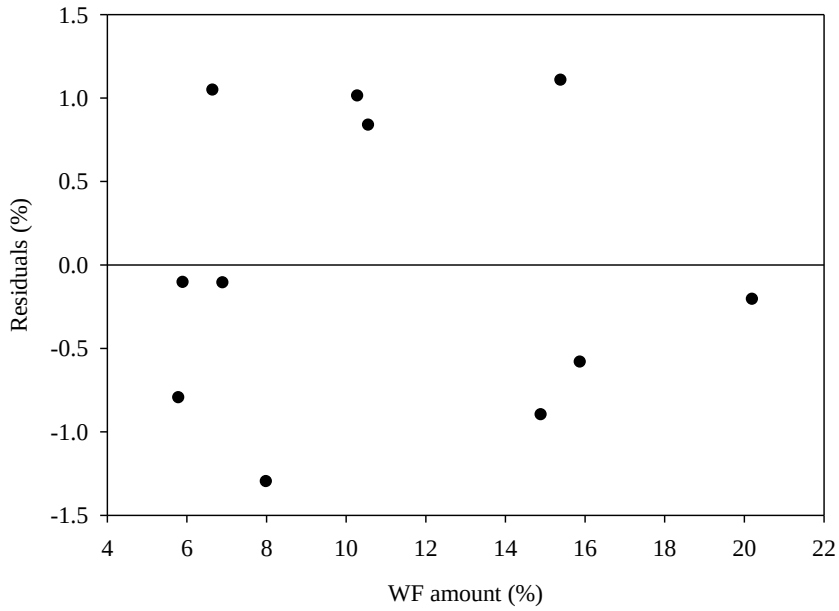

Figure 4.61. Plot of residuals for the model prediction for Widmanstatten ferrite (WF) formed in the WM of A709 steel.

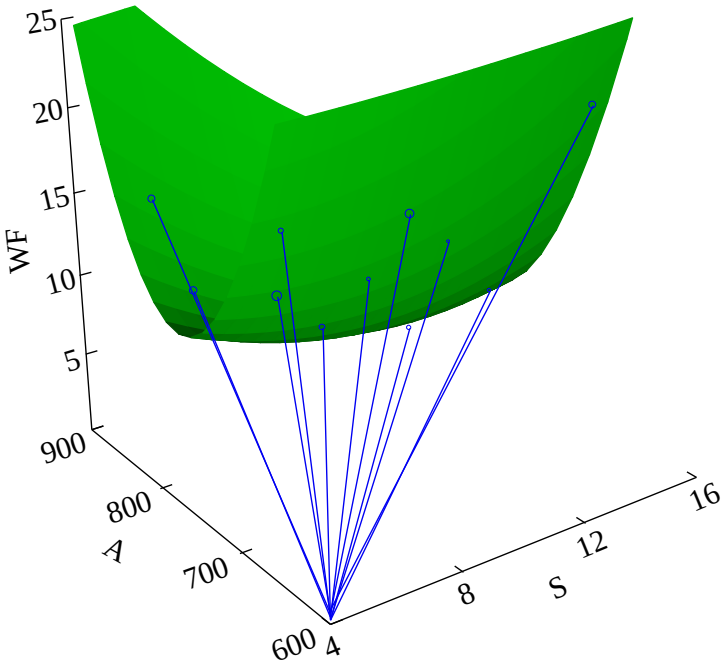

Figure 4.62. Combined effect of welding current and speed on Widmanstatten ferrite (WF) formed in the WM of A709 steel.

As in the case of A709 steel welds, the adequacy of the model was checked with the residuals obtained and tested by the ANOVA technique. The calculated *F*-statistic is 1627.15 at 95% confidence, while the tabulated *F*-statistic vale equals 4.28. The tabulated *t*-statistic for the 12 observations used in this study is 1.796.. The least *t*-statistic value obtained for the regression coefficients was for β_4 (t = 0.68), which is the quadratic term in welding speed. This means the term is non-significant. The raw *R*-squared value, which indicates the goodness of the fit, was 1.00 and the adjusted *R*-square (corrected) value was 0.90.

Figure 4.63 shows the plot of the residuals versus the model predictions. A close look at the residuals plot shows an outlier in the data for the test sample produced using 800 A and 9.3 mm/s which might be the source of the difference in the *R*-square values. Therefore, it was removed and the data re-analyzed using the same model. The model predictions and analysis of variance without the outlier data are shown in Table B.7 in Appendix B. The equation without the outlier is:

$$AF = -637.38 + 2.06I - 8.80S + 0.01S^2 + 0.01IS \qquad (4.6)$$

There is no quadratic relation term in current (*I*) is again absent in equation 4.6. The residuals plot for the data with the outlier removed is shown in Figure 4.64. The new regression model *F*-statistic is 3429.53 while the new tabulated *F*-statistic value is 4.95. Since the calculated *F* value is greater than the tabulated *F*-value, the adequacy of the model is established. The tabulated *t*-statistic value is 1.812.

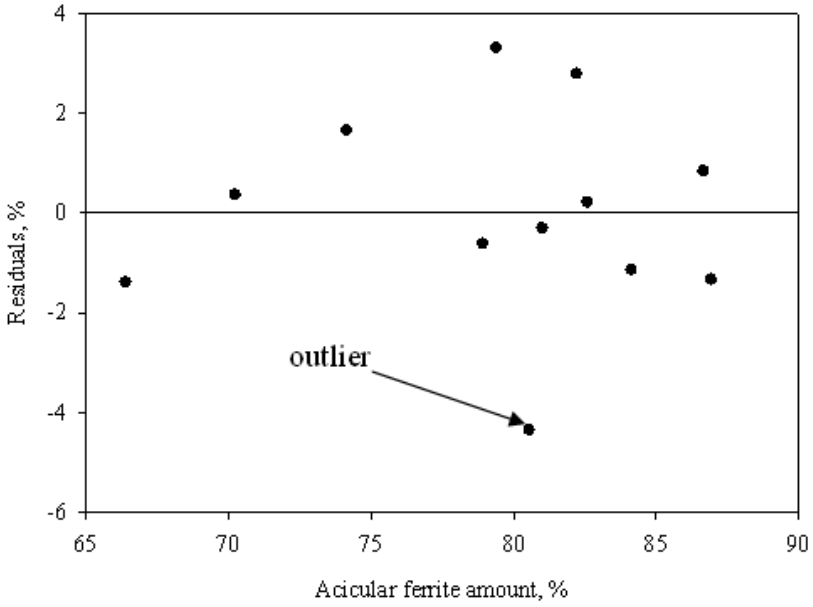

Figure 4.63. Plot of residuals for the model prediction for acicular ferrite (AF) formed in the WM of SA516 steel.

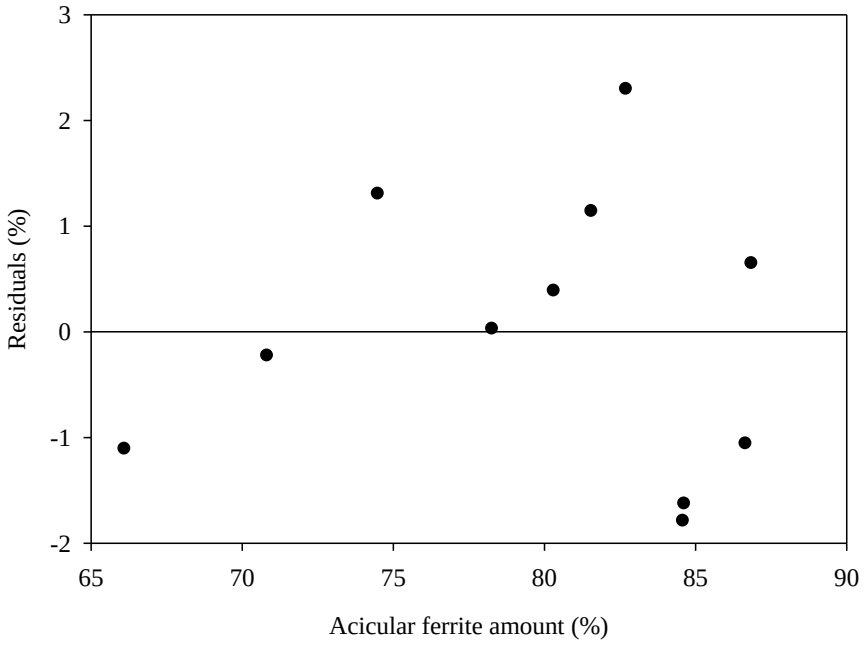

Figure 4.64. Plot of residuals for the model prediction without the outlier data for acicular ferrite (AF) produced in the WM of SA516 steel.

The *t*-statistic values for the regression coefficients (see Table B.7) are all significant with the exception of that of β_4 (t = 0.12), which is the quadratic term in welding speed. The raw *R*-square and corrected *R*-square values are 1.00 and 0.96, respectively. The residuals plot in Figure 4.64 shows the errors are fairly distributed around zero. The interaction effect of welding current and speed on AF is shown in Figure 4.65 indicating AF amount increased to a maximum of ~85% at 800 A and 12 mm/s The amount of AF that was determined in SA516 steel with Pax-it was 81%, which compares well with the regression analysis (see Figure 4.41).

4.11.6 Model Predicting the Amount of Grain Boundary Ferrite (GBF) in the WM of SA516 Steel.

The model derived from regression analysis results which shows the relationship between grain boundary ferrite (GBF) formed in the WM of SA516 steel and welding process parameters (current and speed) is shown in equation 4.7. Table B.8 in Appendix B shows the output of the regression analysis.

$$GBF = 211.12 - 0.63I + 4.89S + 0.02S^2 - 0.01IS \quad (4.7)$$

The quadratic term in current (*I*) is absent from this expression compared to equation 3.3. The raw R-square and the corrected R-square values for GBF are 0.96 and 0.84, respectively. The tabulated *F*-statistic value is 4.95 and the model *F*-statistic value is 21.76. The tabulated *t*-statistic value is 1.812. The *t*-statistic values for regression coefficients β_0, β_1 and β_4 (see Table B.8) are less than1.812. The residuals plot for the regression analysis is shown in Figure 4.66.

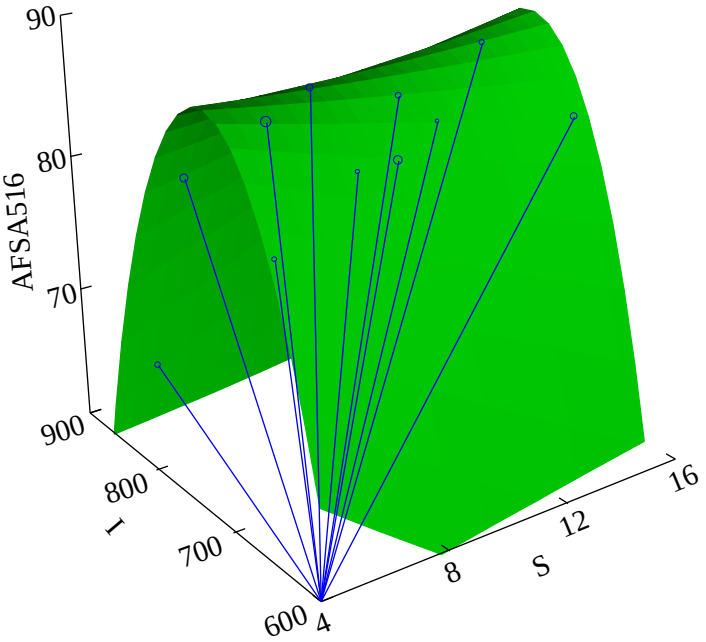

Figure 4.65. Combined effect of welding current and speed on acicular ferrite (AF) produced in the WM of SA516 steel.

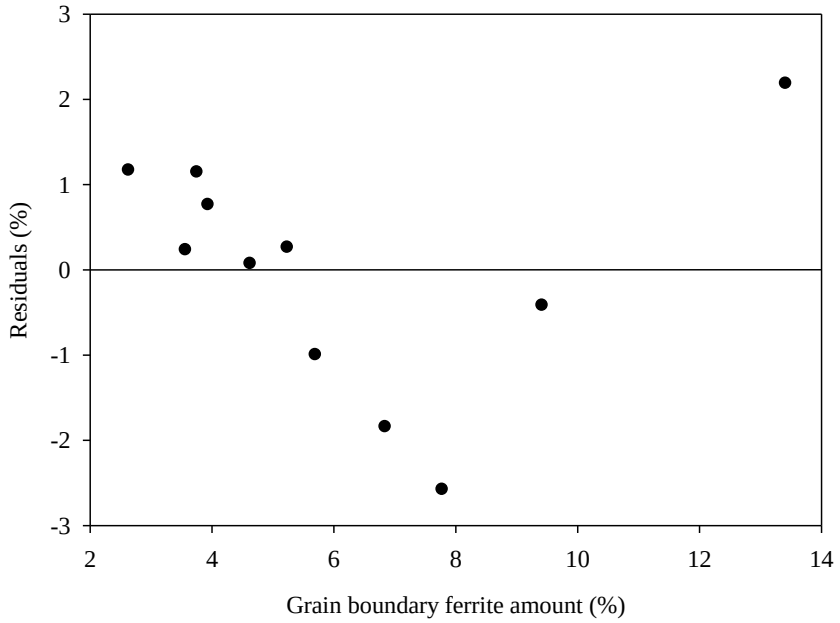

Figure 4.66. Plot of residuals for the model prediction without the outlier data for grain boundary ferrite (GBF) produced in the WM of SA516 steel.

There is a fairly good spread around the horizontal zero line. The interaction effect of welding current and speed on GBF formation in the WM of SA516 is shown in Figure 4.67. GBF amount decreased to a minimum at ~6% at 780 A and 8 mm/s and subsequently increased with current. The amount of GBF obtained in the WM of SA516 steel welds using Pax-it was 17% (see Figure 4.42).

4.11.7 Model Predicting the Amount of Widmanstatten Ferrite (WF) in the WM of SA516 Steel.

Equation 4.8 is the regression model derived for the amount of Widmanstatten ferrite (WF) formed in the WM of SA516 steel as current and speed were varied. Table B.9 in Appendix B shows the results of the regression analysis.

$$WF = 526.06 - 1.43I + 3.88S - 0.02S^2 - 0.01IS \qquad (4.8)$$

where I and S retain their previous meanings.

The raw R-square and the corrected R-square values for WF are 0.99 and 0.91, respectively. The tabulated F-statistic value is 4.95 and the F-statistic for the model is 127.56. Since the calculated F value is greater than the tabulated F-value, the adequacy of the model is established. The tabulated t-statistic value is 1.812. The t-statistic values for the regression coefficients (see Table B.9) are all greater than the critical value with the exception of that of β_4 the quadratic term in welding speed (t = 0.51). It is therefore non-significant. The plot of residuals obtained from the regression analysis is shown in Figure 4.68. There is an even spread of data around the horizontal zero line.

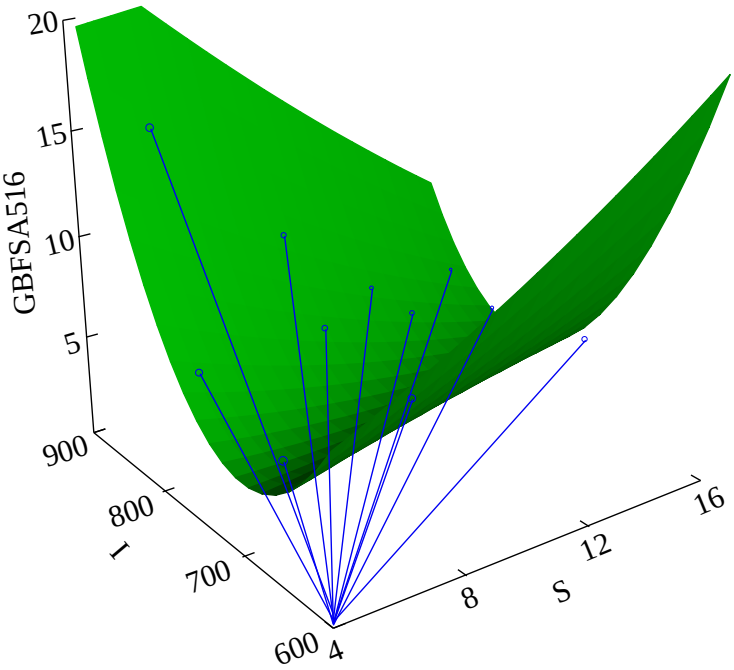

Figure 4.67. Combined effect of welding current and speed on grain boundary ferrite (GBF) produced in the WM of SA516 steel.

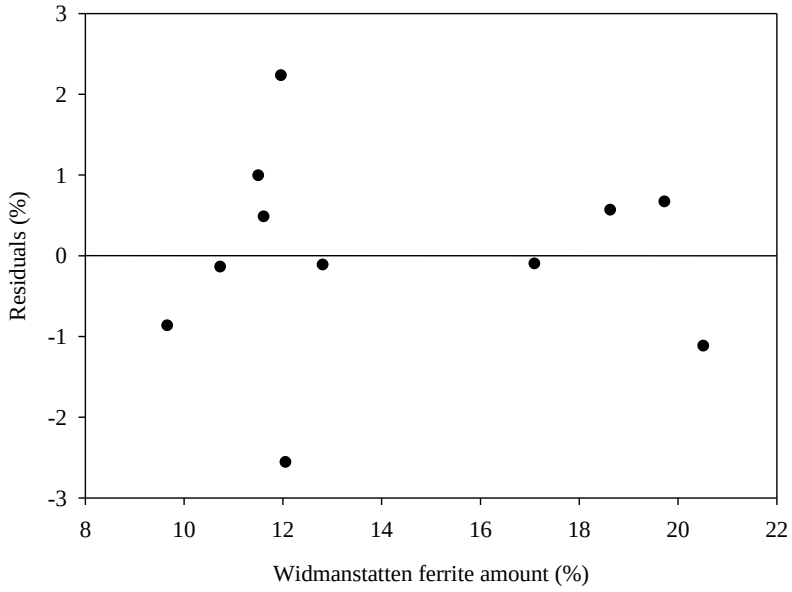

Figure 4.68. Plot of residuals for the model prediction without the outlier data for Widmanstatten ferrite (WF) produced in the WM of SA516 steel.

The interaction effect of welding current and speed on WF formed in the WM of SA516 steel is shown in Figure 4.69. The amount of WF decreased to a minimum of ~12 % at 780 A and 8 mm/s and subsequently increased with current. The amount of WF obtained in the WM of SA516 steel welds using Pax-it was 7% (see Figure 4.43).

4.12. Summary

It was mentioned in section 2.3 of Chapter 2 that welding current and speed influence the chemistry and the cooling rate of welded joints and, consequently, the final microstructure of welds. It was found in this study that carbon and oxygen contents of welded joints of SA516 and A709 steels were affected by welding current and speed. The carbon content of the weld metals of both steels decreased with increasing welding current. The oxygen content of the weld metals of both steels increased with welding current (increased heat input). For the welds of SA516 and A709 steels, the oxygen level in the weld metal for a given welding current generally decreased with increasing welding speed (decreasing heat input). Therefore, increasing heat input achieved by increasing welding current or by reducing welding speed increased the WM oxygen content.

The results also showed that the weld nugget area increased with increasing current and that high heat input produced large nugget area which is known to be detrimental to the mechanical properties of welded joints [24]. The weld cooling rate is a major factor that determines the microstructure of the weld joint. The results showed that the cooling rate parameter (NA/CI) increased with increasing heat input.

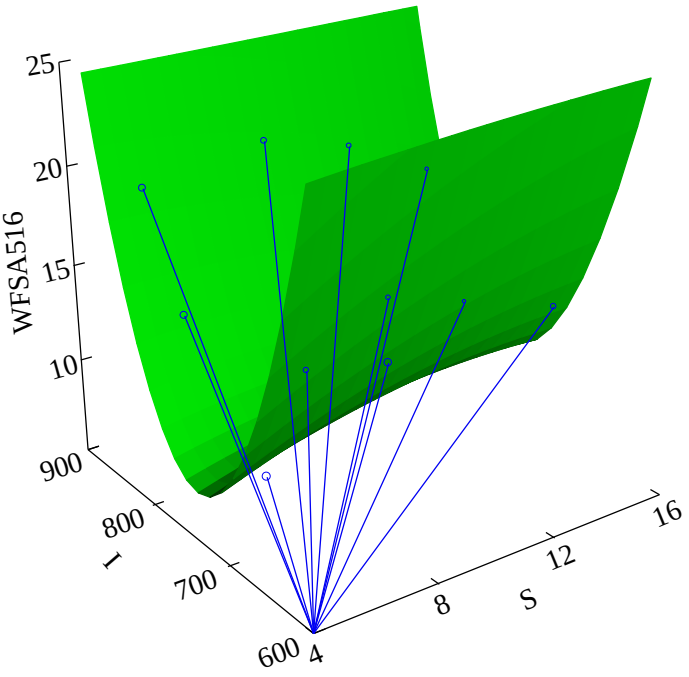

Figure 4.69. Combined effect of welding current and speed on Widmanstatten ferrite (WF) produced in the WM of SA516 steel.

As high value of NA/CI ratio translates to a high time constant ($\Delta t_{8/5}$) value, it implies that the weld will dwell for a longer period at higher temperatures. The HAZ microstructures of the welds of both steels consisted primarily of grain boundary ferrite (GBF), Widmanstatten ferrite (WF), pearlite (P) and bainite (B). On the average, the prior austenite grain size increased with increasing welding current but decreased with welding speed. The prior austenite grain size also increased with increasing heat input. The main microconstituents identified in the weld metals of SA516 and A709 steels were GBF, WF and AF. Quantitative metallographic analysis using PAX-it image analysis software showed that the weld metals consisted of approximately 76% AF, 17% GBF and 7% WF for SA516 steel and 81% AF, 7.6% GBF and 11.4% WF for A709 steel.

It was shown that the amount of AF in the weld metals of both steels increased with welding current from 700 to 800 A, but decreased as the current was further increased to 850 A.

To better understand the combined effect of welding current and welding speed on the microstructure, contour plots were generated. These plots showed the interaction effects of welding current and speed on the proportions of GBF, WF and AF. SEM and TEM inclusion morphology and composition analysis was done to determine inclusions that nucleate AF.

A non-linear quadratic regression model was fitted to the experimental data shown in Table B.2 of Appendix B using SYSTAT-11 statistical analysis software. Equations were obtained that express the proportion of weld metal ferrites (i.e., GBF, WF and AF) as functions of the welding current and speed for SA516 and A709 steel welds. There is agreement between the model predictions and the contour graphs obtained for the weld metal ferrites of both steels.

CHAPTER 5 CONCLUSIONS AND RECOMMENDATIONS

The effects of submerged arc welding current and welding speed on the microstructures of the weld metals and heat affected zones of SA516 and A709 steel welds were studied using optical microscopy, scanning electron microscopy, transmission electron microscopy and image analysis. Sizing of prior austenite grains and weld metal inclusions was carried out using image analysis. Chemical analysis of the inclusions was done using EDS. From the results presented and discussed in Chapter 4, the following conclusions can be made:

5.1 Conclusions

1. The weld metals of SA516 and A709 steels contained acicular ferrite in excess of 65 per cent.
2. X-ray diffraction did not reveal the presence of retained austenite in the weld metals of SA516 steel.
3. High heat input achieved by increasing welding current showed a more noticeable influence on the final microstructure of the weld metals compared to the results achieved by decreasing welding speed for the ranges studied. This was probably due to the fact that high current was accompanied by increased electrode melting which affected not only the cooling rate but also the weld metal chemistry.

4. There are two inclusion morphologies formed in the weld metals of both SA516 and A709 steels. They are the spherical and faceted inclusions. However, only spherical inclusions acted as nucleation sites for acicular ferrite formation.
5. Regression equations that relate the weld metal ferrites (GBF, WF and AF) to the welding parameters of current and speed were obtained for SA516 and A709 steel welds within the limits of the welding parameters studied. The equations can be useful in weld procedure development for the above steels and as a guide for other steels.

5.2 Statement of Originality and Contribution to Knowledge

1. This investigation related separately the effects of the welding current and welding speed on the microstructure and chemistry of the weld metals of SA516 grade 70 and A709 grade 50 steels. Published research work in the past that studied the effect of welding parameters on the microstructures of the HAZ and WM regions in steel weld joints combined the welding current and welding speed together as heat input. Though this approach was practical, the same heat input value achieved by different combinations of welding current and speed will give different weld metal microstructures.
2. Two types of inclusion morphologies were observed in the weld metals of both SA516 and A709 steels. They are the spherical and smooth inclusions and faceted inclusions. Acicular ferrite was found to nucleate only on the spherical inclusions.

5.3 Recommendations for Future Work

1. The WM oxygen content in principle should increase with increasing welding current and heat input. The results obtained in this study however did not establish a clear trend in the WM oxygen content in both SA516 and A709 steels. Other methods of determining the WM oxygen amount is recommended.
2. It is recommended that detailed SEM and TEM analysis be done on more of the weld metals of both SA516 and A709 steels. This will help to explain the difference between the round inclusions that nucleated AF form those that did not.
3. X-ray diffraction analysis was done on SA516 steel weld metal produced with 800 A and 9.3 mm/s. X-ray work is recommended for both SA516 and A709 steel welds for welding currents of 700 A and 850 A. This will help to fully determine the absence or presence of retained austenite in the weld metals.

References

1. K. Easterling, 1992, *Introduction to the Physical Metallurgy of Welding*, Butterworths-Heinemann Ltd, London.
2. The Procedure Handbook of Arc Welding, 1995, The Lincoln Electric Company, Cleveland, Ohio.
3. H. D. K. H. Bhadeshia, 1985, Structural Steels for the 1980s, Graduate Lecture, University of Cambridge, United Kingdom.
4. L. E. Svenson, 1999, "Consumables for Welding High Strength Steels", *Svetsaren*, Vol. 54 No. 1-2, pp. 29-33.
5. G. M. Evans and N. Bailey, 1999, *Metallurgy of Basic Weld Metal*, Abington Publishing, Cambridge, United Kingdom.
6. S. W. Thompson, D. J. Colvin and G. Kraus, 1996, "Austenite Decomposition During Continuous Cooling of an HSLA-80 Plate Steel", *Metallurgical and Materials Transactions*, Vol. 27A No. 6, pp.1557-1571.
7. R. W. K. Honeycombe and H. K. D. H. Bhadeshia, 1996, *Steels; Microstructure and Properties*, Second Edition, Metallurgy and Materials Science Series, Edward Arnold, London, Great Britain.
8. D. J. Abson and R. J. Pargeter, 1986, "Factors Influencing as-Deposited Strength, Microstructure and Toughness of Manual Metal Arc Welds Suitable for C-Mn Steel Fabrication", *International Metals Reviews*, Vol. 31 No. 4, pp. 141-194.
9. S. Liu and D. L. Olson, 1986, "Role of Inclusions in Controlling HSLA Steel Weld Microstructures", *The Welding Journal*, Vol. 2 No. 6, pp. 139s–149s.

10. A. R. Bhatti, M. E. Saggese, D. N. Hawkins, J. A. Whiteman and M. S. Golding, 1984, "Analysis Of Inclusions in Submerged Arc Welds in Microalloyed Steels", *Welding Journal*, Vol. 63 No. 7, pp. 224-230.
11. J. M. Dowling, J. M. Corbett and H. W. Kerr, 1986, "Inclusion Phases and the Nucleation of Acicular Ferrite in Submerged Arc Welds in High Strength Low Alloy Steels", *Metallurgical and Materials Transactions A*, Vol. 17 No. 9, pp. 1611-1623.
12. D. J. Abson, R. E. Dolby and P. H. M. Hart, 1978, "The Role of non-Metallic Inclusions in Ferrite Nucleation in Carbon Steel Weld Metals", *Proceedings of International Conference on Trends in Steels and Consumables for Welding*, The Welding Institute, London, England, pp. 75-89.
13. B. Basu and R. Raman, 2002, "Microstructural Variations in a High-Strength Structural Steel Weld under Isoheat Input Conditions", *Welding Journal,* Vol. 81 No. 11, pp. 239s-248s.
14. P. L. Harrison and R. A. Farrar, 1981, "Influence of Oxygen-Rich Inclusions on the γ-α Phase Transformation in High-Strength Low-Alloy (HSLA) Steel Weld Metals", *Journal of Materials Science*, Vol. 16, pp. 2218-2232.
15. *Selected ASTM Standards for Metallurgy Students*, 1965, American Society for Testing and Materials, Philadelphia, Pa.
16. ASM International, 2000, *Mechanical Testing and Evaluation*, in: ASM Handbook, Materials Park, Ohio, Vol. 8, pp. 596-604.
17. R. A. Farrar and P. L. Harrison, 1987, "Acicular Ferrite in Carbon-Manganese Weld Metals: An Overview", *Journal of Materials Science*, Vol. 22 No. 11, pp. 3812-3820.

18. S. Terashima and H. K. D. H. Bhadashia, 2007, "Changes in Toughness at Low Oxygen Concentrations in Steel Weld Metals", *Science and Technology of Welding and Joining*, Vol. 11, No. 5, pp. 509-516.

19. R. G. Pargeter, 1983, "Acicular ferrite and inclusions in C-Mn steel weld metals", *The Welding Institute Research Bulletin*, No. 24, pp. 215-220.

20. R. S. Funderburk, 1999, "Key Concepts in Welding Engineering", *Welding Innovation*, Vol. 16, No. 1, pp. 1-4.

21. SAW or Submerged Arc Welding, Welding Information, Updated Daily, www.weldguru.com/saw.html, (Accessed August, 2011).

22. J. Nowacki and P. Rybicki, 2005, "The Influence of Welding Heat Input on Submerged Arc Welded Duplex Steel Joints Imperfections", *Journal of Materials Processing Technology*, Vol. 164-165, pp. 1082-1088.

23. O. Grong and D. K. Matlock, 1987, "Microstructural Development in Mild Steel and Low-Alloy Steel Weld Metals", *International Metals Reviews*, Vol. 31 No 1, pp. 27-48.

24. C. S. Lee, R. S. Chandel and H. P. Seow, 2000, "Effect of Welding Parameters on the Size of Heat Affected Zone of Submerged Arc Welding", *Materials and Manufacturing Processes*, Vol. 15 No. 5, pp. 649-666.

25. Y. Kikuta, 1987, "Classification of Microstructures in Low C-Low Alloy Steel Weld Metal and Terminology", *Committee of Welding Metallurgy of Japan Welding Society*, Report No. IX-1281-83, Osaka, Japan.

26. J. R. Yang, 1987, "Development of Microstructure in High Strength Weld Deposits", Ph.D. Thesis, Trinity College, Cambridge, United Kingdom.

27. J. E. Indacochea, M. Blander and S. Shah, 1989, "Submerged Arc Welding: Evidence for Electrochemical Effects on the Weld Pool", *Welding Journal* (Miami Fla.), Vol. 68 No. 3, pp. 77-83.

28. S. D. Bhole and J. Billingham, 1983, "Effect of Heat Input on HAZ Toughness in HSLA Steels", *Metals Technology*, Vol. 10 No. 9, pp. 363-367.

29. C. A. Butler and C. E. Jackson, 1967, "Submerged Arc Welding Characteristics of the CaO-TiO_2-SiO_2 System", *Welding Journal*, (Miami Fla.), Vol. 46 No. 10, pp. 448-456.

30. R. S. Chandel and S. R. Bala, 1986, "Effect of Welding Parameters and Groove Angle on the Soundness of Beads Deposited by the SAW Process", *Proceedings of an International Conference on Trends in Welding Research*, ASM International, New York, USA, pp. 379-385.

31. P. Kanjilal, S. K. Majumdar and T. K. Par, 2005, "Prediction of Acicular Ferrite from Flux Ingredients in Submerged Arc Weld Metal of C-Mn Steel", *ISIJ International*, Vol. 45 No. 6, pp. 876-885.

32. T. H. North, 1977, "The Distribution of Manganese between Slag and Metal During Submerged Arc Welding", *Welding Research Abroad*, The Welding Institute, London, pp. 2-15.

33. H. K. D. H. Bhadeshia, 1999, "Some Phase Transformations in Steel", *Materials Science and Technology*, Vol. 15 pp. 22–29.

34. J. Jang and J. E. Indacochea, 1987, "Inclusion Effects on Submerged-Arc Weld Microstructure", *Journal of Materials Science*, Vol. 22 No. 2, pp. 689-700.

35. S. S. Tuliani, T. Boniszewski and N. F. Eaton, 1969, "Notch Toughness of Commercial Submerged-Arc Weld Metal", *Welding and Metal Fabrication*, Vol. 37 No. 8, pp. 327-339.

36. Y. Ito, M. Nakanishi and Y. Komizo, 1982, "Effects of Oxygen on Low Carbon Steel Weld", *Metal Construction*, Vol. 14 No. 9, pp. 472-478.

37. E. S. Kayali, J. M. Corbett and H. W. Kerr, 1983, "Observations on Inclusions and Acicular Ferrite Nucleation in Submerged Arc HSLA Welds", *Journal of Materials Science Letters*, Vol. No. 3, 2, pp. 123-128.

38. C. E. Jackson, 1982, Submerged Arc Welding, Fluxes and Relations Among Process Variables, in: Metals Hand Book, ASM, Metals Park, OH, pp.73-77.

39. H. K. D. H. Bhadeshia and L., E. Svensson, 1993, "Modelling the Evolution of Microstructure in Steel Weld Metal", *Journal of Materials Science*, London, pp. 109–182.

40. G. M. Evans, 1996, "Microstructure and Properties of Ferritic Steel Welds Containing Ti and B", *Welding Journal* (Miami Fla.), Vol. 75 No.8, pp. 251-260.

41. W. Yan, Y. Y. Shan and K. Yang, 2006, "Effect of TiN Inclusions on the Impact Toughness of Low-Carbon Microalloyed Steels", *Metallurgical and Materials Transactions A*, Vol. 37A, No. 7, pp. 2147-2157.

42. S. S. Babu, 1999, "Fundamental Understanding of Inclusion Formation and Microstructural Evolution in Low-Alloy Steel Welds", Invited Talk at Nippon Steel Corporation, Futtsu, Japan.

43. A. Butler and C. E. Jackson, 1967, "Submerged Arc Welding Characteristics of the CaO-TiO_2-SiO_2 System", *Welding Journal*, (Miami Fla.), Vol. 46 No. 10, pp. 448-456.

44. L. Devillers, D. Keplan, B. Marandet, A. Ribes and P. V. Ribond, 1983, "The Effect of Low Level of Some Elements on the Toughness of Submerged- Arc Welded CMn Steel Welds" *Proceedings, The Effects of Residual, Impurity and Micro-Alloying Elements on Weldability and Weld Properties*, The Welding Institute, London, Paper 1.

45. Carbon Equivalent, http://www.leonghuat.com/articles/carbon%20equivalent.htm, [Accessed on August, 2011).

46. R. D. Thomas, 1977, "Submerged-Arc Welding of HSLA Steel for Low-Temperature Services", *Metal Progress*, Vol. 111 No. 4, pp. 30-36.

47. N. A. Fleck, O. Grong, G. R. Edwards and D. R. Matlock, 1992, "The Role of Filler Metal Wire and Flux Composition in Submerged Arc Weld Metal Transformation Kinetica", *Welding Journal*, Vol. 65, No. 5, pp. 113s-121s.

48. K. Prasad and D. K. Dwivedi, 2008, "Some Investigations on Microstructure and Mechanical Properties of Submerged Arc Welded HSLA Steel Joints", *The International Journal of Advanced Manufacturing Technology*, Vol. 36, pp. 475-483.

49. R. A. Farrar, Z. Zhang, S. R. Bannister and G. S. Barrite, 1993, "The Effect of Prior Austenite Grain Size on the Transformation Behaviour of C-Mn- Ni Weld Metal", *Journal of Materials Science*, Vol. 28, No. 5, pp. 1385-1390.

50. L. E. Collins, M. J. Godden and J. D. Boyd, 1983, "Microstructures in Linepipe Steels", *Canadian Metallurgical Quarterly*, Vol. 2 No. 22, pp 169-179.

51. S. Kou, 1987, Welding Metallurgy, John Wiley & Sons, New York.

52. H. K. D. H. Bhadeshia, 1990, "Control of Weld Metal Microstructure and Properties", in: *The Metallurgy, Welding and Qualification of Microalloyed*

(HSLA) Steel Weldments, eds. J. T. Hickney, D. G. Howden and M. D. Randall, American Welding Society, November, pp. 34-69.

53. J. H. Tweed and F. F. Knott, 1987, "Micromechanisms of Failure in C-Mn Weld Metals", *Acta Metallurgica*, Vol. 35 No. 7, pp. 1401-1414.
54. J. A. Brooks and M. I. Baskes, 1986, *Advances in Welding Science and Technology*, ed. S.A. David, ASM International, Materials Park, OH.
55. R. A. Ricks, P. R. Howell and G. S. Barritte, 1982, "The Nature of Acicular Ferrite in HSLA Steel Weld Metals", *Journal of Materials Science*, Vol. 17 No. 3, pp. 732-740.
56. S. Babu, 1991, "Acicular Ferrite and Bainite in Fe-Cr-C Weld Deposits", Ph.D. Thesis, University of Cambridge, England.
57. R. C. Cochrane and P. R. Kirkwood, 1978, "The Effects of Oxygen on Weld Metal Microstructure", *Proceedings of the Welding Institute Conference on Trends in Steels and Consumables for Welding*, London, pp. 75-103.
58. R. C. Cochrane, 1982, Weld Metal Microstructures, *International Institute of Welding*, Doc. IX-1248-82.
59. G. L. F. Powell and G. Herfurth, 1998, "Charpy V-Notch Properties and Microstructures of Narrow Gap Ferritic Welds of a Quenched and Tempered Steel Plate", *Metallurgical and Materials Transactions A: Physical Metallurgy and Materials Science*, Vol. 29A No. 11, pp. 2775–84.
60. G. Thewlis, 1994, "Transformation Kinetics of Ferrous Weld Metal", *Materials Science and Technology*, Vol. 2, No. 10, pp. 110-125.

61. A. Ahlblom, U. Bergstrom, N. E. Hannerz and I. Werlefors, 1983, "Effect of Residual, Impurity and Micro-Alloying Elements on Weldability and Weld Properties", *Proceedings of the Welding Institute Conference,* London, pp. 49-64.

62. D. Rosenthal, 1946, "The Theory of Moving Sources of Heat and its Application to Metal Treatments", *Transactions ASME Journal of Heat Transfer*, Vol. 68, pp. 849- 865.

63. C. D. Lundin, G. Zhou and K. K. Khan, 1995, "Metallurgical Characterization of the HAZ in A516-70 and Evaluation of Fracture Toughness Specimens", *Welding Research Council Bulletin*, No. 403, Report 1. pp. 1-88.

64. N. T. Nguyen, 2003, *Thermal Analysis of Welds*, Ashurst, Southampton, United Kingdom.

65. F. B. Pickering, 1978, *Physical Metallurgy and the Design of Steels, Applied* Science Publishers LTD, London.

66. P. E. McDonald, 1985, "Factors Influencing the Microstructure and Mechanical Properties of Ultra Low Carbon Bainitic 100 Tungsten Inert Gas Multipass Weldments", Ph.D. Thesis, University of Utah, USA.

67. K. E. Dorshu and R. D. Stout, 1961, "The Factors Affecting the Notch Toughness Steel Welds", *Welding Journal*, Vol. 40, No. 3, pp. 97s- 105s.

68. D. R. Askeland, 1984, *The Science and Engineering of Materials,* PWS Publishing Company, Monterey, Califonia, USA, pp. 296.

69. D. D. Crockett, J. A. Rhone, R. F. Young and D. C. Noernberg, 1995, "Design Considerations for Submerged Arc Consumables Intended for the Manufacture of Line Pipe", *Pipeline Technology*, Vol. 1, No.3, pp. 151-162.

70. R. A. Moll and R. D. Stout, 1967, “Composition Effects in Iron-Base Weld Metal”, *Welding Journal*, Vol. 46 No. 12, pp. 551s- 561s.

71. G. S. Chaveriat, G. S. Kim, S. Shah and J. E. Indacochea, 1987, “Low Carbon Steel Weld Microstructures: The Role of Oxygen and Manganese”, *Journal of Materials Engineering*, Vol. 9 No. 3, pp. 253-267.

72. M. Lord, 1999, “Design and Modelling of Ultra-High Strength Steel Weld Deposits”, Ph.D. Thesis, University of Cambridge, United Kingdom.

73. B. M. Patchett, J. E. Bringas, 1998, CASTI Metals Blue Book – Welding Filler Metals, CASTI Publishing Inc. and AWS, Edmonton, AB, Canada.

74. G. M. Evans, 1991, “The Effect of Nickel on Microstructure and Properties of C–Mn All-Weld Metal Deposits”, *Welding Research Abroad*, Vol. 37 No. 41, pp. 70–83.

75. J. C. F. Jorge, L. F. G. Souza, J. M. A. Rebello and G. M. Evans, 1992, “Effect of Chromium on the Mechanical Properties of Mn-Mo Weld Metal Deposits”, *Materials Characterization*, Vol. 47, No. 3-4, pp. 195-205.

76. S. Lampman, 1997, Weld Integrity and Performance, A Source Book Adapted from ASM International, Materials Park, OH, pp. 89-92.

77. L. E. Svensson, 1994, Control of Microstructure and Properties in Steel Arc Welds, CRC Press, Inc., Sweden, pp.11-17.

78. V. B. Trindade, L. G. Souza and R. R. Paranhos, 2007, “The Role of Addition of Ni on the Microstructure and Mechanical Behaviour of C-Mn Weld Metals”, *Exacta*, Vol. 5 No. 1, pp. 177-183.

79. N. Bailey, 1983, “Titanium Flux Additions During Submerged Arc Welding of Ferritic Steels”, Welding Institute Report No. 221, pp. 1-22.

80. S. S. Babu, G. M. Goodwin, R. J. Rohde and B. Sielen, 1997, "Effect of Residual Boron on the Microstructure of Low-Carbon Steel Resistance-Seam Welds", *Materials Science and Technology*, Vol. 11, No.6, pp. 186-193.

81. D. W. Oh, D. L. Olson and R. H. Frost, 1994, "The Influence of Zirconium and Boron on Low Carbon Steel Weld Microstructure", *Journal of Engineering for Industry, Transactions of the ASME*, Vol. 116, pp.26-31.

82. P. T. Oldland, C. W. Ramsay, D. K. Matlock and D. L. Olson, 1989, "Significant Features of High-Strength Steel Weld Metal Microstructures", *Welding Journal*, Vol. 58 No. 4, pp. 158s-169s.

83. C. S. Chai and T. W. Eager, 1980, "The Effect of SAW Parameters on Weld Metal Chemistry", *Welding Journal*, Vol. 59 No. 3, pp. 93s-98s.

84. H. Terashima and P. H. M. Hart, 1983, "Effect of Residual Impurity and Microalloying Elements on Weldability and Weld Properties", *The Welding Institute Research Report*, Paper 27, London.

85. Y. Ito and M. Nakanishi, 1975, "Submerged Arc Welding Method and Flux Cored Wire for Use in Same", Patent Number 3868487, USA.

86. K. Beomjoo, U. Sangho, L. Changhee, L. Jongbong and A. Youngho, 2005, "Effects of Inclusions and Microstructures on Impact Energy of High Heat-Input Submerged-Arc-Weld Metals", *Journal of Engineering Materials and Technology*, Vol. 127, N. 2, pp. 204-213.

87. M. Diaz, I. Madariaga, J. M. Rodriguez-Ibabe and I. Gutierrez, 1998, "Improvement of Mechanical Properties in Structural Steels by Development of Acicular Ferrite Microstructures", *Journal of Steel Construction Research*, Vol. 46, No.7, pp. 413-414.

88. M. R. Blicharski, C. I. Garcia, S. Pytel and A. J. DeArdo, 1988, "Structure and Properties of ULCB Plate Steels for Heavy Section Applications", *Processing, Microstructure and Properties of HSLA Steels*, The Minerals, Metals, and Materials Society, New York, USA.

89. T. W. Eager, 1978, "Source of Weld Metal Oxygen Contamination During Submerged Arc Welding", *Welding Journal*, Vol. 57 No. 3, pp. 76s-80s.

90. J. R. Yang and H. K. D. H. Bhadeshia, 1991, "Acicular Ferrite Transformation in Alloy-Steel Weld Metals", *Journal of Materials Science,* Vol. 26 No. 3, pp. 839-845.

91. National Board Inspection Code NBIC RA-2151-I, 2007, The National Board of Boilers and Pressure Vessel Inspectors, Columbus, Ohio, USA.

92. Annual Book of ASTM Standards, 1997, Metals Test Methods and Analytical, Section 3, Vol. 3.01, ASTM, Easton, USA, pp. A370-373.

93. Mineral Powder Diffraction File, 1980, Joint Committee on Power Diffraction Standards, International Centre for Diffraction Data, Pa., U. S. A.

94. G. E. P. Box, L. R. Connor, W. R. Cousins, O. L. Davies, F. R. Himsworth and G. P. Sillitto, 1978, *The Design and Analysis of Industrial Experiments*, The Chaucer Press, Bungay, Suffolk.

95. J. N. Neter, W. Wasserman and M. H. Kutner, 1983, *Applied Linear Regression Models*, Richard D. Irwin Inc., Homewood, pp. 303-312.

96. V. Parashar, A. Rehman, J. L. Bhagoria and Y. M. Puri, 2010, "Statistical and Regression Analysis of Material Removal Rate for Wire Cut Electro Discharge Machining of SS 304L Using Design of Experiments", *International Journal of Engineering Science and Technology*, Vol. 2 No. 5, pp. 1021-1028.

97. Y. Yang, 2008, “The Effect of Submerged Arc Welding Parameters on the Properties of Pressure Vessel and Wind Turbine Tower Steels”, MSc. Thesis, University of Saskatchewan, Saskatoon, Canada.

98. V. Gunaraj and N. Murugan, 2002, “Prediction of Heat-Affected Zone Characteristics in Submerged Arc Welding of Structural Steel Pipes”, *Welding Journal*, Vol. 5, No.3, pp 94s-105s.

99. D. M. Viano, N. U. Ahmed and G. O. Schumnn, 2000, “Influence of Heat Input and Travel Speed on the Microstructure and Mechanical Properties of Tandem Submerged Arc HSLA Steel Weldments”, *Science and Technology of Weld Joints*, Vol. 5 No. 1, pp. 26-34.

100. C. Daniel and F. Wood, 1971, *Fitting Equations to Data; Computer Analysis of Multifactor Data for Scientists and Engineers*, John Willey and Sons, Inc., New York.

APPENDIX. A

STATISTICAL ANALYSIS

A.1 Equations for Model Evaluation

The standard error (Se) of the estimates is given as [95]:

$$S_e = \frac{\sum (y_i - \bar{y}_i)}{(n - p - 1)}^{1/2} \quad \text{(A.1)}$$

where y_i = the sample value of the dependent variable, $\bar{y}_i$ = corresponding value estimated from the regression equation, n = number of observations and p = the number of independent variables.

The sum of squares due to error (SSE) in Table 3.5:

$$SSE = \sum_{i}^{n} \left(y_i - \bar{y}\right) \quad \text{(A.2)}$$

where $\bar{y}$ is the mean of the y_i values. The sum of squares due to regression (SSR) in Table 3.5:

$$SSR = \sum_{i}^{n} \left(\bar{y}_i - \bar{y}\right)^2 \quad \text{(A.3)}$$

The total sum of squares (SST) is:

$$SST = SSE + SSR \quad \text{(A.4)}$$

The parameter R^2 is called the coefficient of multiple determination, represents the proportion of the total variation in *y* obtained from the regression model. It is given as:

$$R^2 = \frac{SSE}{SST} \tag{A.5}$$

The adjusted fit $\overline{R}^2$adjusted is given as:

$$\overline{R}^2 = 1 - \frac{SSE/(n-p-1)}{SST/(n-1)} \tag{A.6}$$

The overall goodness of fit of a model to determine whether it correctly predicts the dependent values is evaluated using the F test. The F-statistic is calculated as (refer to Table 3.5):

$$F = \frac{SSE/(n-p-1)}{SST/(n-1)} = \frac{MSR}{MSE} \tag{A.7}$$

where MSR is the mean sum of regression and MSE is the mean sum of error.

APPENDIX B

B.1 Regression Analysis

Tables B.1 and B.2 contain the calculated SAW process heat input and measured values of the prior austenite grain width and the various ferrites for SA516 and A709 steel welds. These values have been used in various graphs and analyses discussed in Chapter 4.

Table B.1. Prior austenite grain width in the weld metals of SA516 and A709 steels.

Weld No.	Welding Current (A)	Welding speed (mm/s)	Heat input (kJ/mm)	γ SA516 (μm).	γ A709 (μm).
1	700	5.3	4.39	140	147
2	700	9.3	2.50	101	110
3	700	12.3	1.89	75	107
4	700	15.3	1.52	60	86
5	800	5.3	5.02	173	182
6	800	9.3	2.86	111	135
7	800	12.3	2.16	98	116
8	800	15.3	1.74	84	96
9	850	5.3	5.33	185	183
10	850	9.3	3.04	132	161
11	850	12.3	2.30	106	127
12	850	15.3	1.85	89	108

Table B.2. Proportions of ferrites found in the weld metals of SA 516 and A709 steels.

Current A	Speed mm/s	GBF %	WF %	AF %	GBF %	WF %	AF %
		SA516 (PV)			A709 (WT)		
700	5.3	3.8	8.8	87.5	10.7	14.0	75.3
700	9.3	4.7	12.5	82.8	11.0	16.5	72.5
700	12.3	8.8	15.0	76.2	6.5	10.5	83.0
700	15.3	4.7	12.7	82.7	18.0	20.0	62.0
800	5.3	5.2	14.2	80.7	3.3	11.3	85.3
800	9.3	5.5	9.5	85.0	5.4	6.8	87.8
800	12.3	4.9	12.1	83.0	9.0	5.0	86.0
800	15.3	3.8	10.6	85.6	8.5	5.8	85.8
850	5.3	15.6	19.4	65.0	9.7	15.3	75.0
850	9.3	9.0	20.4	70.6	9.4	11.4	79.2
850	12.3	5.0	19.2	75.8	7.0	6.7	86.3
850	15.3	4.7	17.0	78.3	6.2	7.7	86.2

B.2 Model Predictions and analysis

The regression coefficients used in equation (4.1) and analysis of variance for the model and R-square values are presented in Tables B.3 to B9.

Table B.3. Model estimates for acicular ferrite (AF) produced in the WM of A709 steel: (a) regression coefficients, (b) analysis of variance and (c) R-square values.

(a) Regression coefficients

Regression Coefficients	Estimated Regression Coefficients(ERC)	Asymptotic Standard Error (ASE)	ERC/ASE (t*)	Confidence Interval < 95%>	
				Lower	Upper
βo	-752.93	392.93	-1.91	1713.83	209.11
β_1	2.20	1.02	2.17	-0.28	4.69
β_2	-6.69	5.87	-1.14	-21.06	7.67
β_3	-0.00	0.00	-2.24	-0.00	0.00
β_4	-0.17	0.13	-1.25	-0.50	0.16
β_5	0.01	0.01	1.99	-0.00	0.03

(b) Analysis of variance

Source of variable	Sum of squares	Degree of freedom	Mean square	F statistic model	F statistic tabulated
Regression	78011.09	6	13001.85	468.37	4.28
Error	166.59	6	27.76		
Total	78177.68	12			

(c) R-square

Raw R-square (1-Residual/Total)	1.00
Mean corrected R-square (1-Residual/Corrected)	0.75
R(observed vs predicted) square	0.75

Table B.4. Model estimates for grain boundary ferrite (GBF) produced in the WM of A709 steel: (a) regression coefficients, (b) analysis of variance and (c) R-square values.

(a) Regression coefficients

Regression Coefficients	Estimated Regression Coefficients(ERC)	Asymptotic Standard Error (ASE)	ERC/ASE (t*)	Confidence Interval < 95%>	
				Lower	Upper
β_0	386.67	152.47	2.54	-5.27	78.61
β_1	-1.02	0.40	-2.59	-2.04	-0.01
β_2	5.61	2.39	2.35	-0.54	11.76
β_3	0.00	0.00	2.67	0.00	0.00
β_4	0.00	0.05	0.09	-0.13	0.14
β_5	-0.01	0.00	-2.65	-0.01	-0.00

(b) Analysis of variance

Source of variable	Sum of squares	Degree of freedom	Mean square	F statistic model	F statistic tabulated
Regression	1002.22	6	167.04	40.84	4.95
Error	20.46	5	4.09		
Total	1022.68	11			

(c)R-square

Raw R-square (1-Residual/Total)	0.98
Mean corrected R-square (1-Residual/Corrected)	0.86
R(observed vs predicted) square	0.86

Table B.5. Model estimates for Widmanstatten ferrite (WF) produced in the WM of A709 steel: (a) regression coefficients, (b) analysis of variance and (c) R-square values.

(a) Regression coefficients

Regression Coefficients	Estimated Regression Coefficients(ERC)	Asymptotic Standard Error (ASE)	ERC/ASE (t*)	Confidence Interval < 95%>	
				Lower	Upper
β_0	603.67	92.75	6.51	365.24	842.11
β_1	-1.57	0.24	-6.55	-2.19	-0.96
β_2	5.92	1.46	4.07	2.18	9.66
β_3	0.00	0.00	6.77	0.00	0.00
β_4	0.07	0.03	2.06	-0.02	0.15
β_5	-0.01	0.00	-6.14	-0.01	-0.01

(b) Analysis of variance

Source of variable	Sum of squares	Degree of freedom	Mean square	F statistic model	F statistic tabulated
Regression	1561.48	6	260.25	172.35	4.95
Error	7.57	5	1.51		
Total	1569.05	11			

(c) R-square

Raw R-square (1-Residual/Total)	1.00
Mean corrected R-square (1-Residual/Corrected)	0.97
R(observed vs predicted) square	0.97

Table B.6. Model estimates for acicular ferrite (AF) produced in the WM of SA516 steel: (a) regression coefficients, (b) analysis of variance and (c) R-square values.

(a) Regression coefficients

Regression Coefficients	Estimated Regression Coefficients(ERC)	Asymptotic Standard Error (ASE)	ERC/ASE (t*)	Confidence Interval < 95%>	
				Lower	Upper
β_0	-697.16	208.23	-3.35	-1206.67	-187.65
β_1	2.23	0.54	4.14	0.91	3.55
β_2	-10.96	3.11	-3.53	-18.58	-3.35
β_3	0.00	0.00	-4.51	-0.00	-0.00
β_4	0.05	0.07	0.68	-0.13	0.22
β_5	0.01	0.00	3.78	0.00	0.02

(b) Analysis of variance

Source of variable	Sum of squares	Degree of freedom	Mean square	F statistic model	F statistic tabulated
Regression	76150.78	6	12691.80	1627.15	4.28
Error	46.78	6	7.80		
Total	76197.56	12			

(c) R-square

Raw R-square (1-Residual/Total)	1.00
Mean corrected R-square (1-Residual/Corrected)	0.90
R(observed vs predicted) square	0.90

Table B.7. Model estimates without the outlier data for acicular ferrite (AF) formed in the WM of SA516.

(a) Regression coefficients

Regression Coefficients	Estimated Regression Coefficients(ERC)	Asymptotic Standard Error (ASE)	ERC/ASE (t*)	Confidence Interval < 95%>	
				Lower	Upper
β_0	-637.38	139.34	-4.57	-995.56	-279.20
β_1	2.06	0.36	5.70	1.13	2.99
β_2	-8.80	2.19	-4.03	-14.42	-3.18
β_3	-0.00	0.00	-6.24	-0.00	-0.00
β_4	0.01	0.05	0.12	-0.12	0.13
β_5	0.01	0.00	4.91	0.01	0.02

(b) Analysis of variance

Source of variable	Sum of squares	Degree of freedom	Mean square	F statistic model	F statistic tabulated
Regression	70374.03	6	11729.01	3429.53	4.95
Error	17.09	5	3.42		
Total	70391.12	11			

(c) R-square

Raw R-square (1-Residual/Total)	1.00
Mean corrected R-square (1-Residual/Corrected)	0.96
R(observed vs predicted) square	0.96

Table B.8. Model estimates without the outlier data for grain boundary ferrite (GBF) formed in the WM of SA516 steel.

(a) Regression coefficients

Regression Coefficients	Estimated Regression Coefficients(ERC)	Asymptotic Standard Error (ASE)	ERC/ASE (t*)	Confidence Interval < 95%>	
				Lower	Upper
β_0	211.12	148.39	1.42	-170.33	592.57
β_1	-0.63	0.38	-1.62	-1.61	0.36
β_2	4.89	2.33	2.10	-1.09	10.88
β_3	0.00	0.00	1.89	-0.00	0.00
β_4	0.02	0.05	0.38	-0.12	0.16
β_5	-0.01	0.00	-2.88	-0.01	-0.00

(b) Analysis of variance

Source of variable	Sum of squares	Degree of freedom	Mean square	F statistic model	F statistic tabulated
Regression	506.43	6	84.41	21.76	4.95
Error	19.38	5	3.88		
Total	525.81	11			

(c) R-square

Raw R-square (1-Residual/Total)	0.96
Mean corrected R-square (1-Residual/Corrected)	0.84
R(observed vs predicted) square	0.84

Table B.9. Model estimates without the outlier for Widmanstatten ferrite (WF) formed in the WM of SA516 steel.

(a) Regression coefficients

Regression Coefficients	Estimated Regression Coefficients(ERC)	Asymptotic Standard Error (ASE)	ERC/ASE (t*)	Confidence Interval < 95%>	
				Lower	Upper
β_0	526.06	132.93	3.96	184.34	867.77
β_1	-1.43	0.34	-4.16	-2.23	-0.55
β_2	3.88	2.09	1.86	-1.48	9.24
β_3	0.00	0.00	4.42	0.00	0.00
β_4	-0.02	0.05	-0.51	-0.15	0.10
β_5	-0.01	0.00	-1.93	-0.01	0.00

(b) Analysis of variance

Source of variable	Sum of squares	Degree of freedom	Mean square	F statistic model	F statistic tabulated
Regression	2380.25	6	396.71	127.56	4.95
Error	15.55	5	3.11		
Total	2395.80	11			

(c) R-square

Raw R-square (1-Residual/Total)	0.99
Mean corrected R-square (1-Residual/Corrected)	0.91
R(observed vs predicted) square	0.91

APPENDIX C

C.1. Micrographs of Weld Zones for SA516 and A709 Steels

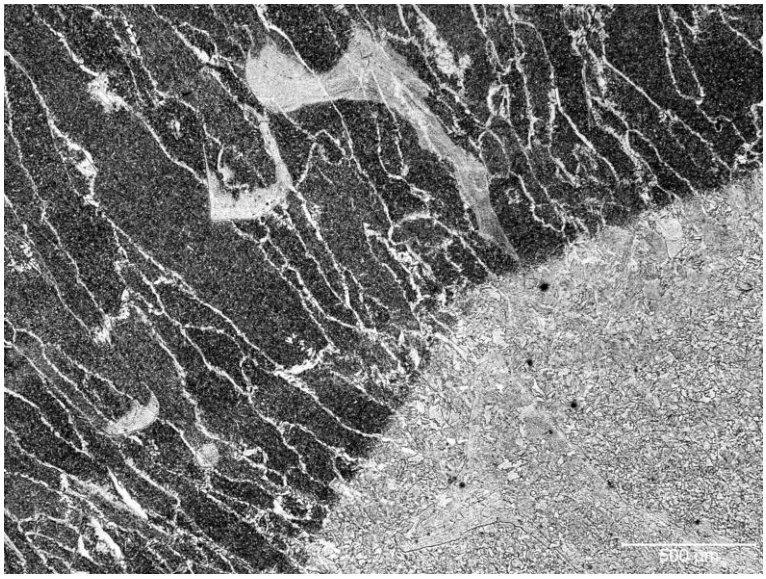

Figure C.1. Micrograph of weld metal and heat affected zone of A709 produced using 700 A and 9.3 mm/s.

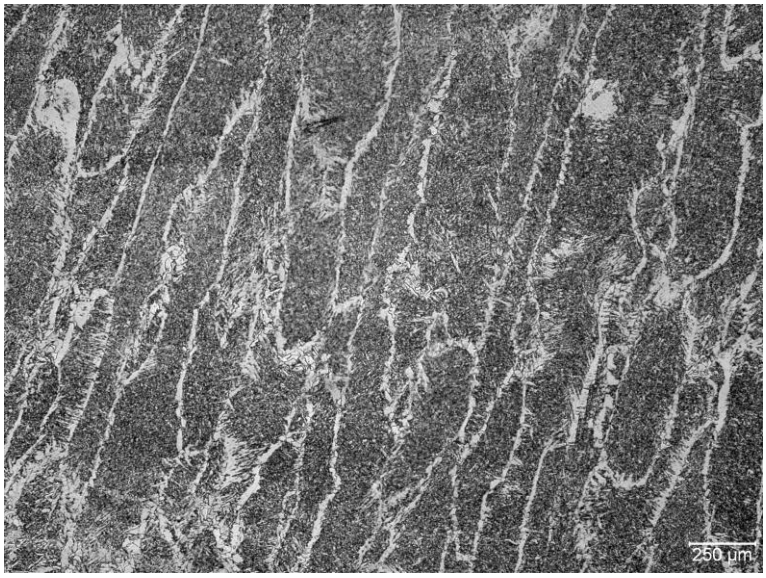

Figure C.2. Micrograph of the weld metal of A709 produced using 700 A and 9.3 mm/s.

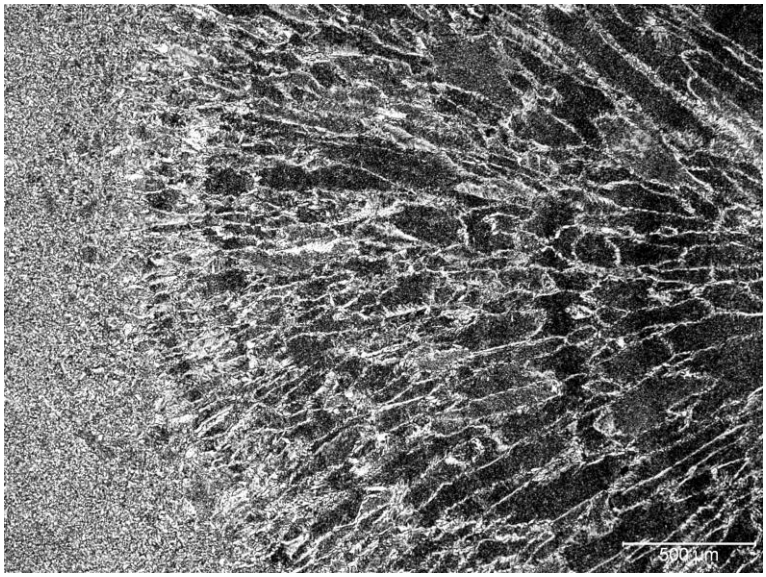

Figure C.3. Micrograph of weld metal and heat affected zone of A709 produced using 700 A and 12.3 mm/s.

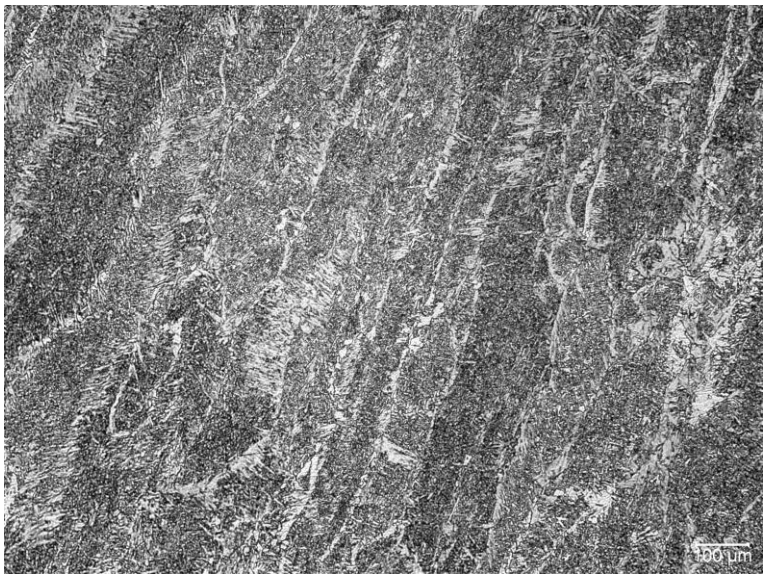

Figure C.4. Micrograph of the weld metal of A709 produced using 700 A and 12.3 mm/s.

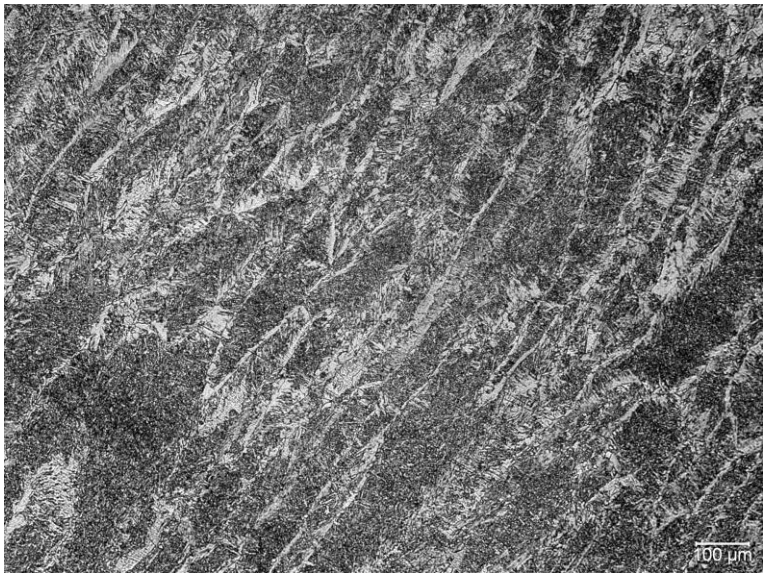

Figure C.5. Micrograph of the weld metal of A709 produced using 700 A and 15.3 mm/s.

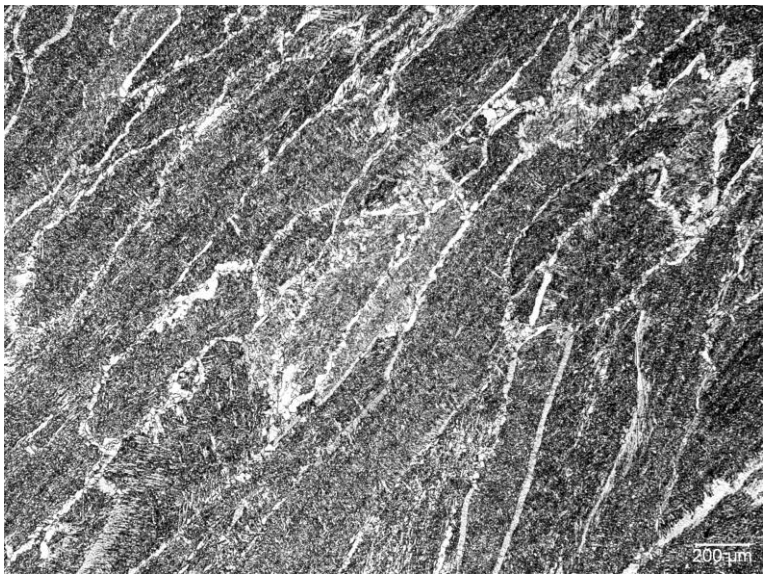

Figure C.6. Micrograph of the weld metal of A709 produced using 800 A and 5.3 mm/s.

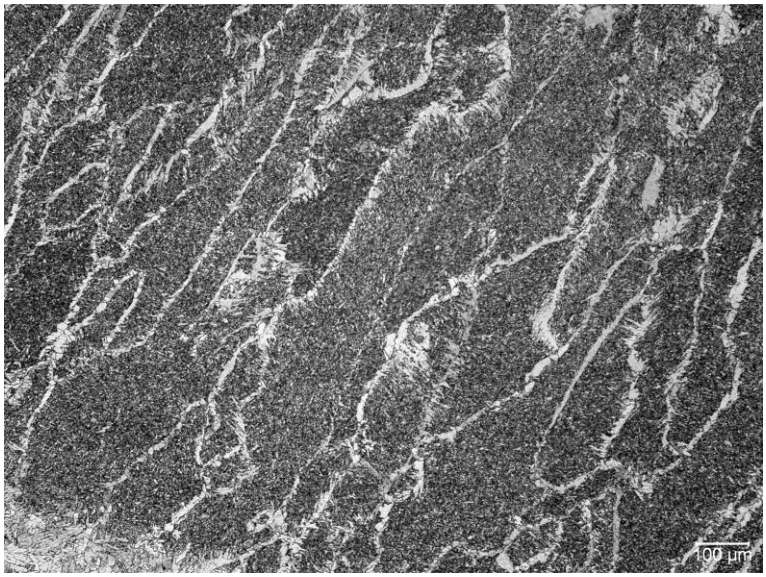

Figure C.7. Micrograph of the weld metal of A709 produced using 800 A and 9.3 mm/s.

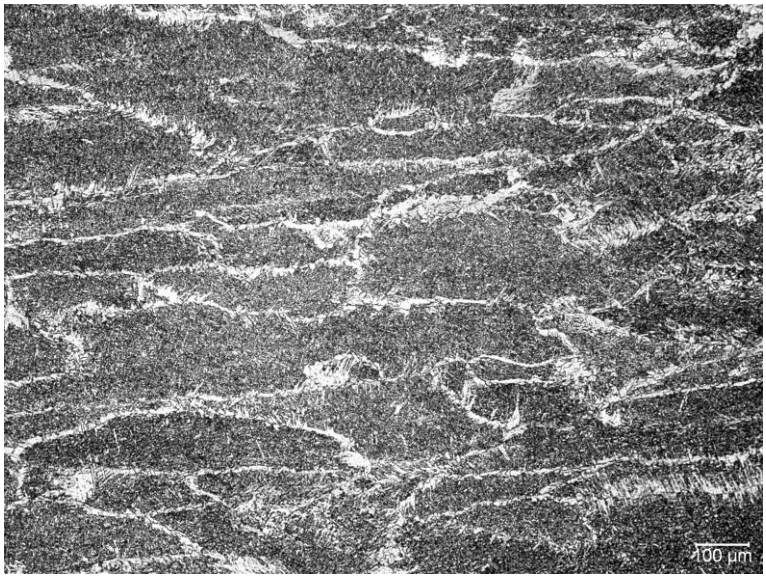

Figure C.8. Micrograph of the weld metal of A709 produced using 800 A and 12.3 mm/s.

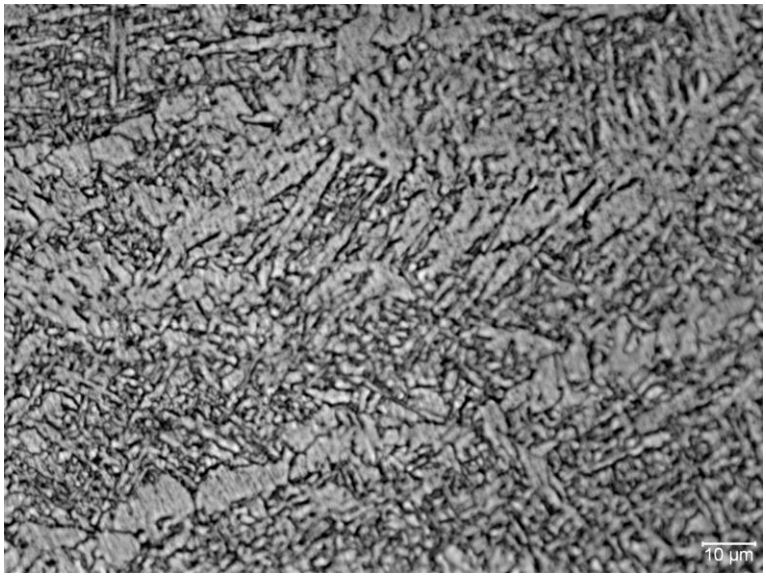

Figure C.9. Micrograph of the heat affected zone of A709 produced using 800 A and 15.3 mm/s.

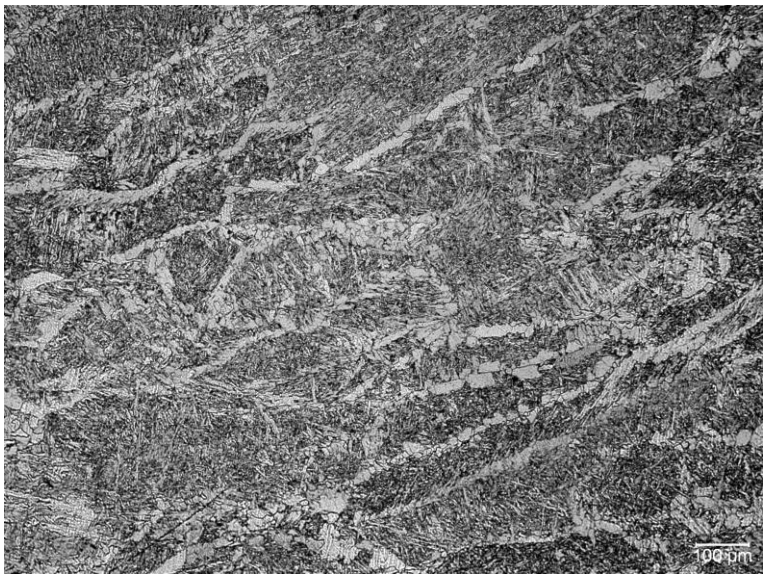

Figure C.10. Micrograph of the weld metal of A709 produced using 850 A and 5.3 mm/s.

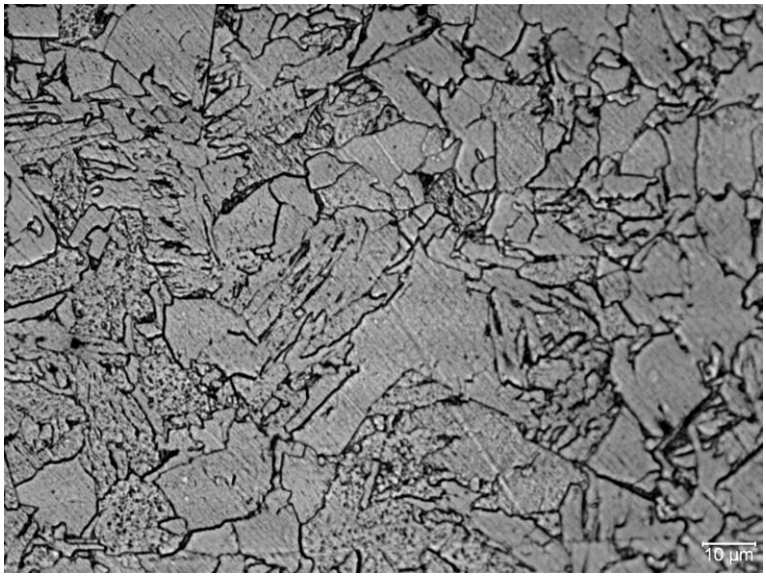

Figure C.11. Micrograph of the heat affected zone of A709 produced using 700 A and 9. 3 mm/s.

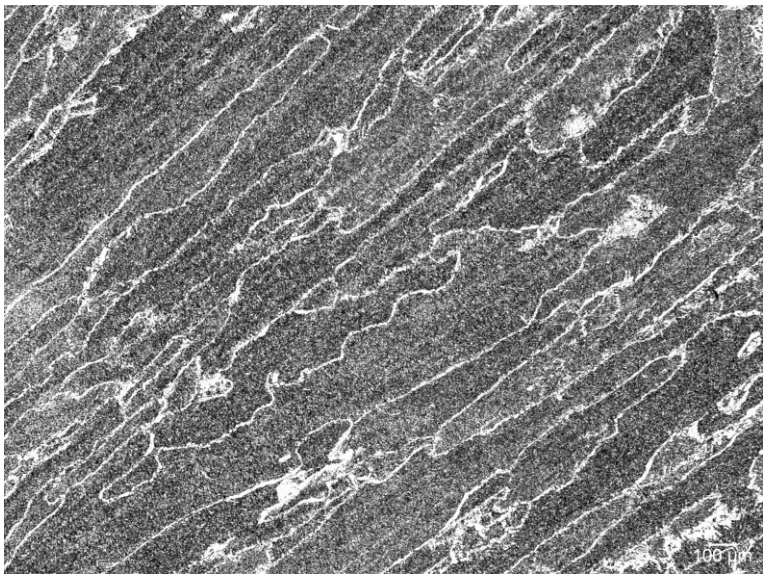

Figure C.12. Micrograph of the weld metal of A709 produced using 850 A and 9.3 mm/s.

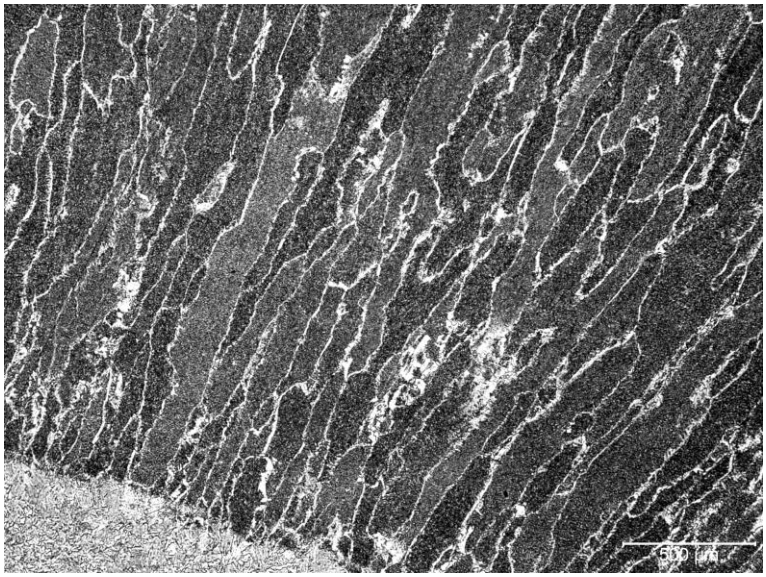

Figure C.13. Micrograph of weld metal and heat affected zone of A709 produced using 850 A and 12.3 mm/s.

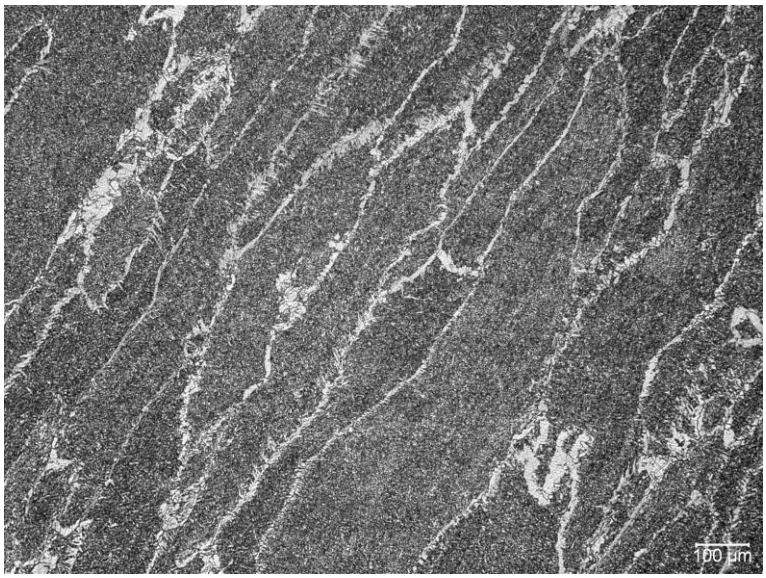

Figure C.14. Micrograph of the weld metal of A709 produced using 850 A and 15.3 mm/s.

Figure C.15. Micrograph of the heat affected zone of SA516 produced using 700 A and 5.3 mm/s.

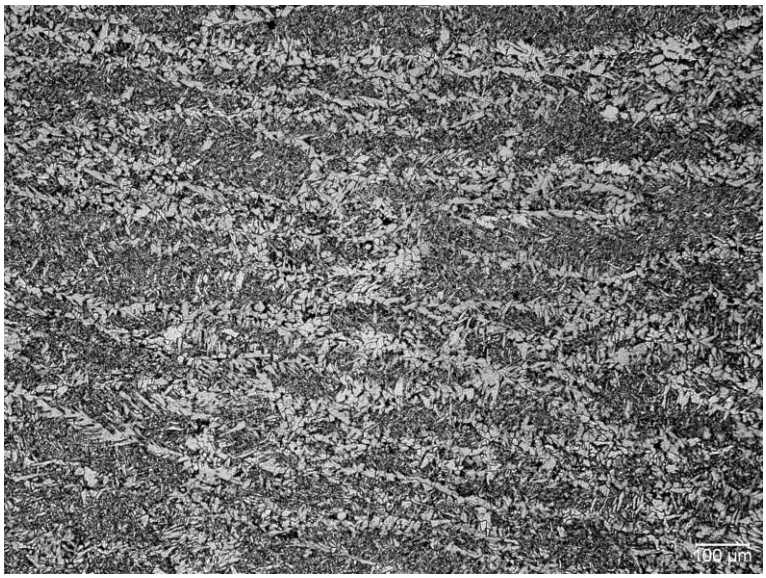

Figure C.16. Micrograph of the weld metal of SA516 produced using 800 A and 5.3 mm/s.

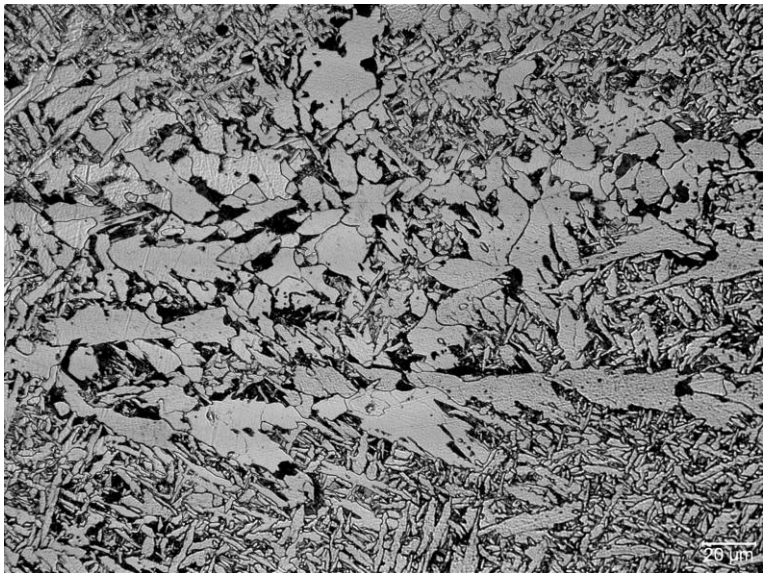

Figure C.17. Micrograph of the weld metal of SA516 produced using 850 A and 15.3 mm/s.

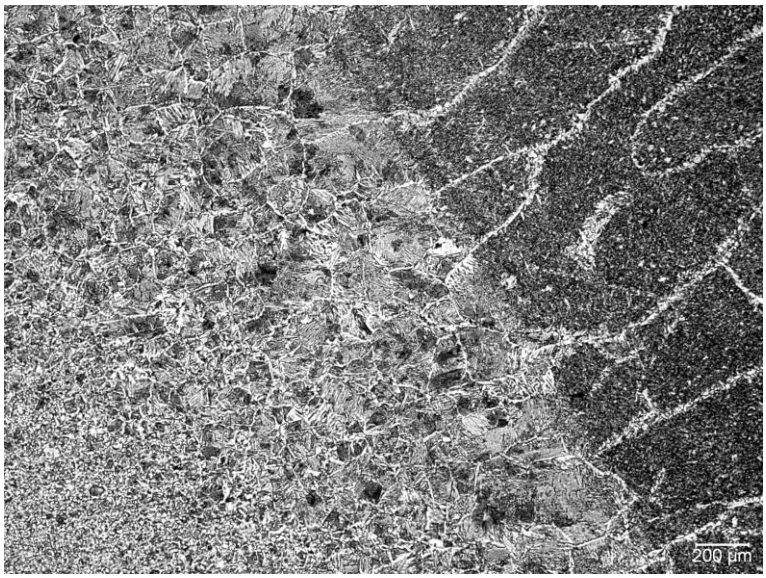

Figure C.18. Micrograph of weld metal and heat affected zone of SA516 produced using 800 A and 5.3 mm/s.

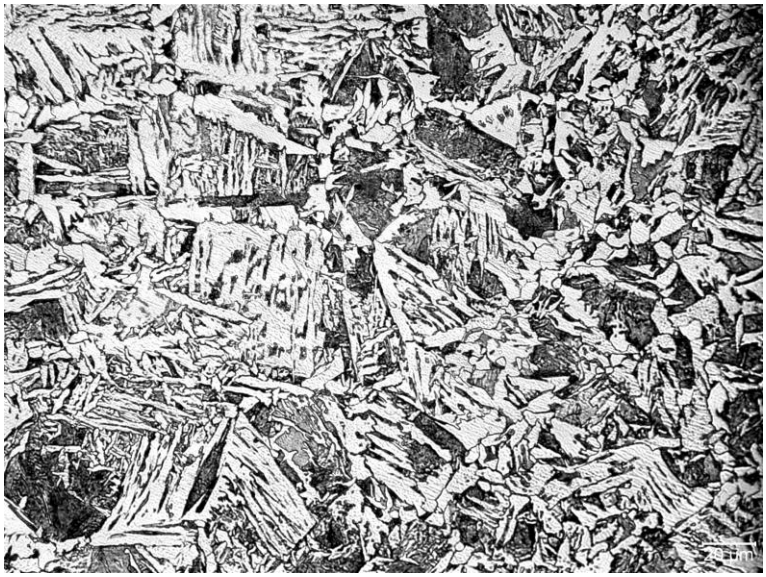

Figure C.19. Micrograph of the heat affected zone of SA516 produced using 800 A and 9.3 mm/s.

Figure C.20. Micrograph of weld metal of the SA516 produced using 800 A and 9.3 mm/s.

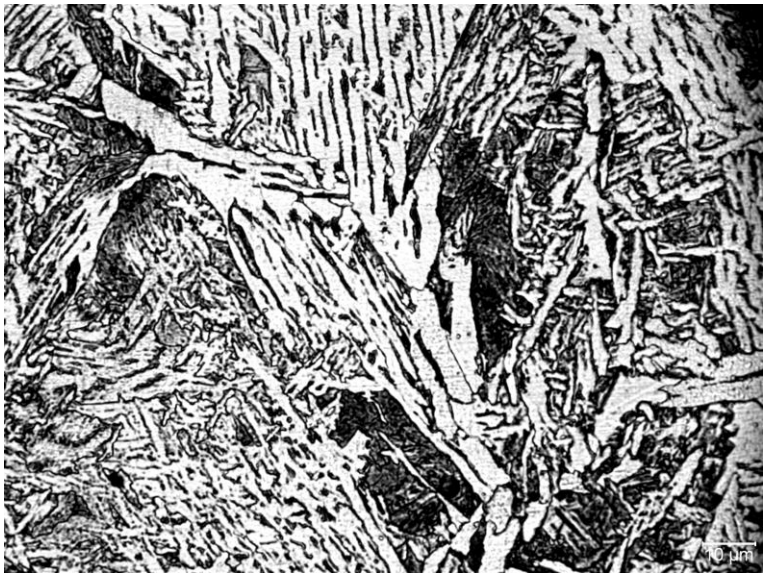

Figure C.21. Micrograph of the heat affected zone of SA516 produced using 800 A and 12.3 mm/s.

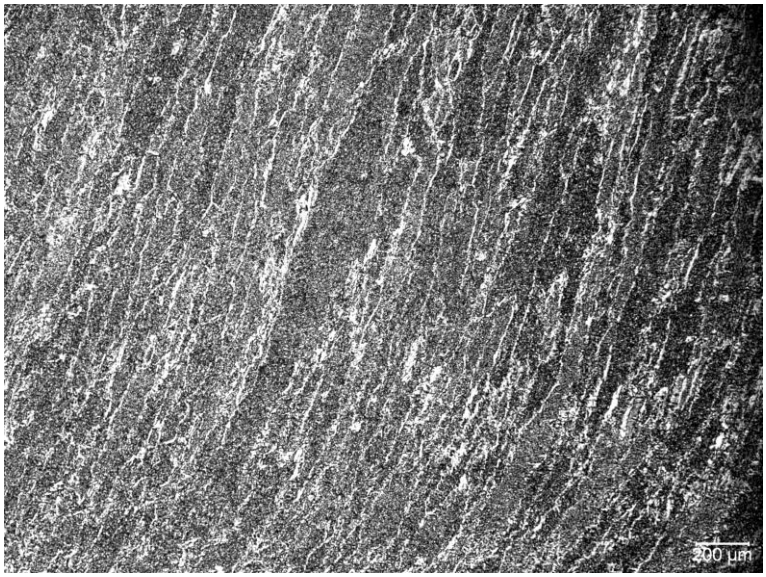

Figure C.22. Micrograph of the weld metal of SA516 produced using 800 A and 12.3 mm/s.

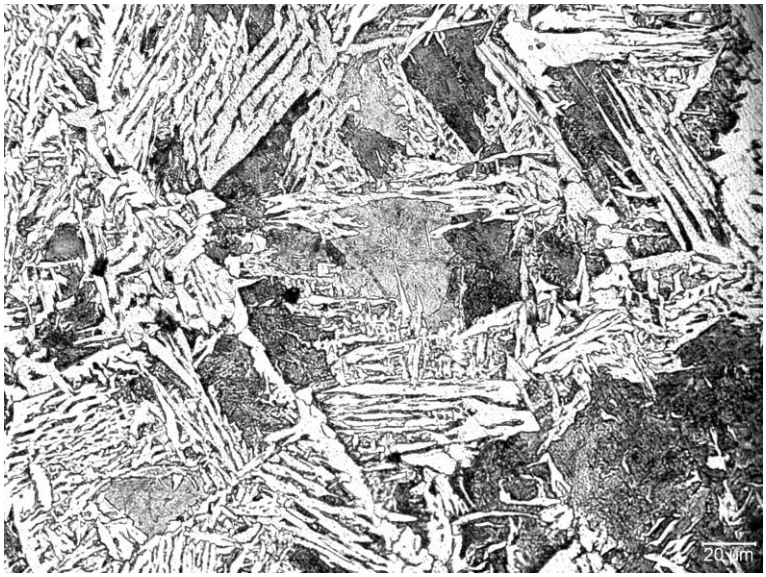

Figure C.23. Micrograph of the heat affected zone of SA516 produced using 850 A and 9.3 mm/s.

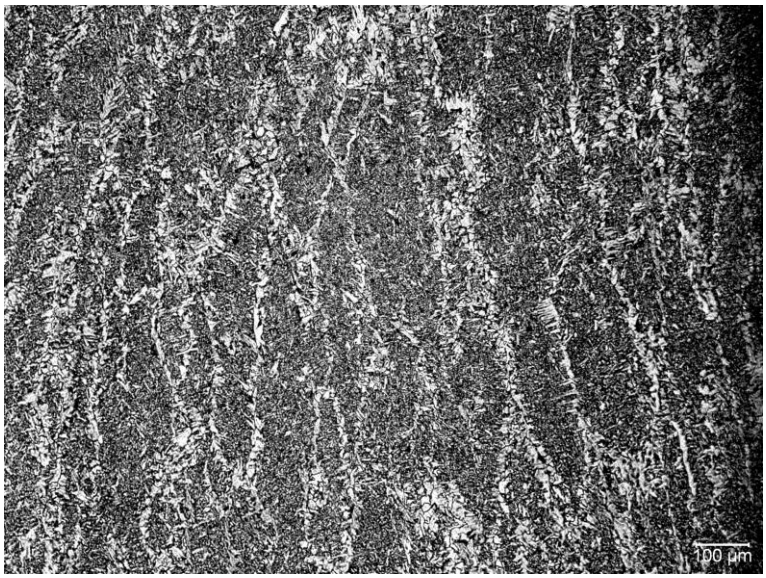

Figure C.24. Micrograph of the weld metal of SA516 produced using 850 A and 9.3 mm/s.

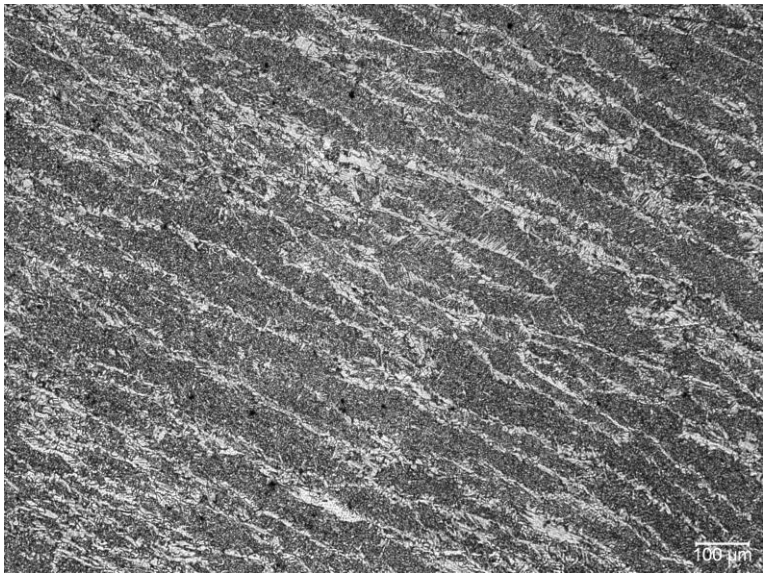

Figure C.25. Micrograph of the weld metal of SA516 produced using 850 A and 12.3 mm/s.

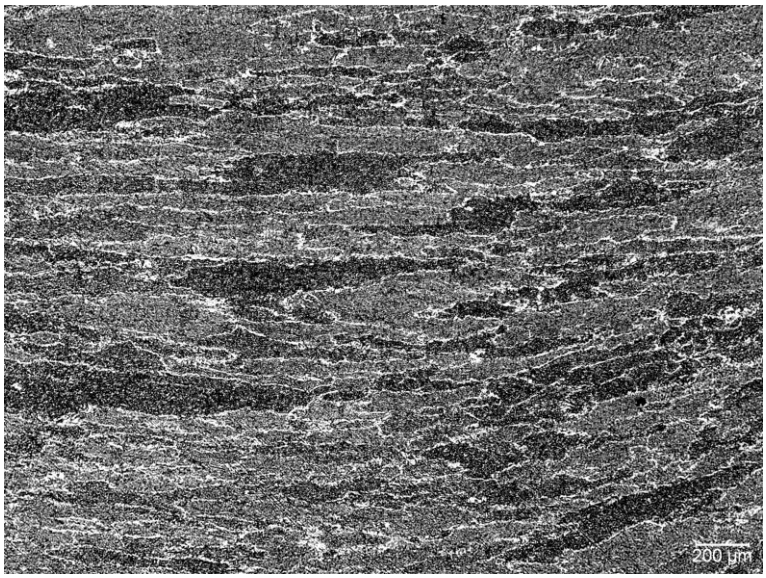

Figure C.26. Micrograph of the weld metal of SA516 produced using 850 A and 15.3 mm/s.

APPENDIX D

D.1 Inverse Lever Rule Calculations

The inverse lever rule is for determining the amount of each phase in a two-phase system. In the present work, it was used to calculate the relative amounts of primary ferrite and pearlite in the base metals of SA516 and A709 steels. For an alloy of composition of Co in Figure D.1, the fractions of primary ferrite (α) and pearlite (P) are determined using equations D1 and D2, respectively.

$$\alpha = \frac{U}{T+U} \tag{D.1}$$

$$P = \frac{T}{T+U} \tag{D.2}$$

Using equations D.1 and D.2, the relative amounts of the base metals primary ferrite and pearlite in SA516 and A709 steels were calculated.

For SA516 steel with carbon content of 0.223 wt.% (Co = 0.223):

$$\text{Primary } \alpha = \frac{0.77-0.22}{0.77-0.022} x100 = 73.5\%;\ P = \frac{0.22-0.022}{0.77-0.022} x100 = 26.5\%$$

The amounts of ferrite and pearlite determined for SA516 steel base metal using Pax-it image analysis were 70% and 30%, respectively.

For A709 steel with carbon concentration of 0.04 wt.% (Co = 0.04):

$$\text{Primary } \alpha = \frac{0.77 - 0.04}{0.77 - 0.022} x100 = 97.59\% \; ; \; P = \frac{0.04 - 0.022}{0.77 - 0.022} x100 = 2.41\%$$

The amounts of ferrite and pearlite determined for A709 steel base metal using Pax-it image analysis were 94% and 6%, respectively.

D.2. ASTM Grain Size Number

The average grain size estimation was done using Pax-it image analysis software using micrographs at 100X magnification. Pax-it output gave average grain diameter (μm). The ASTM grain size number was determined using the value of the average grain diameter in Table II in [15]. For SA516 with the average grain diameter of 27 μm, the ASTM micro-grain size number N = 7.5. From the same table, for A709 steel, with an average grain diameter of 32 μm, the ASTM micrograin size number N = 7.0. Table D.1 shows part of Table II in [15] micro-grain size relationships that was used in ASTM grain number determination.

Table D.1. Micro-grain size relationships from Table II

ASTM micro-grain size number (N)	Average intercept diameter (mm)
6.5	0.038
	0.035
7.0	0.032
	0.030
7.5	0.027
	0.025

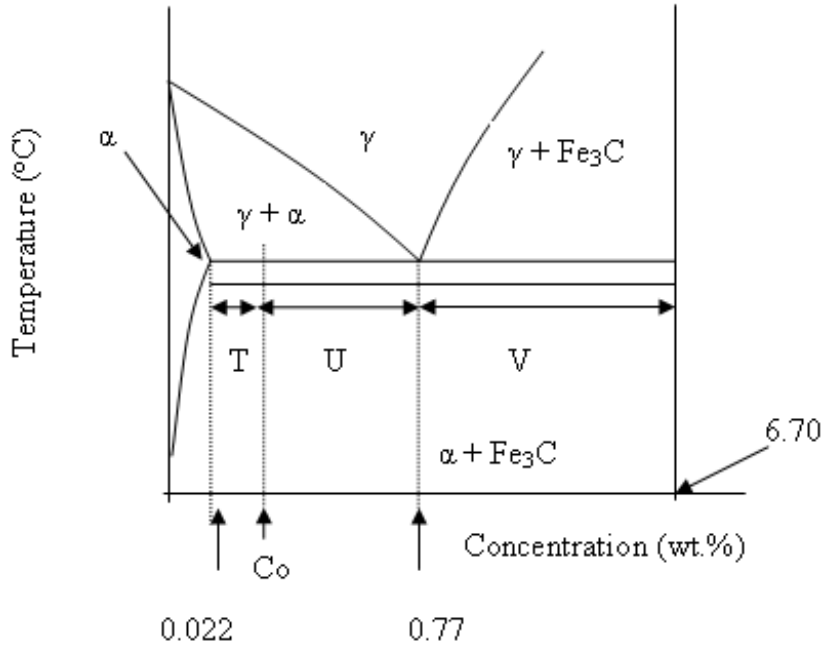

Figure D.1. A portion of Fe-Fe3C phase diagram used to calculate the relative amounts of primary ferrite and pearlite microconstituents.

APPENDIX E

E 1 Copyright Permission

RE: permission to use your diagram [Reference: 110115-001989]
Tuesday, January 18, 2011 4:07 AM
From:
"Parker, Kerry (ELS-OXF)" <Kerry.Parker@elsevier.com>
Add sender to Contacts
To:
jamesadi1@yahoo.com
Dear James

We hereby grant you permission to reproduce the material detailed below in print and electronic format at no charge subject to the following conditions:

1. If any part of the material to be used (for example, figures) has appeared in our publication with credit or acknowledgement to another source, permission must also be sought from that source. If such permission is not obtained then that material may not be included in your publication/copies.

2. Suitable acknowledgement to the source must be made, either as a footnote or in a reference list at the end of your publication, as follows:

"This article was published in Publication title, Vol number, Author(s), Title of article, Page Nos, Copyright Elsevier (or appropriate Society name) (Year)."

3. This permission is granted for non-exclusive world rights in all languages.

4. Reproduction of this material is granted for the purpose for which permission is hereby given, and includes use in any future editions.

Kind regards
Kerry

Kerry Parker :: :: Rights Associate
Global Rights Dpt :: :: Elsevier Ltd

Tel: +44 1865 843280
Fax: +44 1865 853333
Email: kerry.parker@elsevier.com

-----Original Message-----
From: I.Internet [mailto:i.internet@elsevier.com]
Sent: 17 January 2011 15:46
To: jamesadi1@yahoo.com
Cc: Rights and Permissions (ELS)
Subject: permission to use your diagram [Reference: 110115-001989]

Subject

permission to use your diagram

Discussion

Response (Khader Basha Ahmed) - 17/01/2011 03.46 PM

Dear James Amanie,

Thank you for your inquiry.

I have forwarded your email to Elsevier's Global Rights Department at permissions@elsevier.com for their assistance. They respond to routine requests within 15 working days unless you have specified a more immediate deadline. Regular permission letters and correspondence are usually sent via email. You may also phone (215)239-3804 (US) or +44(0)1865 843830 (UK).

If you have any questions please let me know.

Regards,

Kuldeep Singh
Elsevier Customer Service

Customer By Email (james amanie) - 15/01/2011 11.58 PM

Dear Sir/Madam,

I am a graduate student at the University of Saskatchewan, Saskatoon, Canada. In the literature review of my thesis, I discuss the weld metal and the heat affected zone. I would like to use your diagram in “Introduction to the Physical Metallurgy of Welding” by Kenneth Eastering, 1983, Figure 3.1, page 104 to explain the effect of welding process and request you to grant me permission to use the diagram.

I hope my request will be granted and thank you in advance.

Thank you.

James Amanie.

Elsevier Limited. Registered Office: The Boulevard, Langford Lane, Kidlington, Oxford, OX5 1GB, United Kingdom, Registration No. 1982084 (England and Wales).
[---001:002331:13766---]

Elsevier Limited. Registered Office: The Boulevard, Langford Lane, Kidlington, Oxford, OX5 1GB, United Kingdom, Registration No. 1982084 (England and Wales).